STABILITY ANALYSIS OF THE NAMIBIAN POWER GRID WITH INTEGRATION OF LARGE OFFSHORE WIND FARMS USING A VSC-HVDC SCHEME

BY

NICKY K. MBAIMBAI

STUDENT NO: 22064698

IN FULFILMENT OF MASTER OF ENGINEERING IN ELECTRICAL POWER

DEPARTMENT OF ELECTRICAL POWER ENGINEERING

FACULTY OF ENGINEERING AND THE BUILT ENVIRONMENT

DURBAN UNIVERSITY OF TECHNOLOGY

NOVEMBER 2021

Supervisor: Prof. I. E. Davidson

DECLARATION 1 – PLAGIARISM

I, Nicky K. Mbaimbai, declare that:

1. The research reported in this dissertation, except where otherwise indicated, is my original research.
2. This dissertation has not been submitted for any degree or examination at any other university.
3. This dissertation does not contain other persons' data, pictures, graphs or other information, unless specifically acknowledged as being sourced from other persons.
4. This dissertation does not contain other person's writing, unless specifically acknowledged as being sourced from other researchers. Where other written sources have been quoted, then:
    a. Their words have been re-written but the general information attributed to them has been referenced.
    b. Where their exact words have been used, then their writing has been placed in italics and inside quotation marks, and referenced.
5. This dissertation does not contain text, graphics or tables copied and pasted from the internet, unless specifically acknowledged, and the source being detailed in the dissertation and in the References sections.

Signed:

Mr. Nicky K. Mbaimbai

Date: 19-11-2021

As the candidate's Supervisor, I agree/do not agree to the submission of this dissertation.

Signed:

Prof. I.E., Davidson

Date: 22-11-2021.

DEDICATION

This research is dedicated to my wife Kate and my sons Nasir and Nuri. You have all inspired me once again to pursue all my hopes and dreams with renewed vigour.

ACKNOWLEDGMENTS

First and most importantly, I would like to thank and give praise to God Almighty for granting me the gift of life, strength, knowledge, patience and will to carry out this research project.

Secondly, I would like to express my profound gratitude to Professor Innocent Davidson for his supervision, mentoring and visionary direction. I will forever embody all the lessons he taught me throughout my studies. One of those lessons being the continued pursuit of excellence.

I would also like to thank Mr. Severus Sheetekela for investing his time and knowledge in assisting me and for being an industrial mentor. I will forever be grateful for the kindness and encouragement that he has shown me.

I would like to thank all the Electrical Power Engineering Department staff members at the Durban University of Technology, including all my fellow researchers, for their input and continuous encouragement. Being part of the Smart Grids Research Group has truly been a life and career elevating experience.

Finally, I would like to thank my family and friends for their patience, understanding, and encouragement throughout the duration of my studies.

Nicky K. Mbaimbai

November 2021

ABSTRACT

The use of the wind for electrical power production has seen a meteoric increase due to the wind being a free and abundantly available resource, especially when the site is offshore. The wind resource along the Namibian coastline could therefore be implemented to develop offshore wind farms that would enable Namibia to meet its steadily increasing power demand. The efficient transmission of bulk power from offshore sites to the onshore AC grid is widely achieved through voltage source converter-based high voltage direct current (VSC-HVDC) schemes.

This study aims to investigate the power system stability response of the Namibian network, particularly in terms of rotor angle stability, to the integration of large offshore wind farms. A single machine infinite bus (SMIB) model developed in DIgSILENT PowerFactory was used as a test bed for the study. Transient and small-signal stability analysis in relation to different fault scenarios on the main transmission lines were then carried out after doubly-fed induction generators (DFIGs) representing offshore wind farms were integrated into the SMIB model. The same methodology was applied on a reduced model of the NamPower network. DigSILENT PowerFactory's VSC-HVDC offshore wind farm template model was integrated to a reduced model of the NamPower network. The entire network was then subjected to different fault scenarios along backbone transmission lines, major busbars and the HVDC link at different penetration levels of offshore wind power.

The study established that the integration of large offshore wind farms using a VSC-HVDC scheme to the reduced NamPower network negatively affected the network's transient and small-signal stability. However, there was a positive impact on the voltage levels of the network due to the reactive power compensation supplied by the VSC-HVDC link. The VSC-HVDC link also maintained low-voltage ride-through of the offshore wind farms during faults that comply with the Namibian transmission grid code.

DECLARATION 2 – PUBLICATIONS

The following publication emanated from this research:

[1] Nicky Mbaimbai and Innocent Davidson, "Feasibility of Offshore Wind Power for Namibia," in 2021 IEEE PES/IAS Power Africa Virtual Conference,23-27 August 2021.

[2] Nicky Mbaimbai and Innocent Davidson, " Small Signal Stability Analysis of a Power Network with Increasing Offshore RE Penetration Using a VSC-HVDC Scheme," Paper submitted to the 2022 SAUPEC 2022 Conference, 25-27 January 2022. [Under review]

TABLE OF CONTENTS

LIST OF FIGURES

LIST OF TABLES

LIST OF ABBREVIATIONS

AC	Alternating Current
BB	Busbar
CCT	Critical Clearing Time
CFSS	Critical Fault Screening Script
CLI	Caprivi Link Interconnector
DC	Direct Current
DFIG	Doubly Fed Induction Generator
DTU	Denmark Technical University
EMT	Electromagnetic Transient
FACTS	Flexible Alternating Current Transmission Systems
GWA	Global Wind Atlas
HVAC	High Voltage Alternating Current
HVDC	High Voltage Direct Current
IGBT	Insulated Gate Bipolar Transistor
IPP	Independent Power Producer
LCC	Line Commutated Converter
PSS	Power System Stabilizer
PWM	Pulse Width Modulation
RMS	Root Mean Square
SAPP	South African Power Pool
SCIG	Squirrel Cage Induction Generator
SCR	Short Circuit Ratio
SMIB	Single Machine Infinite Bus
TSR	Tip-Speed Ratio
VSC	Voltage Source Converter

CHAPTER 1: INTRODUCTION

1.1 Background

The global requirement for a stable, reliable, and affordable electrical power system has grown significantly in recent times. Like the rest of the world, Namibia has also recorded an increase in the annual power demand due to urbanisation and a steadily growing industrial sector [1]. NamPower, the national power utility, is the only bulk producer of power with a generation capacity of 459.5MW against a demand of approximately 700MW. The surplus power demand is addressed through imports from South Africa's Eskom and Zambia's ZESCO [2]. NamPower has embarked on developing renewable energy power plants such as wind farms and solar PV plants to address the energy shortage and reduce dependency on imported power [3].

NamPower and a number of independent power producers (IPPs) have developed several solar PV plants in recent years, with the largest being the 37 MW Hardap Solar PV plant [4]. In comparison, the development of wind farms has been significantly slower in terms of implementation. The largest wind farm to date, Ombepo, is an onshore installation in the town of Lüderitz with a rating of 5MW [4].Preliminary site condition assessments have concluded that the Namibian coastline has a large potential for the development of large offshore wind farms. Large offshore wind farms would enable Namibia to alleviate its power shortage and possibly become a net exporter of power to the rest of the South African Power Pool (SAPP) [5].

The interconnection of offshore wind farms, just like any other power plant, might affect the performance of the electrical grid in terms of power system stability. Literature has also shown that offshore wind farms might greatly affect the rotor angle stability of a weak or small network such as the Namibian power system which has long radial lines. Voltage Source Converter High Voltage Direct Current (VSC-HVDC) links may be implemented to efficiently deliver power from the remote offshore wind farm to the onshore grid. Moreover, it is also documented that VSC-HVDC links may also improve the stability of a weak or small network [6]. Therefore, it is imperative to assess the rotor angle and voltage stability of the grid with the integration of additional power plants to ensure compliance with the national grid code.

1.2 Research Questions

The investigation aims to answer the following research questions:

- How does the integration of offshore wind farms via a VSC-HVDC link affect the rotor angle stability of Namibia's national grid?
- Do the integrated offshore wind farms comply to the Namibian transmission grid code in terms of low voltage ride-through capability?

1.3 Research Objectives

The main objectives of this study are to:

1. To investigate how the integration of offshore wind farms via VSC-HVDC to Namibia's national grid will affect the grid's performance.

   This objective will be achieved by carrying out the following tasks:

   - Analyzing the impact of integrating large offshore wind farms via VSC-HVDC to the national grid with regard to transient stability.
   - Analyzing the impact of integrating large offshore wind farms via VSC-HVDC to the national grid with regard to small-signal stability.

2. To analyze the compliance of the integrated offshore wind farms to the Namibian transmission grid code with regards to the low-voltage ride-through capability.

1.4 Significance of the Study

The study of the impact of integrating offshore wind farms on the national grid stability is quite significant because, as far as this researcher is aware, there is no documentation indicating that research of a similar kind has been conducted on the Namibian National Grid, thus far. Therefore, the research findings would serve as a guideline for Namibia's power utility company (NamPower) to integrate large offshore wind farms into the grid without significantly affecting the grid's performance. The installation of new power system components, particularly wind farms and HVDC transmission schemes, is technically challenging and requires a thorough understanding of the technical operation of the components before they can be implemented. Therefore, the results of this study will assist network planners in the decision-making process by assessing the technical performance of the grid.

1.5 Project Scope, Limitations, and Delimitations

The analysis of the rotor angle stability is carried out on a reduced DIgSILENT PowerFactory model of NamPower's network and not on the full NamPower network model as NamPower is not able to share the DIgSILENT PowerFactory model of its full network with non-employees. Moreover, the accuracy of all power system component models that will be used for this study is limited to the modelling capabilities of the DIgSILENT PowerFactory software. The power generation capacity of the wind farms is limited to the available wind data as provided by Global Wind Atlas.

1.6 Dissertation Layout

Chapter 1: This chapter introduces the main topics that will be considered for the power system stability analysis. Moreover, the research objectives and the significance of the studied are also highlighted in this chapter. The chapter concludes by defining the parameters of the analysis in terms of the scope, limitations, and delimitations.

Chapter 2: This chapter explores the main concepts to be considered in wind farm development, such as wind energy conversion systems and wind turbine classification. Different wind turbine generators are also explored, with the focus being on DFIGs. The chapter then highlights the topology of a power system before discussing power system stability, emphasizing rotor angle stability. The configuration and different control strategies of HVDC schemes are the closing discourse of the chapter.

Chapter 3: This chapter details the rationale behind the sizing of the offshore wind farms and the modelling of the base model VSC-HVDC scheme that is adopted for the research study. The reduced NamPower network model that was adopted as a study case is also introduced.

Chapter 4: This chapter presents the SMIB model used as a test bed for the study and the methodology for the study. The analysed results for both the SMIB model and the reduced NamPower network model with the integration of offshore wind farms through a VSC-HVDC scheme are discussed in depth in this chapter.

Chapter 5: This chapter gives the conclusions that were drawn from the analysis of results. It further provides recommendations on research areas that could expand the research work around this topic in the future.

CHAPTER 2: LITERATURE REVIEW

2.1 Wind Energy Conversion Systems

The use of the wind as a source of power generation has grown significantly in recent times. This is because the wind is a free, abundantly available, and clean source of energy. The current global installed wind generation capacity is approximately 621 GW as shown in Figure 2-1 below. The portion of offshore wind energy generation is only about 28GW or 4.51% of this installed capacity [7, 8]. Parameters such as wind power and wind speed have to be considered to optimize the conversion of wind energy into electrical power at any potential site, more so when the site is offshore where wind speeds are higher [9].

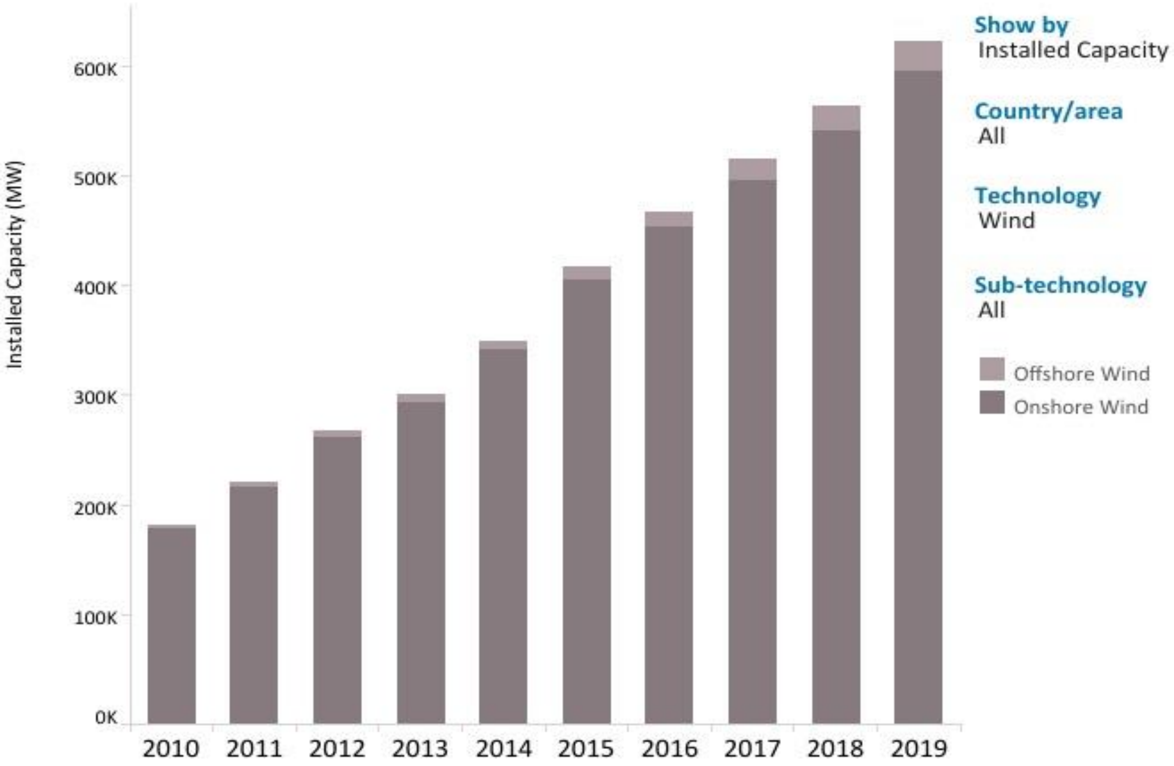

Figure 2-1: Global wind energy installed capacity *[8]*

2.2 Wind Power

The energy that can be captured from the wind and converted into electrical power by a turbine is given by [10, 11]:

$$P_w = \frac{1}{2}\,\rho\, A\, V^3 \tag{2-1}$$

Where ρ is the air density in kg/m^3. This equates to an air density value of 1.23 kg/m^3 for offshore sites as they are at sea level;

A is the area that is swept by the rotor blades in m^2 ;

V is the wind speed in m/s.

The efficiency with which a turbine can convert energy from the wind into power is referred to as the power coefficient (C_p). The maximum theoretical power coefficient at which a turbine can operate is 59.26% as per Figure 2-2 below. This value is known as the Betz Limit [12, 13].

Taking the Betz Limit into account, the power that can be generated by a turbine (P_m) is therefore given by [13]:

$$P_m = P_w\, X\, C_p \tag{2-2}$$

Where P_w is the power available in the wind and C_p is the power coefficient. The power coefficient C_p also depends on the ratio of the speed of the rotor to the wind speed; this ratio is known as the tip-speed-ratio (TSR) and is given by Equation (2-3) [12] [14] [15].

$$\lambda = \frac{R\,\omega_r}{v} \tag{2-3}$$

Where ω_r is the rotor speed in radians/s and $\omega_r = 2\pi f$, with f being the rotational frequency [12].

R is rotor radius in meters, and v is the wind speed in m/s.

In order for a turbine to achieve a high energy conversion ratio, the rotor should operate within an optimum range as determined by the tip-speed-ratio calculations [12].

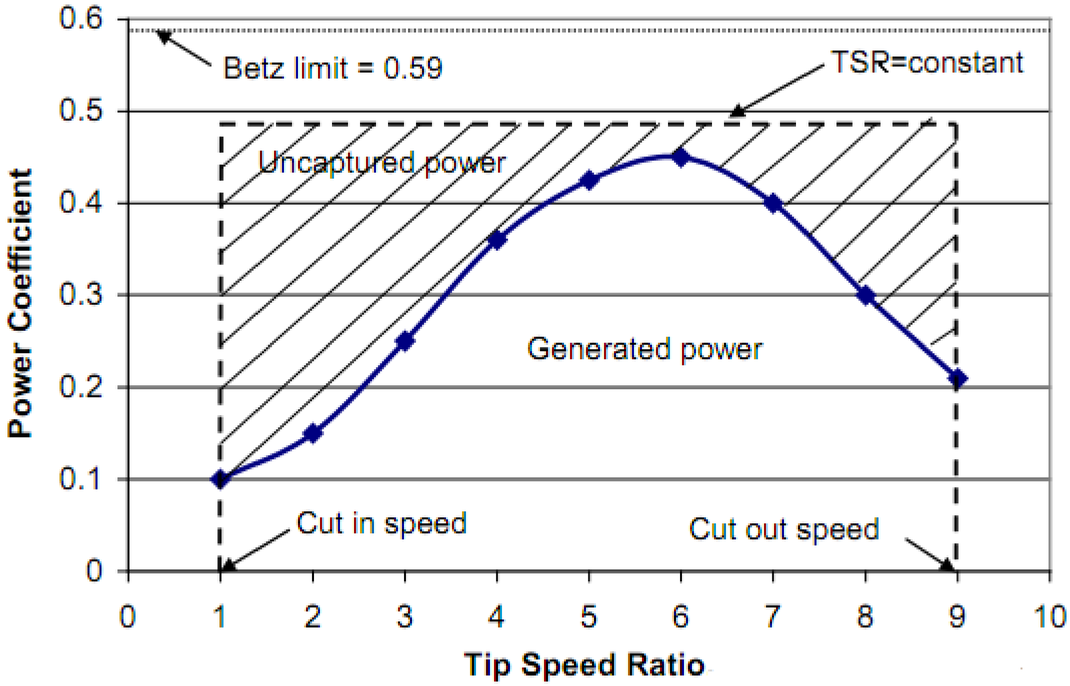

Figure 2-2: Power coefficient as a function of tip-speed ratio *[12]*

2.2.1 Wind Power Density

The wind power density is an important factor in selecting a site for establishing a wind power plant as it indicates the amount of wind energy that can be captured by a turbine and converted into electrical power. Sites with Class 4-6 wind power densities are more suitable for large-scale wind farms as given in Table 2-1 below [11] [16]. The wind power density (P_D) in W/m^2 when calculated using the two-parameter Weibull distribution method is given by [16, 17]:

$$P_D = \frac{1}{2}\,\rho\, c^3 \,\left(1 + \frac{3}{k}\right) \qquad (2\text{-}4)$$

Where ρ is the air density in kg/m^3, c is the scale parameter in m/s and k is the shape parameter.

Table 2-1: Wind power density classification *[11]*

	10-meter height		**50-meter height**	
Wind power class	**Wind power density (W/m^2)**	**Mean wind speed (m/s)**	**Wind power density (W/m^2)**	**Mean wind speed (m/s)**
1	<100	<4.4	<200	<5.6
2	100-150	4.4-5.1	200-300	5.6-6.4
3	150-200	5.1-5.6	300-400	6.4-7.0
4	200-250	5.6-6.0	400-500	7.0-7.5
5	250-300	6.0-6.4	500-600	7.5-8.0
6	300-350	6.4-7.0	600-800	8.0-8.8
7	>400	>7.0	>800	>8.8

2.3 Wind Turbine Classification

Wind energy is considered to be a viable renewable energy source due to its abundance and cleanliness. This abundant wind energy is converted into electricity using wind turbines. Wind turbines are generally classified into two groups; horizontal axis wind turbines (HAWT) and vertical axis wind turbines (VAWT) [18].

Vertical Axis Wind Turbines (VAWT) have blades that rotate on an axis that is vertical to the surface on which they are erected. VAWTs do not require the implementation of any yaw control as they produce power through multidirectional rotation. VAWTs are also relatively cheaper than HAWTs because major components such as the gear box and generator are installed at the base of the turbine on the ground. This configuration further results in VAWTs being shorter in height, and this drives down their cost of installation even more. Despite their cost of installation being relatively cheaper, VAWTs are not as widely installed as HAWTs due to their low conversion efficiency [11] [19, 20].

Horizontal Axis Wind Turbines (HAWTs) have blades that rotate on an axis that is parallel to the ground. HAWTs are the most commonly used turbine nowadays due to their high efficiency and power density conversion factor [11]. Major components such as the gearbox and generator are installed at the top of a structurally sound tower and thus drastically increasing the cost of construction for HAWTs [19] [11]. HWATs are further classified into two installations; upwind HAWTs and downwind HAWTs. Upwind HAWTs are installed so that the rotor blades capture the oncoming wind whereas downwind HAWTs are installed in a manner that allows the rotor blades to capture the outgoing wind stream [11] [19] [21].

2.3.1 Configuration of a Wind Turbine

Modern wind turbines are made up of three main components; the nacelle, the rotor and the tower. The tower is used as the foundation to hold up all the other components and is mostly made from steel or concrete, and is between 80-100 meters in height. The elongated height enables the capture of maximum wind speeds [18] [22] [23].

The nacelle sits above the tower and contains the following components as seen in Figure 2-3 below [23, 24, 25]:

- **Anemometer**: Measures the wind speed and inputs these readings to the controller.
- **Brake**: Halts the movement of the rotor in case of emergency or routine maintenance.
- **Gearbox**: Increase the speed of rotation from approximately 60 revolutions per minute (rpm) in the low-speed shaft to between 1200-1800 in the high-speed shaft for the production of electricity.
- **Generator**: Produces electricity as a result of the rotation of the high-speed shaft.
- **High speed shaft**: Enables the high-speed rotation of the generator.
- **Low speed shaft**: Connects the drive train to the rotor.
- **Pitch**: Governs the operation of the rotor when the wind speed is significantly low or too high for the efficient production of electricity.
- **Yaw drive**: Positions upwind turbines towards the oncoming wind. The yaw drive is not required in downwind turbines.
- **Yaw motor**: Enables the operation of the yaw drive.

The rotor consists of a hub and blades that capture the wind, consequently resulting in rotation of the rotor blades.

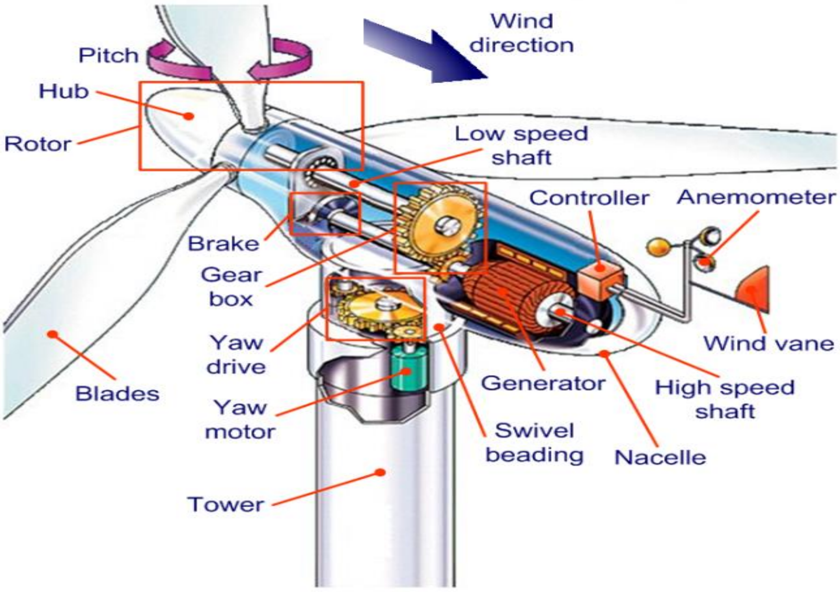

Figure 2-3: main components of a wind turbine *[26]*

2.3.2 Operating Characteristics of a Wind Turbine

The wind speed at a given location greatly affects the electrical power produced by a wind turbine. The wind turbine power curve as seen in Figure 2-4 depicts the relationship between the two parameters as being divided in three regions; the cut-in wind speed, rated output wind speed and cut-out wind speed [11] [27] [25].

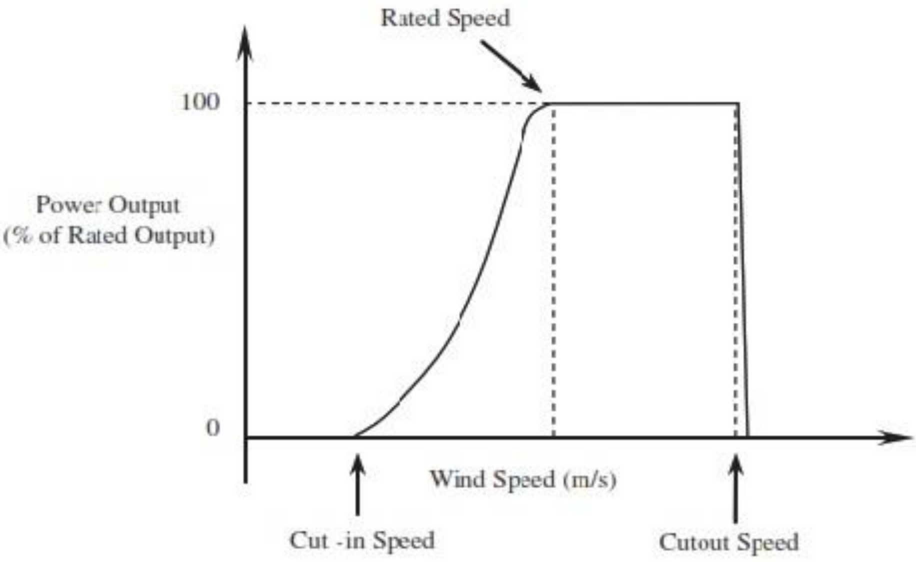

Figure 2-4: Wind turbine power curve *[11]*

2.3.2.1 *Cut-in wind speed*

This is the speed at which the wind turbines start power production. Most turbines have a cut-in speed of 3-4m/s. No energy production takes place below the cut-in speed as the rotor does not have any motion [11, 25].

2.3.2.2 *Rated output wind speed*

This is the region in which the wind turbines produce their maximum rated output power. The output power will not surpass the rated power at speeds in the range of 12-17m/s due to the operation of the power control mechanism of the turbine [11, 25].

2.3.2.3 *Cut-out wind speed*

The cut-out wind speed is the speed at which the turbine automatically shuts off in order to avoid any damage as it cannot safely produce power beyond this wind speed. Most turbines have their cut-out speed rated at 25m/s [11, 25].

2.4 Wind Turbine Generators

Wind turbine generators that are employed in offshore wind farm installations are classified according to the machine and the configuration of the grid interconnection converter as shown in Figure 2-5 below [28, 29].

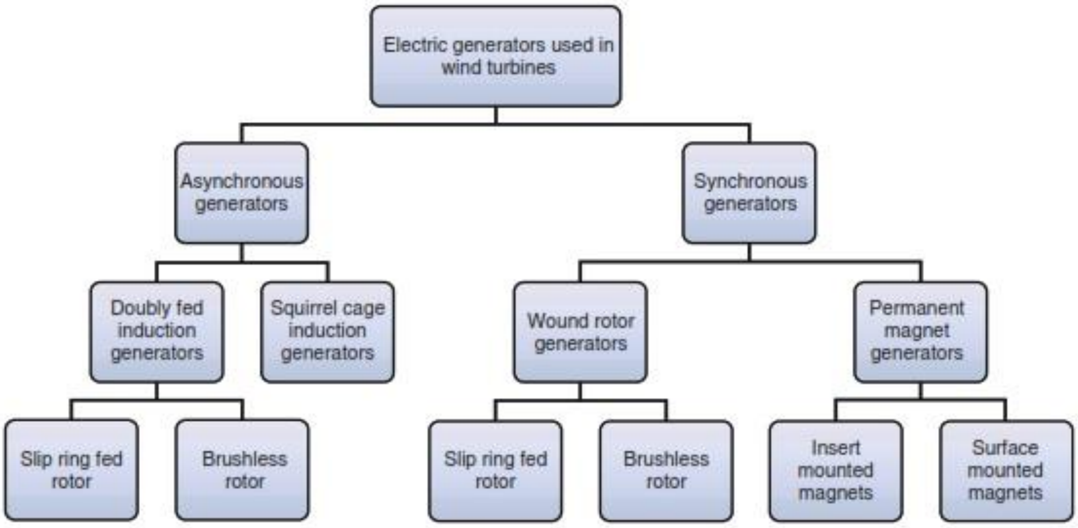

Figure 2-5: Classification of wind turbine generators *[29]*

2.4.1 Type 1 Wind Turbine Generator (Fixed Speed)

Type 1 wind turbine generators consist of a squirrel cage induction generator (SCIG) that is connected to the grid without the application of any electronic converters [30]. The turbine speed of Type 1 generators has a fixed range as the operational slip is not more than 1% [29]. Type 1 turbines also employ a soft-starter within the installation as they consume reactive power during start-up. Reactive power compensation is achieved through the installation of capacitor banks as per Figure 2-6 below. In addition to their low efficiency due to the restricted speed, Type 1 turbines are also affected by any instabilities experienced by the grid [25] [28].

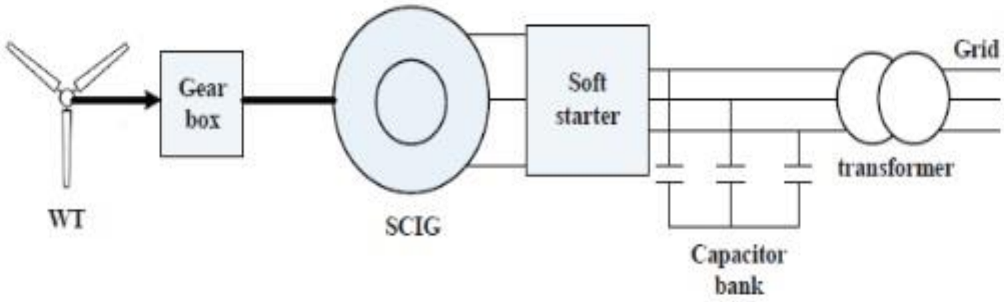

Figure 2-6: Type 1 wind turbine *[28]*

2.4.2 Type 2 Wind Turbine Generator (Limited Variable Speed)

Type 2 wind turbine generators consist of a wound rotor induction generator (WRIG) that is connected to the grid in the same manner as Type 1 generators. Type 2 generators however include a variable resistor that is connected to the rotor coil as shown in Figure 2-7 below. The variable resistor allows the operational slip to be controlled to as much as 10% [28] . The limited speed variation improves the quality of power produced by WRIG. Increased power losses and high maintenance costs are however factors that still make Type 2 generators unfavourable [25] [29].

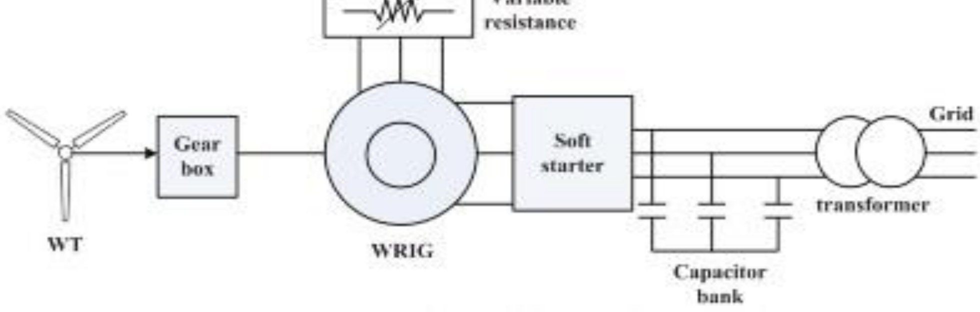

Figure 2-7: Type 2 wind turbine generator *[28]*

2.4.3 Type 3 Wind Turbine Generator (Variable Speed)

Type 3 wind turbine generators consist of a doubly fed induction generator (DFIG) that is linked to the grid through a partially rated AC/DC and DC/AC frequency converter as seen in Figure 2-8 [29]. The turbine can operate at speeds of between -40% - 30% of the synchronous speed thus only transmitting 30% of the rated power from the rotor with the other 70% transmitted directly to the grid [28, 31]. The wide operating range of the turbines and the continuous development of control techniques such as vector and field control, allows the control of active and reactive power in Type 3 wind turbine generators. On the other hand, low efficiency and the cost of the turbine and converters are considered to be demerits of this configuration [29] [32].

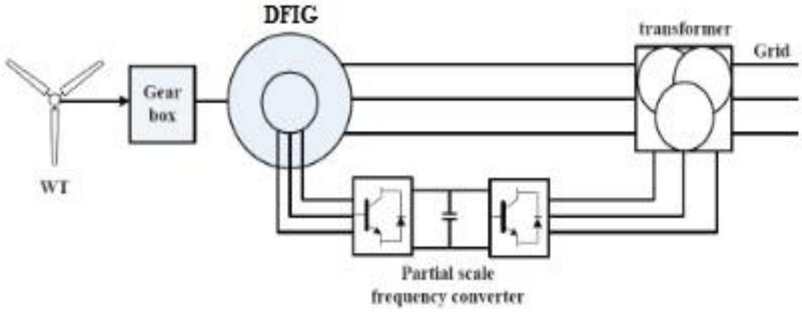

Figure 2-8: Type 3 wind turbine generator *[28]*

2.4.4 Type 4 Wind Turbine Generator (Fully Variable Speed)

Type 4 wind turbine generators consist of a wound rotor induction generator (WRIG) or permanent magnet synchronous generator (PMSG) that is linked to the grid through a fully rated AC/DC /AC back-to-back converter as seen in Figure 2-9. The grid side converter (GSC) maintains a stable DC bus voltage while also providing reactive power compensation. The DC link of the converter also ensures that the turbine system and grid remain decoupled from each other, thereby granting the turbine immunity from faults that may occur in the grid [28] [33]. In some configurations, the gear box may be omitted entirely, allowing the generator to have variable speeds and a wide range of operations translating in the full rated operation of the converter [33]. The cost of the converter installation is, however, a major drawback of this configuration.

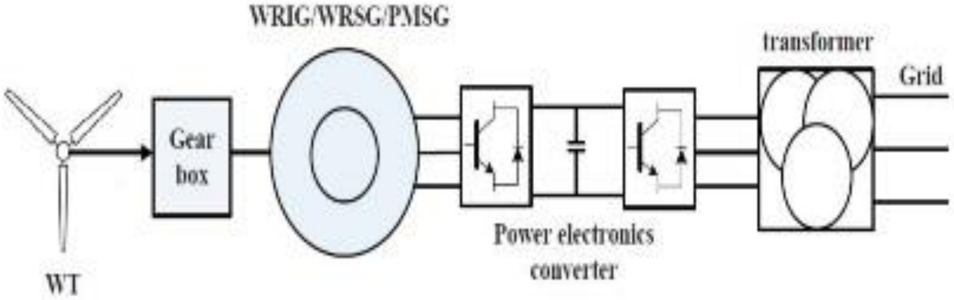

Figure 2-9: Type 4 wind turbine generator *[28]*

2.5 Doubly Fed Induction Generator

In recent years, the integration of offshore wind farms to the onshore Alternating Current (AC) grid has been implemented through the use of Doubly Fed Induction Generators (DFIG) wind energy conversion systems. DFIG generators will be the focus of this study and are widely preferred in the integration of offshore wind farms to the onshore AC grid, due to their numerous benefits, which include [28, 34]:

a) the independent control of active and reactive power;
b) the generation of reactive power;
c) reduced noise levels;
d) reduced size and weight and thus reducing the cost of construction;
e) reduced cost of power electronic converters.

DFIGs are made up of a wound rotor induction generator with the stator being directly supplied by a three-phase ac grid and the rotor is supplied through a back-to-back bidirectional power converter. The two converters operate independently of each other and are referred to as the rotor side converter (RSC) and the grid side converter (GSC) [35].The converters enable the control of active and reactive power through the implementation of vector control strategies. A back-to-back Pulse-width modulation (PWM) is used in order to allow for the DFIG to operate across a wide range of between -40% to 30%. The slip is given by [36]:

$$s = \frac{n_{syn} - n_{gen}}{n_{syn}} \tag{2-28}$$

Where n_{syn} is the synchronous speed and n_{gen} is the generator speed in rpm.

During periods of low wind speeds, the DFIG rotor absorbs reactive power as it is operating below synchronous speed. On the other hand, the DFIG acts as a supply of reactive power during periods of increased wind speed as it operates above the synchronous speed as seen in Figure 2-10 [32].

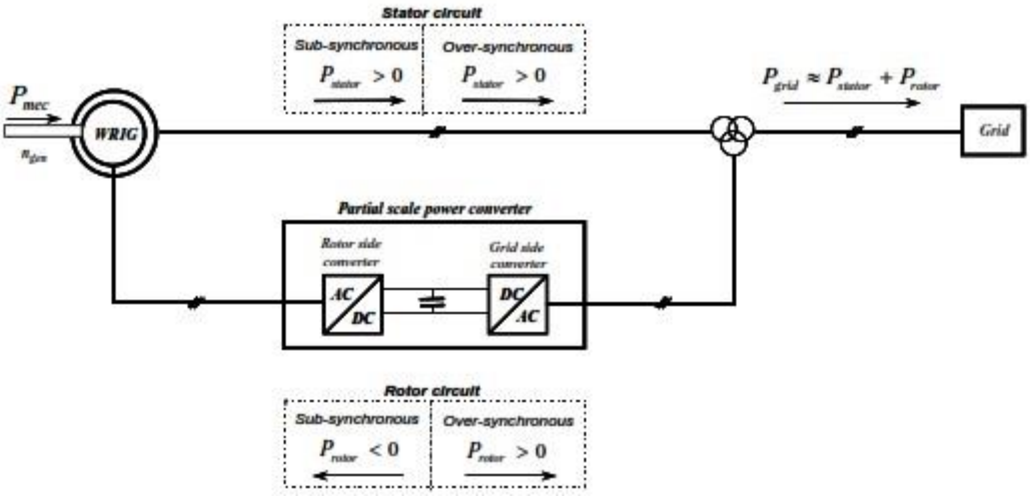

Figure 2-10: Power flow in a DFIG *[36]*

2.5.1 D-Q Transformation Theory

The mathematical analysis of the doubly-fed induction generator is carried out in the direct quadrature (d-q) reference frame. The Clarke-Park and Inverse Clarke-Park Transformation are used to convert three-phase parameters to the d-q reference frame and back as shown in Figure 2-11 and Table 2-2 below [37].

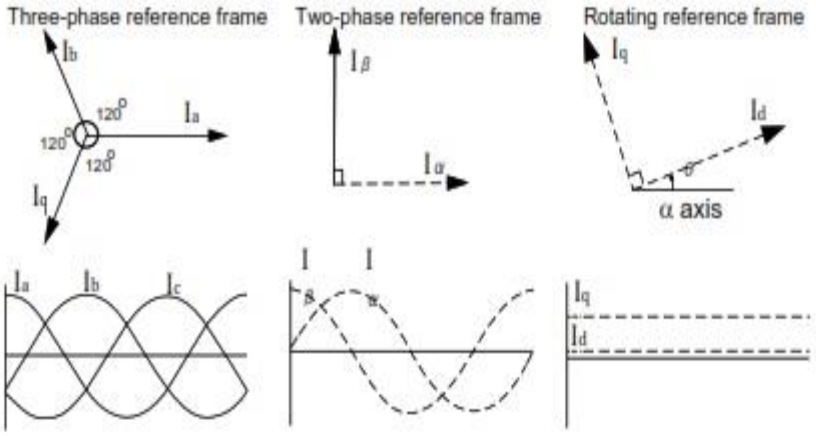

Figure 2-11: d-q transformation theory *[37]*

Table 2-2: d-q transformation theory summary

Reference Frame	**Transformation Method**	**Power System**
a b c to αβ	Clarke Transformation	3Ø AC to 2Ø AC
αβ to d-q	Park Transformation	2Ø AC to 2Ø DC
d-q to αβ	Inverse Park Transformation	2Ø DC to 2Ø AC
αβ to a b c	Inverse Clarke Transformation	2Ø AC to 3Ø AC

2.5.2 DFIG Mathematical Model

The equivalent circuit of the DFIG as modelled in the d-q reference frame is given by Figure 2-12 below [38]:

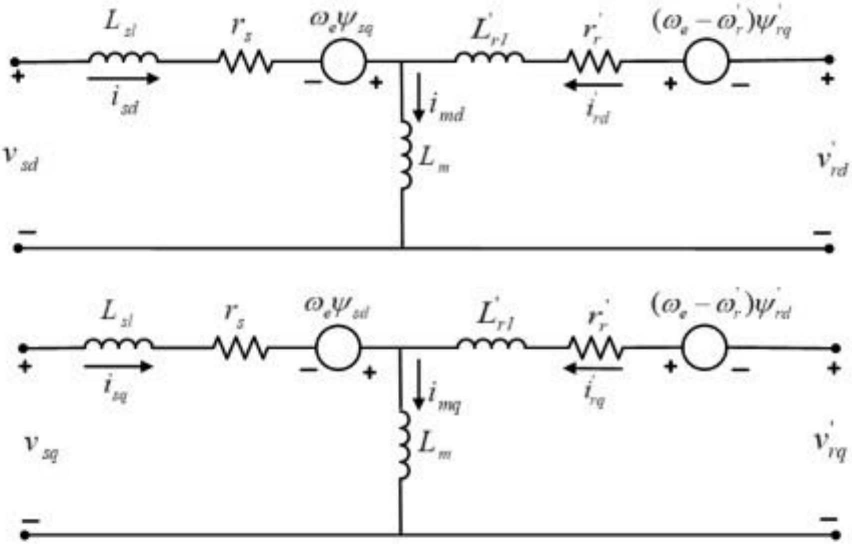

Figure 2-12: Equivalent circuit of DFIG in d-q reference frame *[38]*

The stator voltages are given by Equation (2-29) and Equation (2-30) below [38, 39, 40]:

$$v_{sd} = r_s i_{sd} + \frac{d\psi_{sd}}{dt} - \omega_e \psi_{sq} \qquad (2\text{-}29)$$

$$v_{sq} = r_s i_{sq} + \frac{d\psi_{sq}}{dt} - \omega_e \psi_{sd} \qquad (2\text{-}30)$$

The rotor voltages are given by equations (2-31) and (2-32) below:

$$v'_{rd} = r'_r i'_{rd} + \frac{d\psi'_{rd}}{dt} - \omega_{sl} \psi'_{sd} \qquad (2\text{-}31)$$

$$v'_{rq} = r'_r i'_{rq} + \frac{d\psi'_{rq}}{dt} - \omega_{sl} \psi'_{rd} \qquad (2\text{-}32)$$

The flux linkages are given by Equations (2-33) to Equation (2-36) below:

$$\Psi_{sd} = L_s i_{sd} + L_m i'_{rd} \tag{2-33}$$

$$\Psi_{sq} = L_s i_{sq} + L_m i'_{rq} \tag{2-34}$$

$$\Psi'_{rd} = L'_r i_{rd} + L_m i_{sd} \tag{2-35}$$

$$\Psi'_{rq} = L'_r i'_{rq} + L_m i_{sq} \tag{2-36}$$

Where:

$\omega_{sl} = \omega_e - \omega'_r$

v_{sd} and v_{sq} are the stator voltages in the d-q reference frame.

v'_{rd} and $v'_{rq}$are the rotor voltages in the d-q reference frame.

r_s and r'_r are the stator and rotor phase resistances in the d-q reference frame.

i_{sd} , i_{sq} , i'_{rd} and i'_{rq} are the stator and rotor currents in the d-q reference frame.

ψ_{sd} , ψ_{sq} , ψ'_{rd} and ψ'_{rq} are the stator and rotor fluxes in the d-q reference frame.

L_s , L'_r and L_m are the stator and rotor magnetizing per phase inductances in the d-q reference frame.

ω_e and ω'_r are the synchronous and rotor speed.

The active and reactive power in the stator is given by:

$$P_s = v_{sd} i_{sd} + v_{sq} i_{sq} \tag{2-37}$$

$$Q_s = v_{sq} i_{sd} - v_{sd} i_{sq} \tag{2-38}$$

The active and reactive power in the rotor is given by:

$$P_r = v_{rd} i_{rd} + v_{rq} i_{rq} \tag{2-39}$$

$$Q_r = v_{rq} i_{rd} - v_{rd} i_{rq} \tag{2-40}$$

The electromagnetic torque is given by:

$$T_e = \frac{3}{2} \frac{L_m}{2\, L_s} + \psi_s i_{rq} \tag{2-41}$$

2.6 Power System Operation

The topology of a typical AC power system is built up of the following components as seen in Figure 2-13:

- Generators
- Transmission Lines
- Distribution Lines
- Loads(consumers)

The generation of power is achieved through the use of 3-phase AC synchronous generators in coal, hydro or nuclear power stations. Namibia's main power stations are coal and hydro-powered. The electrical power is generated at small voltages within the range of 11 kV and a frequency of 50 Hz. The electrical power is generated at low voltages as this enables the generators to be relatively smaller in size, thus reducing the cost of construction. The generated power is then stepped up to higher voltages between the range of 132 kV to 700 kV. The electrical power is transmitted at higher voltages and lower currents in order to minimize energy losses. The transmitted electrical power is once again transformed to lower voltages at distribution substations. Distribution voltage levels range between 33 kV to 0.4 kV. Distribution lines (overhead and underground) are then used to supply power to consumers. The consumers are classified as either three-phase customers (0.4 kV) or single-phase customers (0.23 kV) depending on their power requirements [41, 42].

The different generators in an ac grid should always maintain a state of equilibrium with each other and other rotating machines such as loads within the system during operation. However, the ideal state of equilibrium is difficult to maintain as the ac grid is constantly subjected to a number of disturbances such as load changes, transmission line faults, and loss of generation units in some instances. It is, therefore, imperative to maintain synchronism at a grid frequency of 50 Hz while considering the effects of adding or removing both generators and loads from the system [43]. The discussion on power system stability is further explored in section 2.6.1.

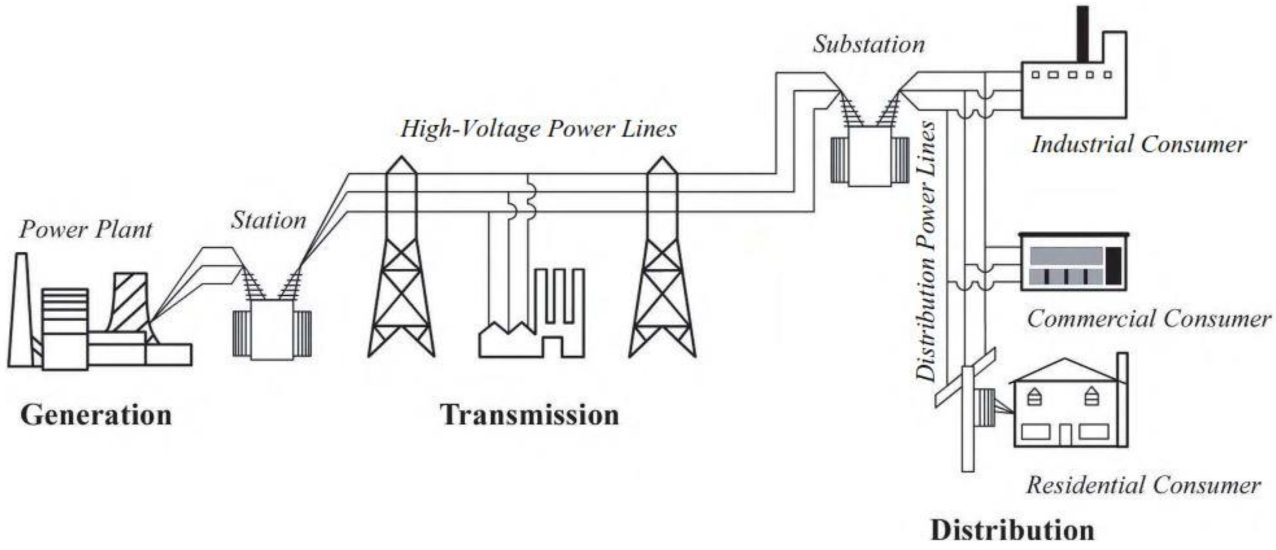

Figure 2-13: Electrical power system overview *[42]*

2.6.1 Power System Stability

Power system stability is defined as the ability of an electric power system, for a given initial operating condition, to regain a state of operating equilibrium after being subjected to a physical disturbance, with most system variables bounded so that practically the entire system remains intact [44].

Power system stability is classified into three categories depending on the severity of the disturbance, the response of system parameters, and the methods used to evaluate the disturbance. The three main categories are rotor angle stability, frequency stability, and voltage stability, as per Figure 2-14 below [44, 45, 46]. The development of converter interfaced generation (CIGs) has resulted in the addition of two new stability classes which are converter driven stability and resonance stability [47]. This study will focus on rotor angle stability, specifically on transient stability, as the interconnection of offshore wind farms to the onshore AC grid significantly affects the rotor angle oscillation of synchronous generators during fault conditions and the power system damping ratio [48]. Moreover, getting a better understanding of the small-signal stability aids in the future development of a suitable control strategy [49].

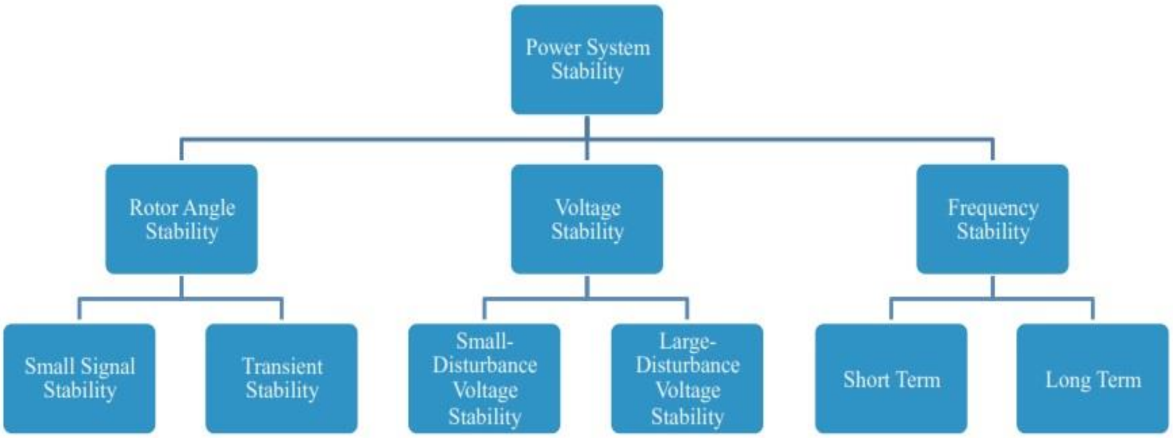

Figure 2-14: Classification of power system stability [46]

2.6.1.1 *Rotor Angle Stability*

Rotor angle stability is the ability of synchronous machines of a power system to remain in synchronism after being exposed to a disturbance. Rotor angle stability fundamentally involves the restoration of equilibrium between the electromagnetic and mechanical torque of synchronous machines in the power system. Should this equilibrium not be achieved, the machines lose synchronism due to the differences in rotor angles. Rotor angle stability studies are normally carried out within 3-20 seconds after the disturbance is experienced and are thus considered to be short-term disturbances [44, 45] [50].

2.6.1.2 *Transient Stability*

Transient stability is the ability of the synchronous machines in a power system to achieve post-fault synchronism after exposure to a large disturbance [44]. Abrupt load changes, transmission line faults and generator faults are some of the contingency events that may affect the transient stability of a power system [51].

2.6.1.2.1 Swing Equation

The swing equation is a differential equation that is used to establish how stable a power system is by taking into account the angular momentum, acceleration power and the rotor angles of generators within the system. Consider a three-phase synchronous generating unit as shown in Figure 2-15 below where:

P_m = mechanical power in MW

P_e = electrical power in MW

T_m= mechanical torque in N-m

T_e= electrical torque in N-m

ω = rotor angular speed in rad/s

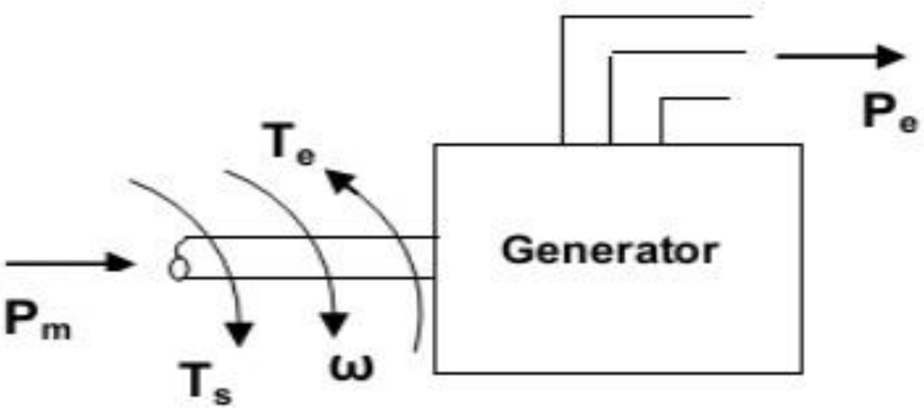

Figure 2-15: Three-phase synchronous generating unit *[52]*

The equation of motion as determined by Newton's second law is given by:

$$T_a = T_m - T_e = J\alpha_m \tag{2-5}$$

Where:

T_a = net accelerating torque in N-m

J= total moment of inertia of the rotating masses in kg-m^2

$\alpha_m = \frac{d^2\theta_m}{dt^2}$, is the rotor angular acceleration in rad/s^2 (2-6)

θ_m is the rotor angular position with respect to a stationary axis and is measured in reference to a synchronously rotating frame.

$$\theta_m = \omega_{ms}t + \delta_m \tag{2-7}$$

Where:

ω_{ms} is the synchronous angular velocity of the rotor in rad/s

δ_m is the rotor angular position (rad) in respect to a synchronously rotating frame

In a steady state, the electromechanical torque (T_e) is equal to the mechanical torque (T_m) and the accelerating torque (T_a) is zero. Equation (2-5) also shows that the rotor speed increases or decreased depending on whether the accelerating torque (T_a) is positive or negative.

Substituting (2-6) and (2-7) into (2-5) results in:

$$T_a = T_m - T_e = J\frac{d^2\theta_m}{dt^2} = J\frac{d^2\theta_m}{dt^2} \tag{2-8}$$

Multiplying (2-8) by ω_m on both sides results in:

$$P_a = P_m - P_e = J\omega_m\frac{d^2\delta_m}{dt^2} \tag{2-9}$$

Where:

P_a is the accelerating power

In order to simplify the equation, the normalised inertia constant (H) is used.

$$H = \frac{stored\ kinetic\ energy\ at\ synchronous\ speed}{generator\ voltampere\ rating} = \frac{j\omega_{ms}^2}{2S_{rated}}\ joules/VA \tag{2-10}$$

Substituting Equation (2-10) into Equation (2-8) and dividing by the generator MVA rating (S_{rated}) results in the per-unit Swing Equation below.

$$P_a = P_m - P_e = \frac{2H}{\omega_{ms}}\frac{d^2\delta}{dt^2} = \frac{Hd^2\delta}{\pi f dt^2} \tag{2-11}$$

Where:

δ is the power angle in electrical radians and 2πf is the radian frequency in radians/s

Swing curves are obtained as a result of solving the swing equation. A power system is considered to be stable should the power angle oscillations decrease after reaching a maximum value as shown in Figure 2-16 below. This implies that $\frac{d\delta}{dt} = 0$ at some instant during the oscillations. On the other hand, a continually increasing power angle depicts an unstable power system [53, 54, 52, 55].

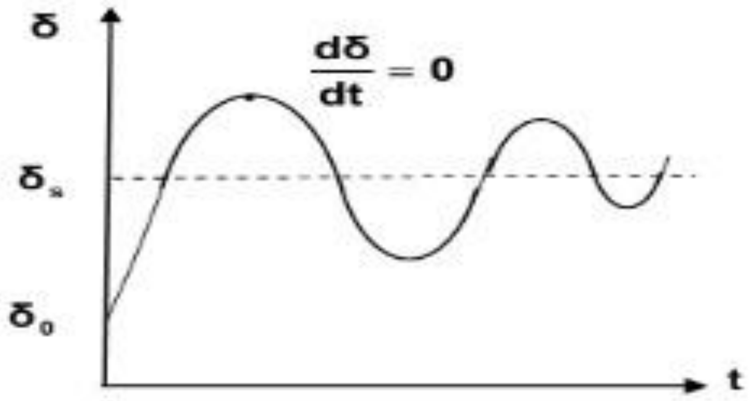

Figure 2-16: Swing curve depicting stable system *[52]*

2.6.1.2.2 Power-Angle Relationship

The active power delivered to an infinite bus by a synchronous generator is given by Equation (2-12) below.

$$P_e = \frac{|E_g||V_t|}{X_{eq}} \sin\delta \tag{2-12}$$

Where $|E_g|$ is the generator internal voltage, $|V_t|$ is the terminal voltage, δ is the power angle and X_{eq} is the equivalent synchronous reactance. The power-angle curve is a graphical representation of the power angle (δ) in relation to the output power that can be delivered from a synchronous generator (P_e) without affecting the transient stability.

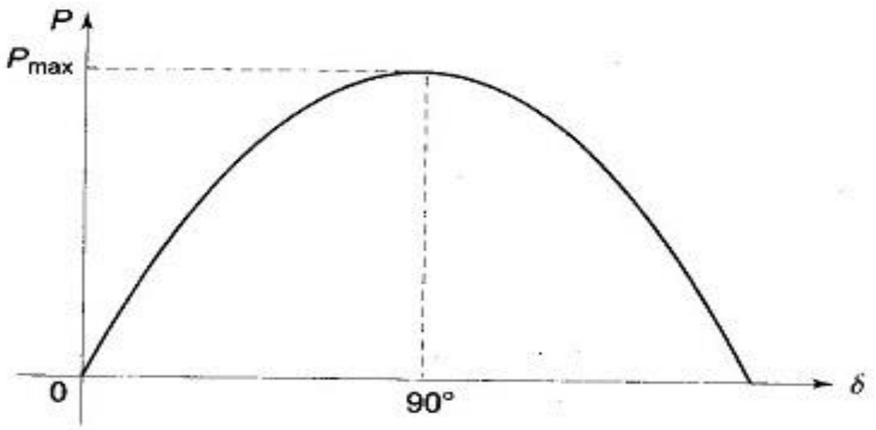

Figure 2-17: Power-angle curve *[56]*

From Figure 2-17 above, it can be seen that the output power (P_e) from a synchronous generator increases proportionally to the power angle (δ) until it reaches a maximum value at 90°. The output power decreases when the power angle (δ) increases to more than 90° as the synchronous generator starts to lose synchronism. δ = 90° is therefore said to be the synchronous generator's steady-state stability limit. The maximum power is given by Equation (2-13) [53, 54, 52, 56].

$$P_{max} = \frac{|E_g||V_t|}{X_{eq}} \tag{2-13}$$

2.6.1.2.3 The Equal-Area Criteria

The equal-area criterion is a graphical method that is used in transient stability analysis. The equal-area criterion is used to determine how long it would take for a short-term fault to be cleared before the synchronous machines of a power system lose their synchronism [57, 58].Consider the Swing Equation (2-11):

$$P_a = P_m - P_e = \frac{2H}{\omega_{ms}}\frac{d^2\delta}{dt^2} = \frac{Hd^2\delta}{\pi f dt^2} \tag{2-11}$$

Multiplying (2-11) by $\frac{d\delta}{dt}$ on both sides results in:

$$\frac{1}{2}\frac{H}{\pi f}\frac{d}{dt}\left(\frac{d\delta}{dt}\right)^2 = P_a\frac{d\delta}{dt} \tag{2-14}$$

Rearranging and integrating (2-14) results in:

$$\frac{d\delta}{dt} = \sqrt{\frac{2\pi f}{H}\int_{\delta_o}^{\delta} P_a d\delta} \tag{2-15}$$

Where δ_o is the torque angle when the synchronous machines are in operating equilibrium. During equilibrium, the torque angle does increase or decrease and thus $\frac{d\delta}{dt} = 0$.

The condition for transient stability is defined by:

$$\int_{\delta_o}^{\delta} P_a d\delta = 0 \tag{2-16}$$

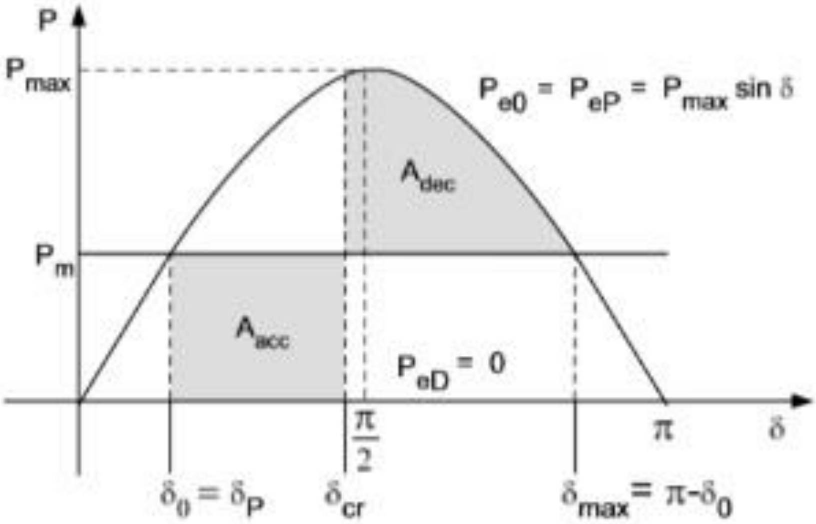

Figure 2-18: Equal-area criteria curve *[58]*

During the occurrence of a fault, the accelerating power (P_a) increases as the generator's kinetic energy increases as illustrated by the accelerating area (A_{cc}) in Figure 2-18 above. Once the fault is cleared, the generator decelerates, and the stored energy is released as illustrated by the decelerating area (A_{dec}) in Figure 2-18 above. The power angle (δ) of the machine only reaches a maximum value (δ_m) when A_{cc} is equal to A_{dec}.The equality of the two areas is referred to as the equal-area criterion. The fault should be cleared before the critical clearing angle (δ_{cr}) is reached in order to ensure the stability of the synchronous machine. Thus, the critical clearing time (CCT) is the time in which a fault should be cleared before losing stability and is a function of the critical clearing angle [52, 57, 58, 59].

2.6.1.3 *Small-signal Stability*

Small-signal stability is the ability of the synchronous machines in a power system to achieve post-fault synchronism after exposure to a small disturbance [44]. Small-signal stability analysis is carried out using linearized equations and state-space form as the disturbances experienced by the power system are considered minute in nature. Small-signal instability is mostly experienced due to discrepancies in the damping torque as the rotor angle increases [60, 61].

2.6.1.3.1 State-space Representation

A nominal operating point is used for the linearization of the first-order non-linear equations that describe a power system. The linearized state-space equations are given by:

$$\Delta\dot{x} = \boldsymbol{A}\Delta x + \boldsymbol{B}\Delta u \qquad (2\text{-}17)$$

$$\Delta y = \boldsymbol{C}\Delta x + \boldsymbol{D}\Delta u \qquad (2\text{-}18)$$

Where A, B, C and D are the state matrix, input matrix, output matrix, and feed-forward matrix respectively. Δx,Δy and Δu are the state vector, output vector and input vector respectively. The vectors represent the incremental changes of the matrices [62, 63].The Laplace Transform is the equation used to solve the state-space equation in matrix form.

$$s\Delta\boldsymbol{x}(s) - \Delta\boldsymbol{x}(0) = \boldsymbol{A}\Delta\boldsymbol{x}(s) + \boldsymbol{B}\Delta\boldsymbol{u}(s) \qquad (2\text{-}19)$$

$$\Delta\boldsymbol{y}(s) = \boldsymbol{C}\Delta\boldsymbol{x}(s) + \boldsymbol{D}\Delta\boldsymbol{u}(s) \qquad (2\text{-}20)$$

$$(\boldsymbol{sI} - \boldsymbol{A}) - \Delta\boldsymbol{x}(s) = \Delta\boldsymbol{x}(0) + \boldsymbol{B}\Delta\boldsymbol{u}(s) \qquad (2\text{-}21)$$

The solution of Equation (2-21), which is the characteristic equation of **A** results in eigen values that are used in small-signal stability analysis [64, 65].

$$\det(sI - A) = 0 \qquad (2\text{-}22)$$

2.6.1.3.2 Eigen Value Analysis

Eigen values and modal analysis are used in the study of small-signal stability of a system. The solution of Equation (2-22) using Lyapunov’s first method results in understanding the generators' operation modes, damping, and speed. A plot of complex eigen values on the s-plane as per Figure 2-19 below makes small-signal stability analysis easier.

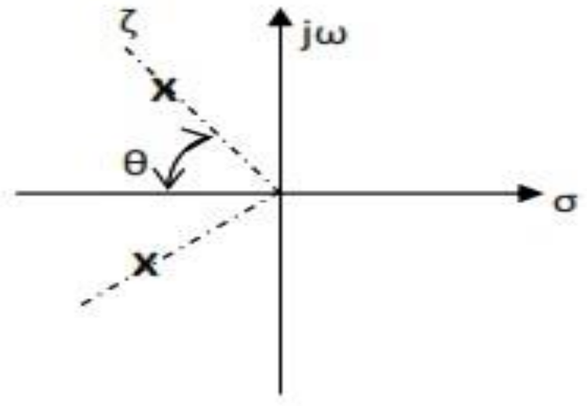

Figure 2-19: Eigen value on s-plane *[66]*

The eigenvalues can be written into a real part (σ) that represents the damping value and imaginary part (ω) that represents the frequency of oscillation as stated by equation (2-23).

$$\lambda = \sigma \pm j\omega \tag{2-23}$$

The frequency of oscillation in hertz is given by:

$$f = \frac{\omega}{2\pi} \tag{2-24}$$

The rate at which the oscillation experiences decay in terms of the amplitude is given by the damping factor (ς) in percentage (%). The damping factor is considered to be acceptable at values of greater than 5%.

$$\varsigma = \frac{-\sigma}{\sqrt{\sigma^2+\omega^2}} \tag{2-25}$$

Based on Lyapunov's First Criteria and considering Equation (2-21) the following applies [25, 67, 66]:

- The system is said to be asymptotically stable if all the eigen values of matrix **A** have a negative real part. That is, they are all plotted on the left half plane.
- The system is said to be unstable if at least one of the eigen values of matrix **A** has a positive real part.
- It is not possible to determine the stability of a system if at least one of the eigen values of matrix A is located on the imaginary axis while all the other eigen values have a negative real part.

The left and right eigen vectors of the state matrix **A** are given by:

$$A_{vi} = V_i\lambda_i \tag{2-26}$$

$$w_iA = \lambda_iw_i \tag{2-27}$$

Where v_i is the right eigen vector and w_i is the left eigen vector.

The right eigen vector accounts for the shape of the mode whereas the left eigen vector accounts for the controllability of the mode as it significantly influences the amplitude of the mode [65, 67].

2.6.1.3.3 Power Oscillation Damping

Electromechanical oscillations of numerous interconnected generators in a power system cause power oscillation in a power system. Low-frequency oscillations (0.2-2 Hz) that last for an extended period of time without being damped will cause a power system to lose its stability which eventually lead to blackouts in some instances. The analysis of eigen values is instrumental as it is used to determine the dominant oscillation mode of power systems, thus making the development of a damping strategy easier. Low-frequency oscillations modes are classified as either local mode or interarea mode. In local mode, generators within the same locality oscillate at homogeneously higher frequencies as they have a strong electrical link. Whereas in interarea mode, generators in the same locality oscillate against generators in neighbouring areas at homogeneously lower frequencies as they have a weak electrical connection [68]. Power oscillation damping can be achieved through the application of FACTS devices such as, static synchronous series compensators (SSSC) [69].

2.6.1.4 *Voltage Stability*

The ability of a power system to maintain acceptable voltage levels at its busbars after being subjected to a contingency event is referred to as voltage stability [44].

2.6.1.4.1 Short-term Voltage Stability

Short-term voltage stability, as the name implies, is the short-term response of the power system to large disturbances such as changes in dynamic motor loads [70]. Due to its nonlinear nature, short-term voltage stability is studied within a few seconds. Voltage instability may lead to voltage collapse in weak networks due to the excessive current requirements of induction motors and other mechanical loads during fault conditions. [71]. Short-term voltage has also been documented to affect small networks that have larger offshore wind farms in relation to conventional generation power plants [72]. It is therefore advisable to monitor short-term voltage stability when carrying out projects that require the integration of offshore wind farms to onshore networks.

2.6.1.4.2 Long-Term Voltage Stability

Long-term voltage stability, as the name implies, is the long-term response (5 to 30 minutes) of a power system in terms of load restoration after being subjected to a large distance [73]. Long-term voltage instability may be affected by the inability of the available generators within a network. Moreover, networks in which the generating stations are remotely located from load centres may also experience long-term voltage instability [74]. Flexible AC Transmission devices such as shunt capacitors and reactors are used as a method of improving long-term voltage stability. VSC-HVDC links are also used to improve long-term voltage stability due to their ability to independently control active and reactive power [75].

2.6.1.4.3 Voltage Stability Analysis

Voltage stability analysis aims to highlight the stability margins of the network and may be carried out by using the following methods:

- P-V curve method
- P-Q curve method
- Continuation power flow method

2.7 Namibian Power System

2.7.1 Namibia’s Existing Generation Capacity

Namibia’s current peak energy demand currently stands at approximately 744 MW, and this is expected to grow to approximately 768 MW by the year 2022. The current maximum local installed generation capacity is only 511 MW as shown in Table 2-3 below. This local capacity is supplemented by an imported capacity of 430 MW which translates to almost 50% of the total installed capacity. The Namibian government has indicated that they plan to increase the local installed capacity by 220 MW through a mixture of generation scenarios beyond the year 2020. 150 MW of the 220 MW has been allocated to the national utility NamPower with the remaining 70 MW being allocated to independent power producers (IPPs) on a competitive basis [76].

Table 2-3: Namibia's existing power generation capacity *[76]*

Generating Stations	**Technology**	**Capacity (MW)**
Ruacana	Hydro	347
Van Eck	Coal	10
Anixas	Diesel	22.5
Omburu	PV	4.5
Greenam	PV	20
Hardap	PV	37
REFIT Programme	PV & Wind	70

Figure 2-20: NamPower transmission network master plan *[76]*

2.7.2 Namibia’s Load Forecast

NamPower carried out long-term forecasting studies over a 40-year period (2003-2042). The load forecast as shown in Figure 2-21 below indicates that Namibia’s demand is expected to grow to about 861 MW in ten years and to about 962 MW in the year 2042 [76]. The load forecast is an important tool in determining the investments that should be made in generation, transmission, and distribution infrastructure to achieve self-sustainability.

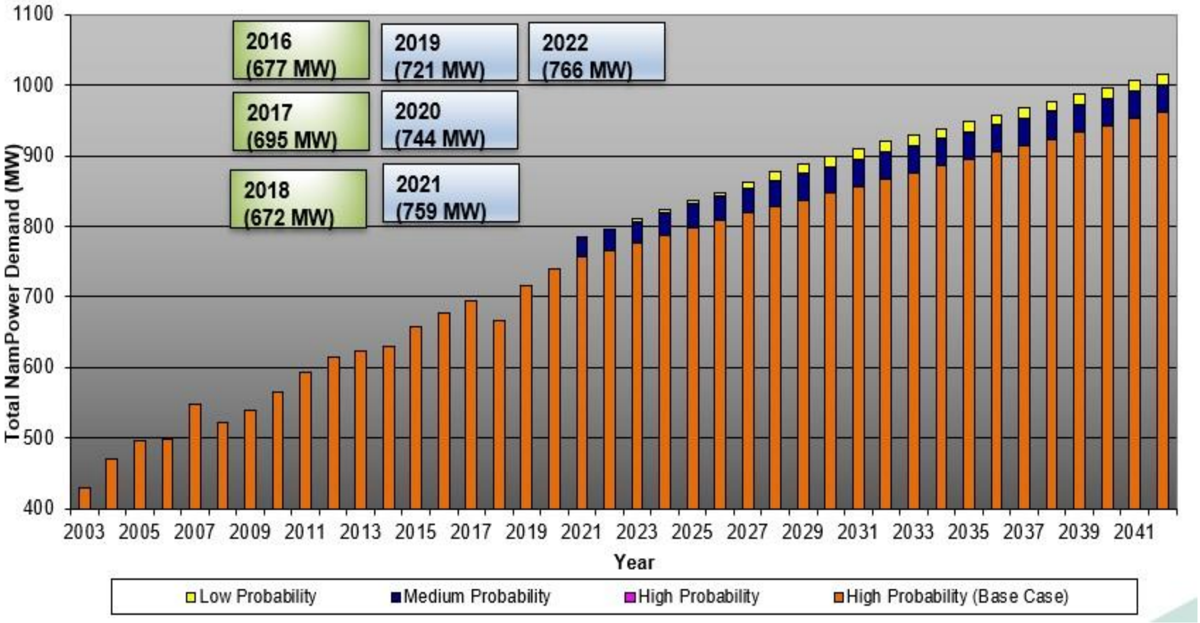

Figure 2-21:Namibia's electricity load forecast :2018-2042 *[76]*

2.8 Grid Code

Grid codes are the minimum technical specifications that must be met by any generation facility or load that is to be interconnected to the national electrical grid. The grid codes ensure that the electricity system remains safe and continues to operate when faults occur. The most accepted interconnection criteria for offshore wind farms include the following [77]:

- Dimensioning voltages and frequencies
- Voltage control and reactive power output requirements
- Low voltage ride-through capability (LVRT)
- Frequency control

Generation facilities are required to remain connected to the electrical grid during periods of under-voltage. This criterion is referred to as low voltage ride-through capability (LVRT), which has greatly improved the transient stability of the electrical grid. The use of VSC-HVDC links as an interconnecting technology further strengthens the low voltage ride-through capability of offshore wind farms as it grants them immunity from faults that may occur at the onshore electrical grid [78].

The Namibian Grid Code does not explicitly give interconnection criteria for offshore wind farms, but rather for all renewable energy plants. The grid code states that transient stability should be achieved after a fault's clearance and that a renewable energy plant should remain connected to the network as a means of low voltage ride-through as depicted in Figure 2-22 below. Sub code (2) of code 235 details the conditions under which disconnection of the renewable energy plants under low-voltage conditions is allowed [79].On the other hand, the South African Grid Code explicitly defines the criteria for interconnection of renewable power plants (RPPs) including offshore wind farms. The renewable power plants (RPPs) are further divided into three categories:

1. Category A: 0-1 MVA
2. Category B: 1 MVA – 20 MVA
3. Category C: 20 MVA and higher

As per the South African Grid Code requirements, RPPs are required to supply or absorb reactive power during fault conditions. The RPPs should maintain interconnection for a period of 2 seconds for over-voltage conditions of up to 120 % at the point of common coupling. The RPPs should also maintain interconnection for a period of 0.15 seconds for under-voltage conditions of up to 0 volts at the point of common coupling [80].

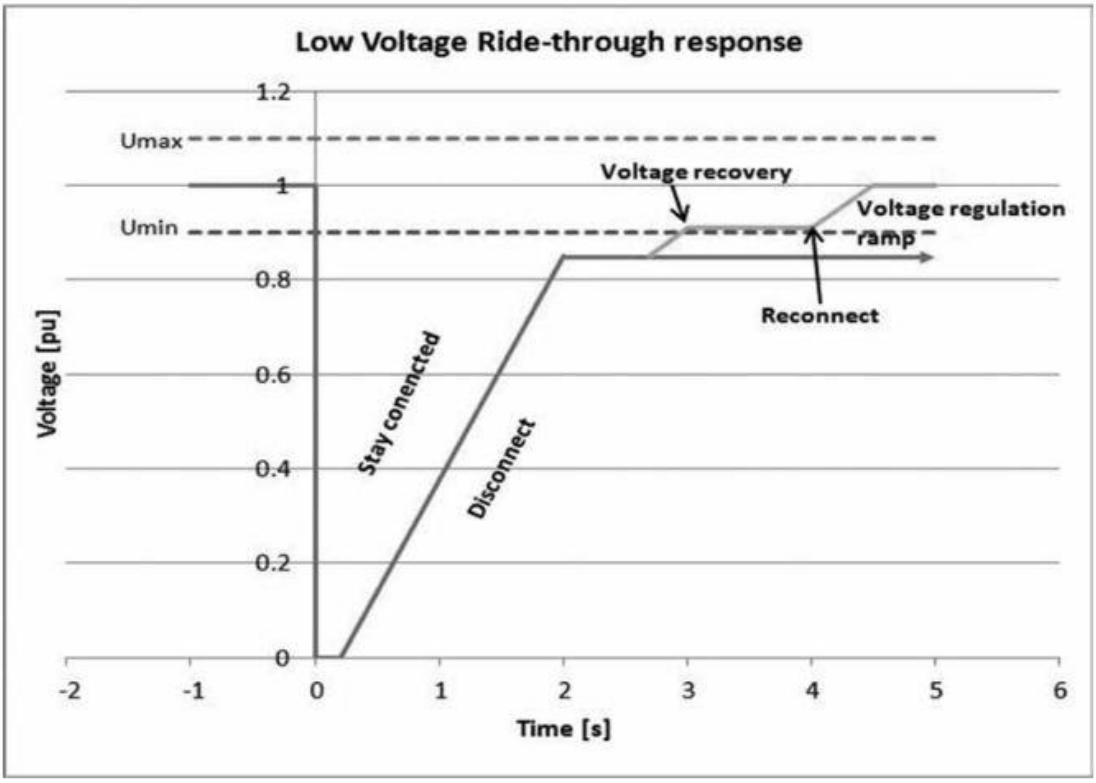

Figure 2-22: Namibian grid-code renewable plant on low-voltage ride- through response *[79]*

2.9 Bulk Power Transmission

The development of offshore wind farms includes their integration to the onshore AC grid. The integration and delivery of power can be achieved either through the use of High Voltage Alternating Current (HVAC) technology or High Voltage Direct Current (HVDC) technology. The application of HVAC technology has however been found to be unsuitable for distances that are longer than 50 km and for wind farms that generate over 100 MW of power. HVAC transmission systems have become greatly uneconomical for bulk power transfer as they regularly suffer from asymmetric faults that result in high current conditions. These high currents affect the cost of protection devices as the higher the short circuit current of the system, the more costly the protection devices in terms of the design [81].Moreover, HVAC transmission systems are considered to be less reliable than HVDC transmission systems as they do not fully allow the control of the transmitted power. HVAC transmission systems are also affected by corona loss, the skin effect as well as cable charging currents over extended distances. These factors coupled with the inability of HVAC transmission systems to link asynchronous grids further reduce their technical preference in terms of reliability and stability [82].

There are currently two main HVDC technologies that are widely implemented in the integration high voltage systems. The two technologies are LCC-HVDC which is based on line commutated converters and VSC-HVDC which is based on voltage source converters. Of the two, VSC-HVDC has been highly developed in the integration of offshore wind farms. This study focused on VSC-HVDC as the interconnecting and transmission technology [83, 84].

2.9.1 LCC-HVDC

Line Commutated Converters High Voltage Direct Current (LCC-VHDC) which is also referred to a current source converter (CSC), uses thyristors as the main switching element in the transmission of power over long distances. LCC-HVDC does not support black-start capability as thyristor switches require an external ac voltage for commutation. LCC-HVDC is considered to be a matured technology since it was applied in the transfer of bulk power over 50 years ago. The ability to transfer a large capacity of power as well as low power losses due to lower frequencies are some of the main advantages of LCC-HVDC [85, 86].

The components of an LCC-HVDC transmission system include the following [87]:

2.9.1.1 *The Power Converter*

The power converters used in LCC-HVDC are thyristors switches that achieve commutation by using the ac system voltage. The converters which are referred to as current source converters (CSC), ensure the conversion of power from AC/DC at the sending end and then DC/AC at the receiving end. The converters are normally arranged in a 12-pulse topology.

2.9.1.2 *The Converter Transformer*

The converter transformer is used to transform the AC voltage to the valve bridges to a suitable operating range for the valves. The on-load tap changers also aid in reducing the steady state power demands of the power converters.

2.9.1.3 *AC and DC Harmonic Filters*

The operation of LCC-HVDC power converters produces harmonic components which affects the produced AC waveforms and increases power losses. Harmonic filters are installed in order to absorb the resultant harmonic components and provide reactive power compensation.

LCC-HVDC is however not the preferred technology for offshore wind farm integration as it also requires support from the ac grid which may lead to voltage and frequency instability. The inability to support the independent control of active and reactive power is another factor that limits the use of LCC-HVDC in the integration of offshore wind farms to an onshore ac grid [86, 87].

2.9.2 VSC-HVDC

VSC-HVDC technology uses self-commutating insulated gate bipolar transistors (IGBTs) as the main switching technology in the transmission of power from remotely located offshore wind farms to the onshore AC grid. The use of IGBTs enables the technology to turn-on and turn-off a voltage source. In recent years, the development of VSC-HVDC technology has been dominated by ABB (HVDC Light), Siemens (HVDC PLUS), ALSTOM (MaxSine) and C-EPRI (HVDC Flexible) [83, 88]. VSC-HVDC is an efficient transmission technology as it results in minimal power losses ranging between 1-2%. Furthermore, VSC-HVDC has also enabled the transmission of large amounts of power from offshore wind farms to the onshore AC grid starting with as little as 44 MW at 70 km in 2005 to as much as 1400 MW being transmitted. In Europe, HVDC cables are also considered to be much cheaper than AC cables per kilometre as they do not consume reactive power [89, 90]. The advantages of implementing VSC-HVDC technology in respects of offshore wind farms far outweigh the disadvantages, thus making it a suitable technology as seen in Table-2-4 below [88, 90].

Table 2-4: Advantages and disadvantages of VSC-HVDC

Advantages of VSC-HVDC	Disadvantages of VSC-HVDC
Independent control of active and reactive power	Converters are highly priced
Black start capability	Harmonics are generated due to operation of the converters.
Ability to connect passive or weak ac networks	
Multi-terminal grid systems can be achieved	
The losses of DC lines are considered to be low at high voltages	
Reduced risk of commutation failure due to the use of IGBTs	

Other applications of VSC-HVDC technology include the following:

- Power from onshore
- Connecting remote loads
- Interconnections
- DC links in AC grids
- City centre infeed

2.9.3 VSC-HVDC Configurations

HVDC systems are classified into four main configurations which are monopolar, bipolar, back-to-back and multiterminal [91, 92].

2.9.3.1 *Monopolar VSC-HVDC*

In this topology, two converter stations are connected by a positive or negative single pole DC transmission line with the ground being used as a return as shown in Figure 2-23 [91, 92, 93].

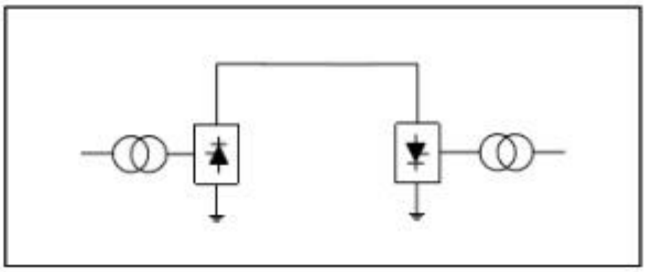

Figure 2-23: Monopolar configuration *[91]*

2.9.3.2 *Bipolar VSC-HVDC*

In this topology, two monopolar links are connected using transmission lines with both positive and negative polarity relative to the ground as shown in Figure 2-24 below. This improves reliability as one pole can be used for transmission should the other pole fail [91, 92, 93].

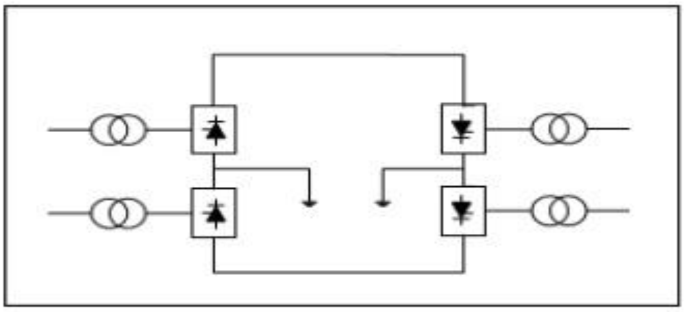

Figure 2-24: Bipolar configuration *[91]*

2.9.3.3 *Back-to-back VSC-HVDC*

Two asynchronous converter stations located at the same site are connected together via a DC link without the use of a transmission lines as depicted in Figure 2-25 below [91, 92, 93].

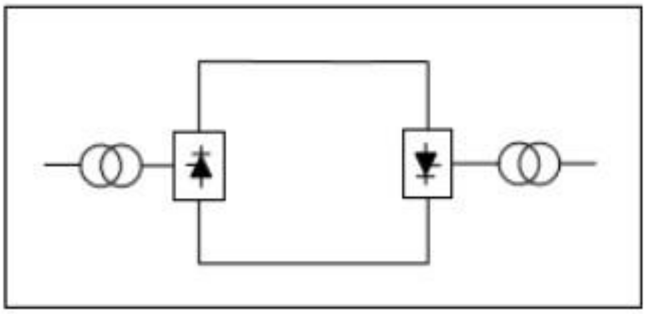

Figure 2-25: Back-to-back configuration *[91]*

2.9.3.4 *Multi-terminal VSC-HVDC*

In this topology, three or more converter stations are interconnected in series or parallel depending on the application as shown in Figure 2-26. Some of the converters are operated as rectifiers with the rest operating as inverters [91, 92, 93].

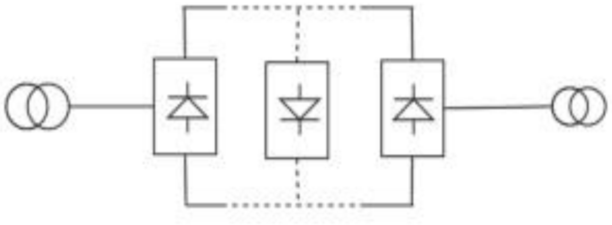

Figure 2-26: Multi-terminal configuration *[92]*

2.9.4 VSC-HVDC Components

The components of a VSC-HVDC transmission system as depicted in Figure 2-27 include the following [93]:

2.9.4.1 *Converters*

VSC-HVDC systems make use of Insulated Gate Bipolar Transistors (IGBTs) as the main converter technology. The converters are used as a rectifier at the sending end and an inverter at the receiving end. The converters are installed as per the configurations that have already been discussed above.

2.9.4.2 *Filters*

The commutation of the IGBTs used in VSC-HVDC systems results in voltage and current waveforms that have high order harmonics. High-pass passive filters are therefore used to correct this harmonic distortion.

2.9.4.3 *Transformers*

The transformer is used to maintain voltage levels that are suitable for the operation of the VSC-HVDC semiconductor switches.

2.9.4.4 *Smoothing Reactors*

Smoothing reactors control both the reactive and active power flow along with carrying out harmonic filtering.

2.9.4.5 *HVDC Cables*

HVDC submarine cables are used for the transmission of large amounts of power as they are light and do not consume reactive power over long distances. Extruded polyethylene cables are commonly used in recent times due to their added benefits.

2.9.4.6 *HVDC Breakers*

HVDC breakers are used to shield the HVDC system from the faults experienced by the rest of the transmission system.

2.9.4.7 *HVDC Capacitors*

Two equally sized capacitors are used in order to ensure that there are minute voltage ripples on the DC side of the system.

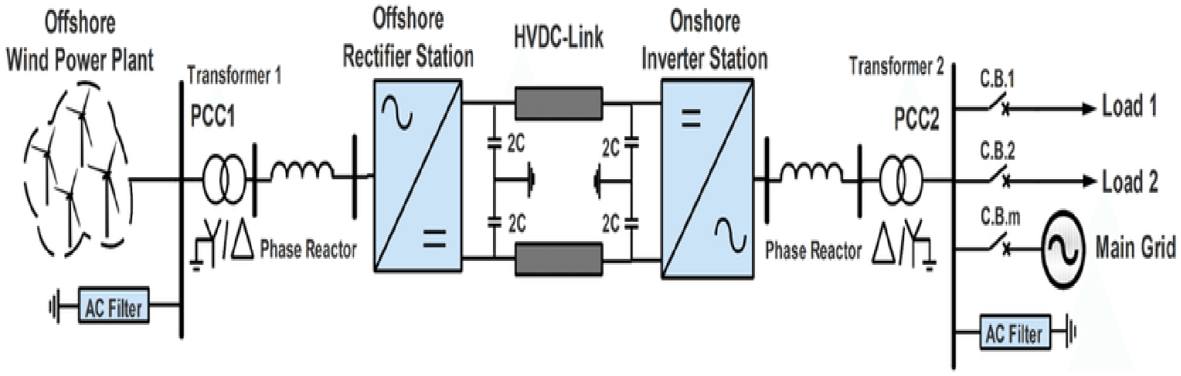

Figure 2-27: VSC-HVDC link *[94]*

2.9.5 VSC-HVDC Control Strategies

The control strategy that is adopted and implemented plays a significant role in the desired operation of the VSC-HVDC system as well as in maintaining the overall system stability [91]. It is therefore imperative to select the correct control parameters with the aim of achieving independent control of the active and reactive power [95].

2.9.5.1 *Direct Control*

This control strategy is not complex in its implementation as it is carried out in the three-phase frame. However, the direct control strategy does not employ any inner-current control loop and therefore there is no overcurrent protection for the converter valves as shown in Figure 2-28 and Figure 2-29. Another factor that makes this strategy less common is the variability of the switching frequency [96, 97].In addition to shortfalls in the switching frequency, this control strategy does also not allow the independent control of active and reactive power as the change in either the voltage or current affects the other parameters [91]. The active and reactive power are however directly controlled through the use of a switching table [98].

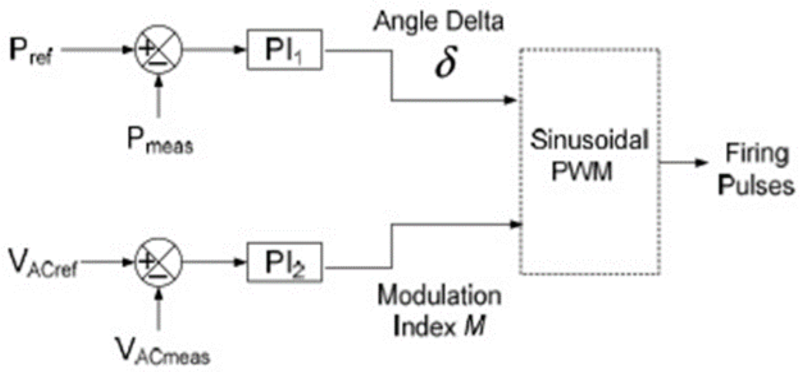

Figure 2-28: Direct control strategy sending-end block *[98]*

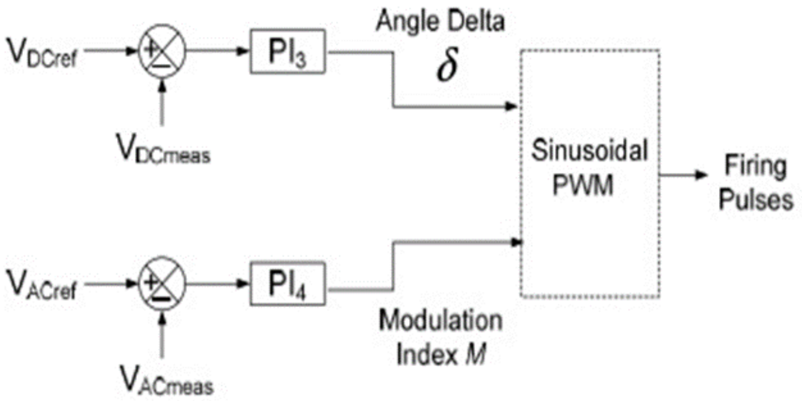

Figure 2-29: Direct control strategy receiving-end block *[98]*

2.9.5.2 *Vector Control*

Vector-oriented control strategy is complex as it is carried out in the d-q axis reference frame. A phase-locked loop (PLL) is used to synchronize the d and q currents in the rotating reference frame by locking them to the three-phase voltage. The d and q components of the currents with reference to the sending end three phase voltage control the active and reactive power through a rectifier and inverter as per equation (2-42) and (2-43) below. The outer voltage controller maintains the dc voltage between the two converter stations and ensures that the ac voltage is maintained at the correct magnitude.

$$P = \frac{3}{2}(Vs_{id}) \tag{2-42}$$

$$Q = -\frac{3}{2}(Vs_{iq}) \tag{2-43}$$

Where Vs is the sending end voltage, i_d and i_q are the d and q current components respectively.

The separation of currents in the d and q reference axis is carried out in the inner current loop. The resulting signals from the inner current loop are forwarded to the converter after transformation to the three-phase frame as shown in Figure 2-30. The independent control of active and reactive power coupled with fast dynamic response is one of the main reasons why the vector control strategy is the most common control strategy for VSC-HVDC systems [91, 95, 97, 99].

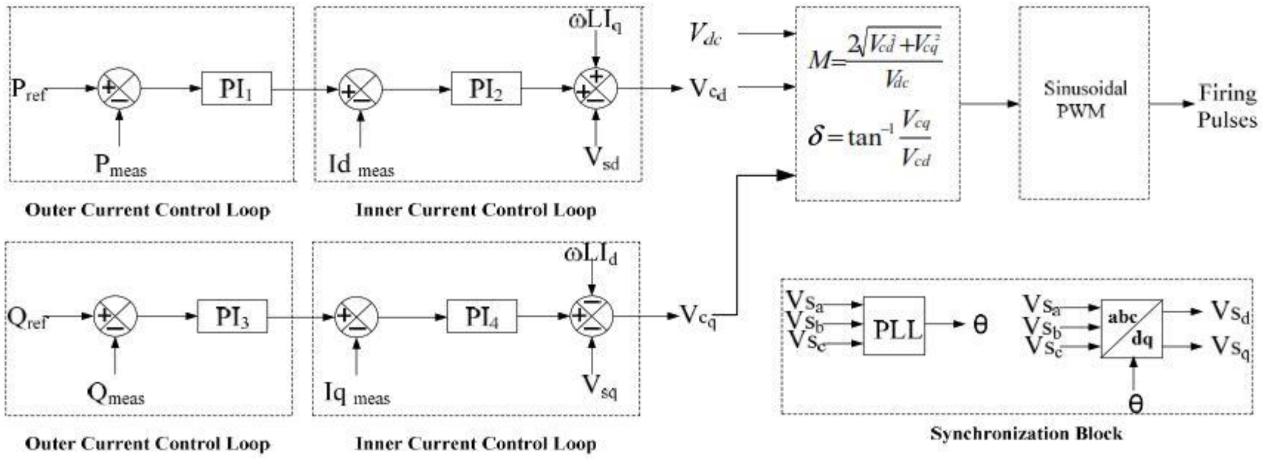

Figure 2-30: VSC-HVDC vector control strategy *[98]*

2.9.6 Existing VSC-HVDC Projects

2.9.6.1 *BorWin3*

BorWin3, which was commissioned in 2019, is a project initiated by TenneT, a joint German-Dutch network operator. The grid connection system has a capacity of 900 MW, whereas the offshore wind farm has the capacity to produce 500 MW of power. This power is then transferred over a ±320 kV VSC-HVDC link from the North Sea to the German shore through a subsea cable. The power is integrated to the German onshore ac network via two 666 MVA transformers at a 380 kV station in Emden [100].

2.9.6.2 *DolWin3*

DolWin3, which was commissioned in 2018, is a project that was initiated by TenneT which is a joint German-Dutch network operator. The grid connection system has a capacity of 900 MW, whereas the offshore wind farm has the capacity to produce 400 MW of power. This power is then transferred over a ±320 kV VSC-HVDC link from the North Sea to the German shore through a 162 km subsea cable as shown in Figure 2-31. The power is integrated to the German onshore ac network at a DC/AC converter station in Dorpen/West lower Saxony [101].

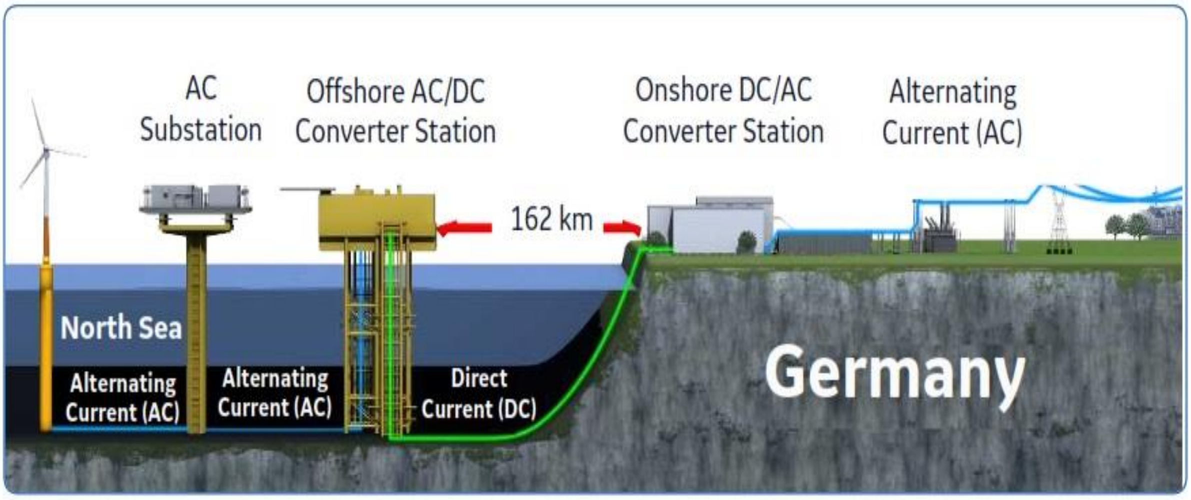

Figure 2-31: DolWin3 VSC-HVDC connection overview *[101]*

2.9.6.3 *Caprivi Link Interconnector*

The Caprivi Link Interconnector (CLI) is a 950 km ±350 kV VSC-HVDC connection between the 330 kV Zambezi Substation and 400 kV Gerus Substation in Namibia as shown in Figure 2-32 below. The VSC-HVDC link pioneers the use of overhead dc lines between two substations and has a capacity of 300 MW (monopole). The project was commissioned in the year 2010 to a value of N$ 3.2 billion. There are plans to expand the interconnector to a 600 MW bipole system that will link Namibia to Botswana and Zimbabwe. The presence of the CLI is crucial as it aids in improving the stability of the weak AC networks of the South African Power Pool (SAPP) as well as limits the possibility of a regional-wide black-out within the SAPP [102, 103].

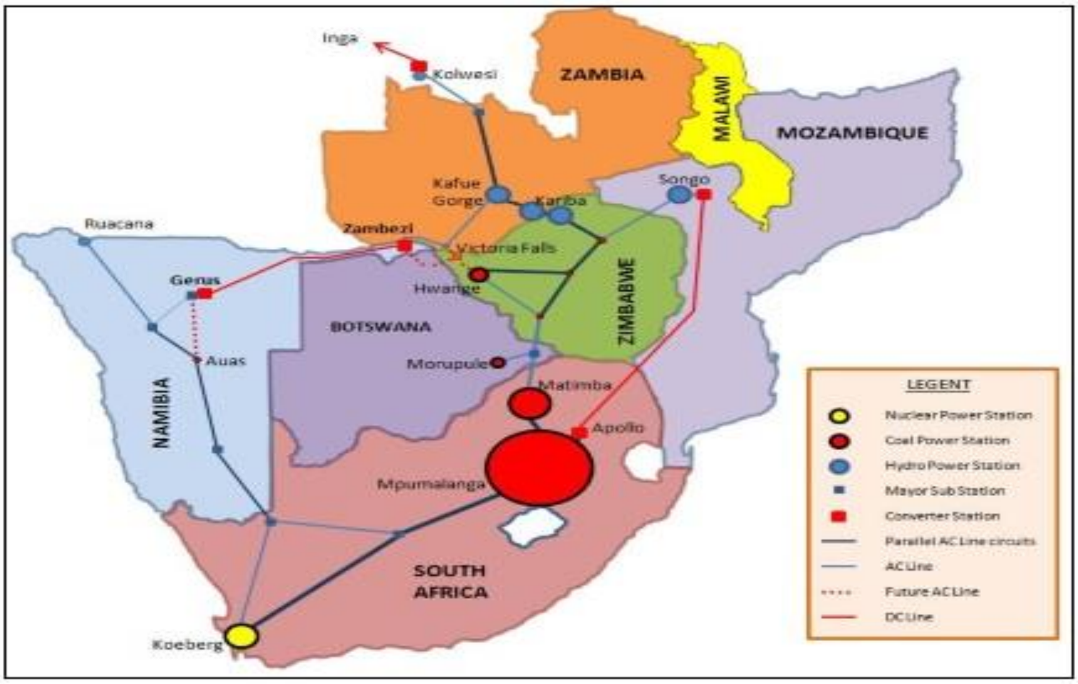

Figure 2-32: SAPP with the embedded Caprivi Link Interconnector *[103]*

Conclusion

The chapter highlights the installation of wind energy conversion systems and also focuses on the parameters that are considered in the establishment of offshore wind farms. The chapter then goes onto explore the modelling of DFIGs as they are widely used in the offshore wind farm installations. Moreover, the chapter then goes on to expatiate on power system stability with the focus being on rotor angle stability and small-signal stability. Power delivery systems with the main emphasis being VSC-HVDC systems, their configurations and control are then analysed. The chapter finally concludes by focusing on large scale VSC-HVDC systems that have been commissioned.

CHAPTER 3: SYSTEM MODELLING

The models of the offshore wind farms and the VSC-HVDC links are developed in DIgSILENT Power Factory. The wind turbines are aggregated into a number of DFIG models with the number of aggregated models depending on the rating of the turbines and the total required generation capacity of the wind farms. The wind data is collected through Global Wind Atlas. The data collected from this software package is adequate for the study as the same data is also used for actual feasibility studies in real-life project development [104, 105].

3.1 Wind Farm Modelling

Global Wind Atlas (GWA) is a free-to-use web-based tool developed as a result of collaboration between the Technical University of Denmark (DTU Wind Energy) and the World Bank Group. The web-based application assists various stakeholders in the wind energy sector in determining how feasible a site is for wind energy production. The application provides information on significant parameters to consider for a potential site such as [106]:

- Mean wind speed
- Mean power density
- Energy yield
- IEC class of installed turbine

The parameters are measured at heights of 10 m,50 m,100 m,150 m, and 200 m at every 250 m on the globe.

The latest version of GWA, GWA 3.0, was developed using close to 10 years of mesoscale time-series model simulations as shown in Figure 3-1. High-resolution calculations are achieved by implementing Frogfoot, which is the same calculation program used in WAsP.

The wind data obtained from GWA 3.0 is continually validated by comparing it to that of ESMAP-funded. The data has also been reanalysed over 10 years (2008-2017), with 32 sites from four countries used as an actual reference for the validation process. The mean absolute bias of the wind speed for the 32 sites is 14%. Further validation is carried out by comparing the results of models developed in GWA3 to the models developed in WAsP, a well-recognised software package used for wind resource assessment and wind turbine development [106, 107].

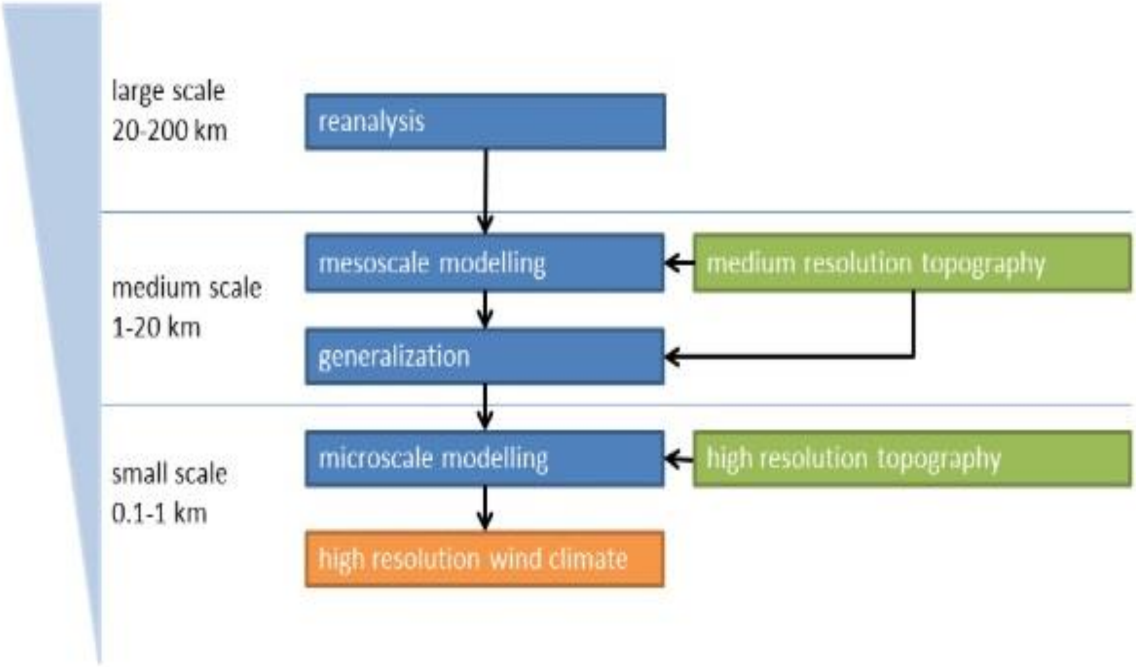

Figure 3-1: GWA modelling process *[107]*

3.1.1 Lüderitz Coast Wind Potential

The Namibian coastline experiences strong and high-speed winds at the coastal town of Lüderitz due to the permutations of the South Atlantic Anticyclone. The wind mostly blows form a southerly direction due to the intervention of the Coriolis force. The area of Lüderitz also features upwelling cells that have caused a lot of historically documented shipwrecks. The differences in pressure gradients between the coast and the land results in intense high-speed winds over the ocean floor in summer. These high-speed winds reach up to speeds of 22 metres/second and do not face any obstructions on the ocean floor and thus they could be harnessed in the development of offshore wind farms [108].

Global Wind Atlas was used in optimally selecting the site for the offshore wind farm. The wind farm is to be located at the following coordinates:

Latitude:	26°57'31.68"S
Longitude:	14°25'30.18"E

The average wind power density (P_D) of the chosen site is recorded to be more than 1300 W/m^2 at a height of 100 meters above sea level whereas the average wind speed is 11.11 m/s with a

50 % capacity factor as seen in Figure 3-2 to Figure 3-4. The site is therefore classified as a Class 7 site and is suitable for the establishment of an offshore wind farm [109].

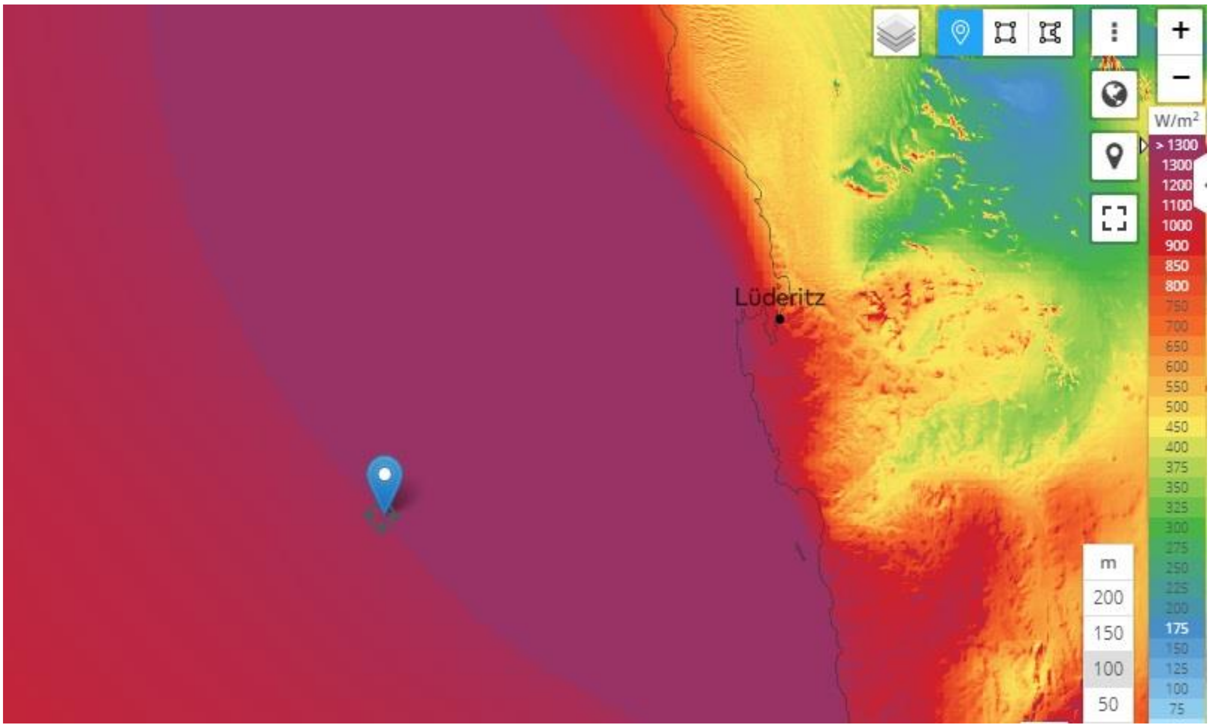

Figure 3-2: Offshore site wind power density measurement

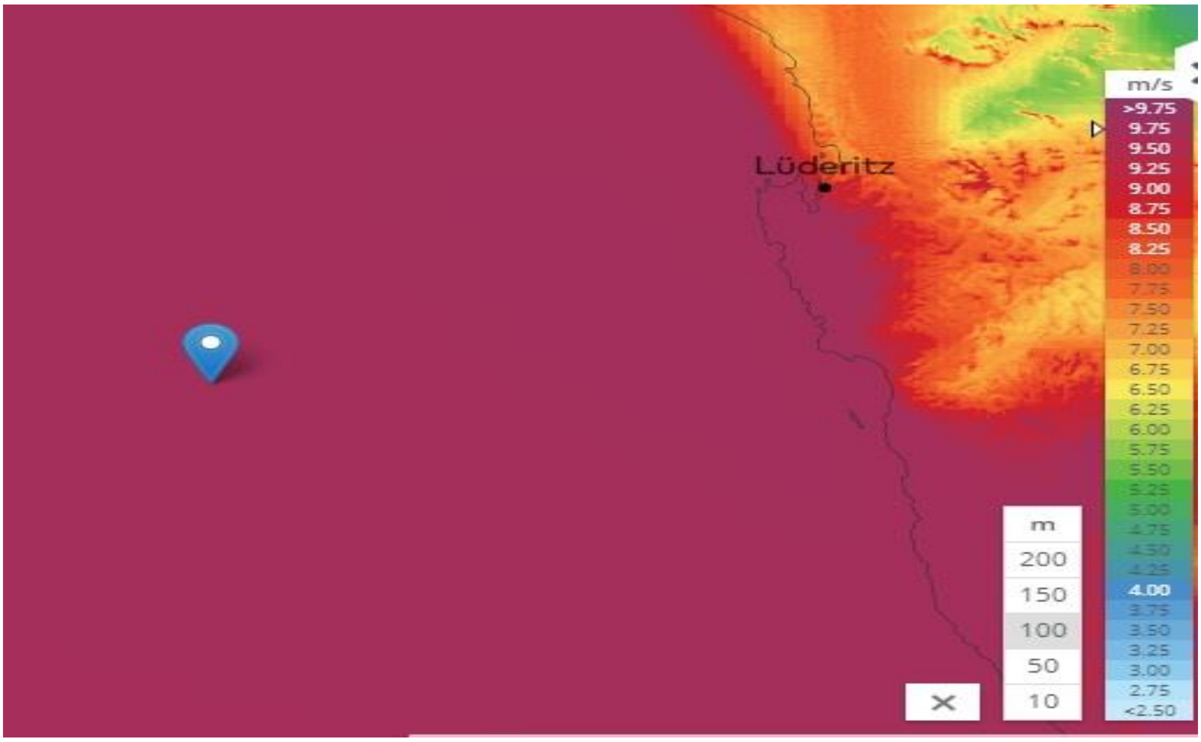

Figure 3-3: Offshore site wind speed measurement

Figure 3-4: Mean wind speed at 100-meter height

Table 3-1: Site details

Site coordinates:	26°57'31.68"S, 14°25'30.18"E
Distance of site from the shore:	100 km (DC cable)
Closest NamPower substation:	Kokerboom BB2 Substation (400 kV) Kokerboom BB1 Substation (220 kV)
Distance from shore to NamPower Substation:	30 km (AC overhead line)

3.1.2 DFIG Wind Farm Layout

Namibia’s peak energy demand in 2030 is forecasted to be 861 MW [76]. This means that an additional generation capacity of 350 MW will have to be added to the current generation infrastructure to meet this demand. Therefore, the offshore wind farm model used in this study has a maximum rating of 350 MW as shown in Figure 3-5, in line with Namibia’s high-probability demand for the next 10 years. The offshore wind farm is modelled using 5 MW Type 3B WT DIgSILENT in-built models developed according to the IEC 61400-27-1 standard as per the specifications in Table 3-2. The wind turbine models consist of a DFIG with a grid-connected stator and a rotor that is connected through a back-to-back electronic power converter. The DFIG models also contain additional equations for the frequency converter. The DIgSILENT models were validated by comparing them to MATLAB models and the numerical differences were only found to be 2% [110].

Table 3-2: 5MW DFIG specifications

Active Power (MW)	**Rated Voltage (kV)**	**Nominal Frequency (Hz)**	**No. of Pole Pairs**	**Stator Resistance (p.u.)**	**Stator Reactance (p.u.)**
5	0.69	50	2	0.01	0.1

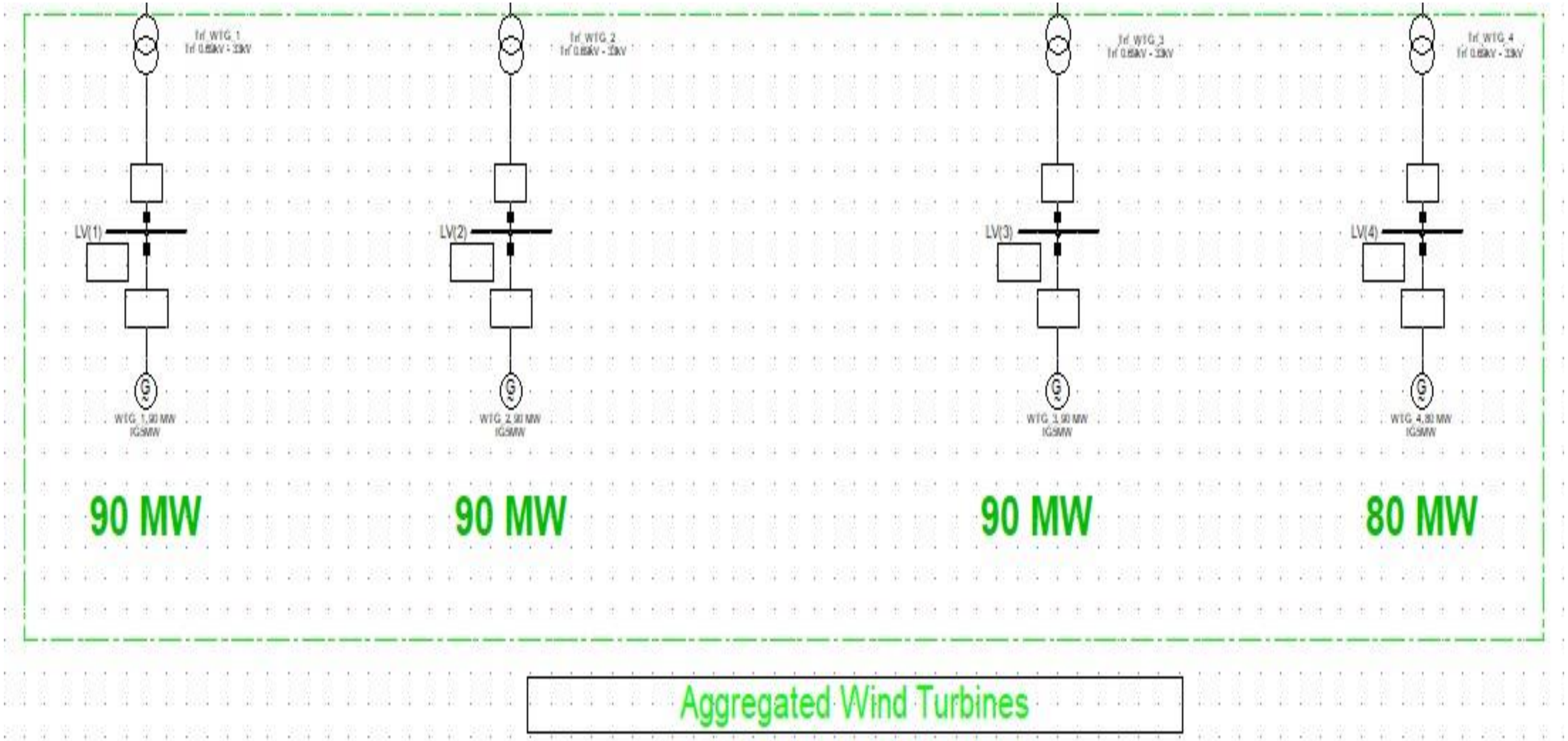

Figure 3-5: 350MW offshore wind farm

3.2 VSC-HVDC Modelling

DIgSILENT PowerFactory's two-level VSC-HVDC template is used as the base model for this study. Although simple, the two-level converter topology shown in Figure 3-6 can produce high quality three-phase VSC bridges. The operational limits of the converters are defined to be 95% to 105%.

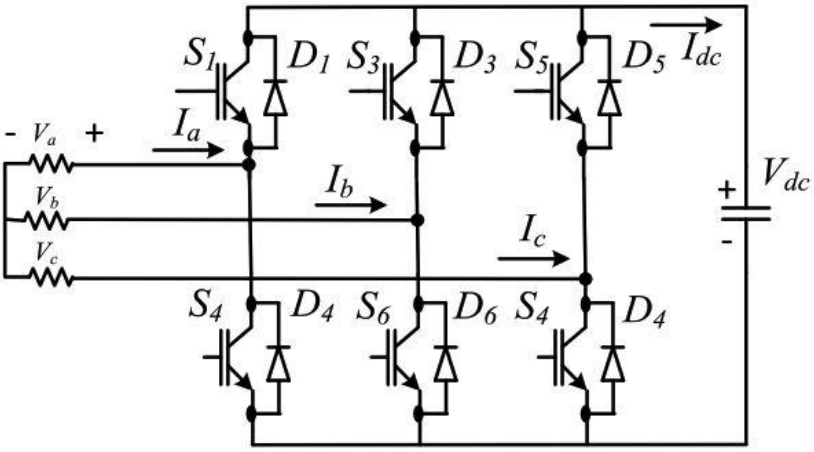

Figure 3-6: Two-level converter topology *[95]*

The switching sequence is carried out in a complementary manner as shown in Figure 3-7 below. Considering the mid-point in Figure 3-6, the output voltages of the converter are V_{ao}, V_{bo} and V_{co}. These voltages can only take two values; $\frac{+V_{dc}}{2}$ and $\frac{-V_{dc}}{2}$ [111, 112].

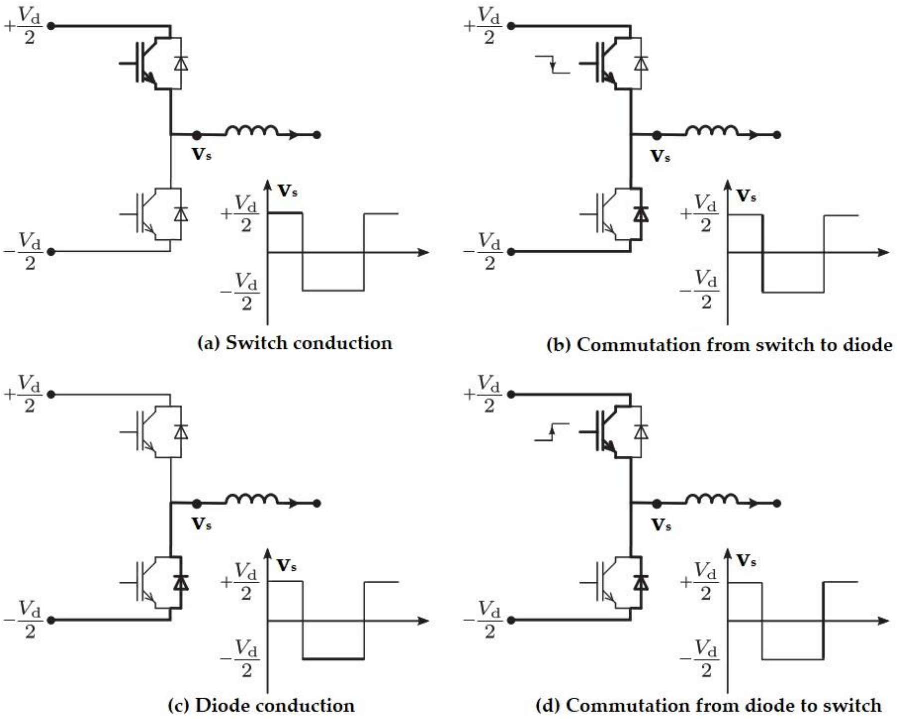

Figure 3-7: Two-level converter switching sequence *[112]*

3.2.1 Sinusoidal Pulse Width Modulation (SPWM)

Sinusoidal pulse width modulation (SPWM) is a technique that is used to regulate and generate the gating pulses that are required for the operation of voltage source converters. In SPWM, a triangular carrier signal is compared to a fundamental (50Hz) sinusoidal modulating signal as seen in Figure 3-8 below. A high pulse (1) is generated at instances where the modulating signal is greater than the carrier signal. A low pulse (0) is generated when the inverse occurs.

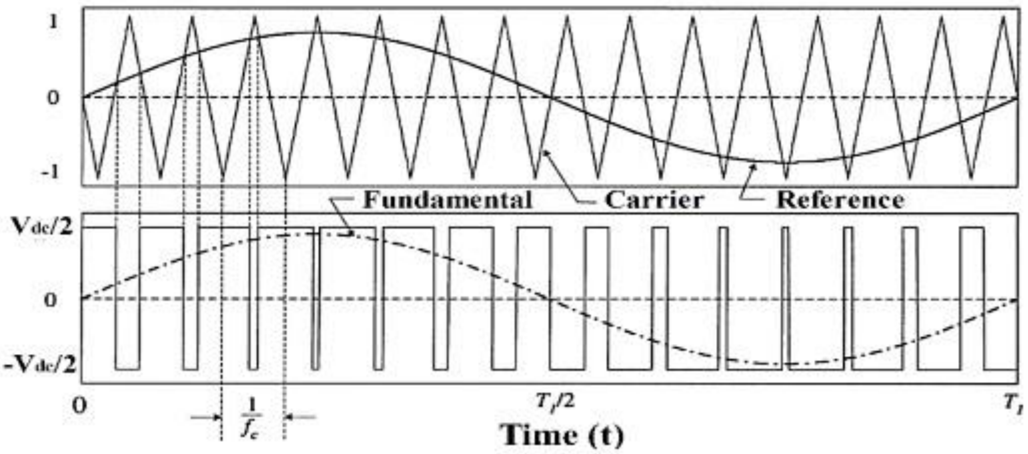

Figure 3-8: SPWM technique *[94]*

The amplitude modulation index (m_a) is given by:

$$m_a = \frac{V_m}{V_c} \tag{3-1}$$

Where V_m is the peak value of the modulating signal and V_c is the peak value of the carrier signal. The region defined by $0 < m_a < 1$ is referred to as the linear region of modulation since the output voltage of the inverter increases linearly with the modulation index (m_a) [94, 113].

3.2.2 VSC-HVDC Capability Chart

The capability chart shows the operating range of voltage source converters in the P-Q plane. The capability curve is limited by three main factors which are as follows [114]:

1. Maximum current through the IGBT valves: The maximum current defines the maximum MVA circle of the capability curve.

2. Maximum DC voltage level: This defines the maximum reactive power of the capability curve as it depends on both the AC as well as DC voltage.

3. Maximum DC power: This defines the maximum active power operating range of the curve.

3.2.3 DC Power Rating

The maximum direct Voltage (U_{dc}) that can be employed without saturating the converters in relation to the AC voltage is given by [25, 115]:

$$V_{LL} = \frac{\sqrt{3}\,U_{dc}M}{2\sqrt{2}} \tag{3-2}$$

$\therefore$

$$U_{dc} = \frac{V_{LL}}{0.612\,M} \tag{3-3}$$

Where V_{LL} represents the AC line-to-line voltage, U_{dc} is the DC link voltage and M is the steady state modulation index ;$0 \leq M \leq 1$. M is taken to be 0.85 for the design of most commercial applications [25, 115].

From Equation (3-3), the DC link voltage is given by:

The DC power is given by:

$$P_{dc} = U_{dc}\, I_{dc} \tag{3-4}$$

Where I_{dc} is the current of the IGBT valves.

The IGBT valves in the PowerFactory template are rated at 1500 A.

3.2.4 DC Line Rating

The rating of one monopole is designed for 200 MW.

Rearranging Equation (3-4) gives us the following equation:

$$U_{dc} = \frac{P_{dc}}{I_{dc}} \tag{3-5}$$

$\therefore$

$U_{dc} = \frac{200\ MW}{1500\ A} = 133.33\ kV$

The DC line rating is therefore taken as 150kV to allow for contingencies and for standardisation.

3.2.5 Converter Sizing

The IGBT valves of the VSC-HVDC template used in the study have a current rating of 1500A and a rated DC voltage of 300kV.

The power rating of the converter is calculated below using Equation (3-4).

$P_{dc} = 300\ kV\ x\ \ 1500\ A = 450\ MW$

The converters are therefore rated at 450 MW.

3.2.6 Power Transformer Sizing

The power converter transformers are used to step up or step down the system voltage to levels that are suitable for the efficient operation of the converters [25].

3.2.6.1 *Onshore Transformer*

The secondary voltage of the onshore converter transformer is 400 kV as this is the rating of Kokerboom BB2.

The primary rating of the transformer is determined from Equation (3-2).

$$V_{LL} = U_{dc}\ X\ 0.612\ X\ M \qquad (3\text{-}2)$$

Where M is taken as 1 and U_{dc} is the DC line voltage rating of 150 kV.

$\therefore$

$V_{LL} = 150kV\ X\ 0.612\ X\ 1 = 91.8kV$

The secondary voltage range is therefore standardised to 110kV. The onshore converter transformer is therefore a 110/400kV ,450MVA transformer.

3.2.6.2 *Offshore Transformer*

The busbar voltage at the DFIG turbine generator collector busbar is 33 kV and the onshore converter has a power rating of 400 MW. Taking into account the 150 kV DC line rating, the power converter transformer should therefore be a 33/155kV step up transformer.

The rating of the transformer is given by Equation (3-6) [25].

$$S = \frac{P}{cos\theta} \qquad (3\text{-}6)$$

Where P is the converter rating of 400 MW and the power factor is taken as 1.

$\therefore$

$S = \frac{400\ MW}{1} = 400\ MVA$

The VSC-HVDC template in PowerFactory uses two 250MVA,33/33/155kV three winding offshore converter transformers.

3.2.7 DC Capacitor Sizing

DC-link capacitors are used to maintain the DC voltage at a steady value. Such capacitors are designed in such a way that they minimize the effects of harmonic components on the DC side that are as a result of the operation of the IGBT converters valves. The equivalent capacitance is calculated by Equation (3-7) below.

$$C_{dc\_eq} = \frac{\tau S_N}{0.5U_{dcN}^2} \qquad (3\text{-}7)$$

Where τ ,the time constant, is the time needed to fully charge the capacitor from zero to the DC link voltage value U_{dcN}^2 (150 kV) and S_N is the active power rating of the converter (450 MVA). A small value of 5ms is chosen as the time constant in order to dampen any ripple effects to the DC voltage. Rearranging Equation (3-7) by making τ the subject of the formula results in Equation (3-8) [25, 114, 115].

$$\tau = \frac{0.5C_{dc}U_{dcN}^2}{S_N} \tag{3-8}$$

The individual capacitance is given by:

$$\frac{1}{C_{eq}} = \frac{1}{C_1} + \frac{1}{C_2} \tag{3-9}$$

3.2.8 Phase Reactor Sizing

Phase reactors are employed to control the active and reactive power flow to the ac system. In addition to this, the reactors also double as high-pass filters, thereby regulating the presence of high frequency harmonic components in the system. The design parameter of the reactors are usually between 0.1 pu to 0.2 pu. The phase reactor is given by Equation (3-10) below. The phase reactor is chosen to have a value 0.1pu, with the resistance taken as 1% of the inductance.

$$L = \frac{\Delta t\omega_e(V_{LL} - V_{LLmax})}{0.9\,X0.612U_{dc}} \tag{3-10}$$

Where:

Δt is the minimum reference current tracking time. This should be less than the time constant of the converter controller.

V_{LL} is the AC line-to-line voltage,V_{LLmax} is the maximum value of the converter fundamental phase voltage and U_{dc} is the DC voltage.

$\omega_e = 2\pi f$, is the electrical frequency with f being a frequency of 50 Hz [25, 114, 115].

3.2.8.1 *AC Phase Reactor*

The base impedance of the AC system is given by :

$$Z_{base} = \frac{\sqrt{3}\,V^2}{S} \tag{3-11}$$

Where V^2 is the secondary transformer voltage and S is the converter rating.

The inductance is given by $L = \frac{Z_{pu}Z_{base}}{\omega}$ (3-12)

3.2.8.2 *DC Phase Reactor*

The base impedance of the DC system is given by :

$$Z_{base} = \frac{\sqrt{3}\,V^2}{S}$$

Where V^2 is the secondary transformer voltage and S is the converter rating.

The inductance is given by $L = \frac{Z_{pu}Z_{base}}{\omega}$

3.2.9 HVDC Control

The DIgSILENT PowerFactory VSC-HVDC template shown in Figure 3-9 employs two composite models; with one controlling the onshore VSC and the other controlling the offshore VSC.

3.2.9.1 *Onshore Controller*

The onshore controller is mainly responsible for maintaining the dc-link voltage at a set nominal value as shown in Table 3-3. The controller is made up of the following blocks [104, 116]:

- Main controller: controls the voltage via a P-I controller.
- Current controller: responsible for generation of the modulation index .
- Chopper controller: regulates the voltage that is fed to the onshore VSC and that's safeguarding the VSC from faults.

3.2.9.2 *Offshore Controller*

The offshore controller is mainly responsible for controlling the active and reactive power that is generated by the wind farms. The controller is made up of a number of measuring blocks and PI controllers with the final output signals being used to switch the IGBT modules on/off after being cross-referenced via SPWM [104, 116].

Table 3-3: VSC-HVDC link parameters *[104]*

Converters			
VSC-Rectifier		**VSC-Inverter**	
Rated AC voltage	155 kV	Rated AC voltage	110 kV
Rated DC voltage per pole	300 kV	Rated DC voltage per pole	300 kV
Rated power	450 MVA	Rated power	450 MVA
Control mode	P-Q	Control mode	DC voltage
Active Power set point per pole	400 MW	Voltage set point	0.974 p.u.
Modulation	Sinusoidal PWM	Modulation	Sinusoidal PWM
DC Line			
Rated voltage	150 kV		
Rated current	1.4 kA		
Length	100 km		
Conductor type	Aluminium		
AC resistance -R'(20°C)	0.01 Ω/km		
Reactance – X'	0.4 Ω/km		

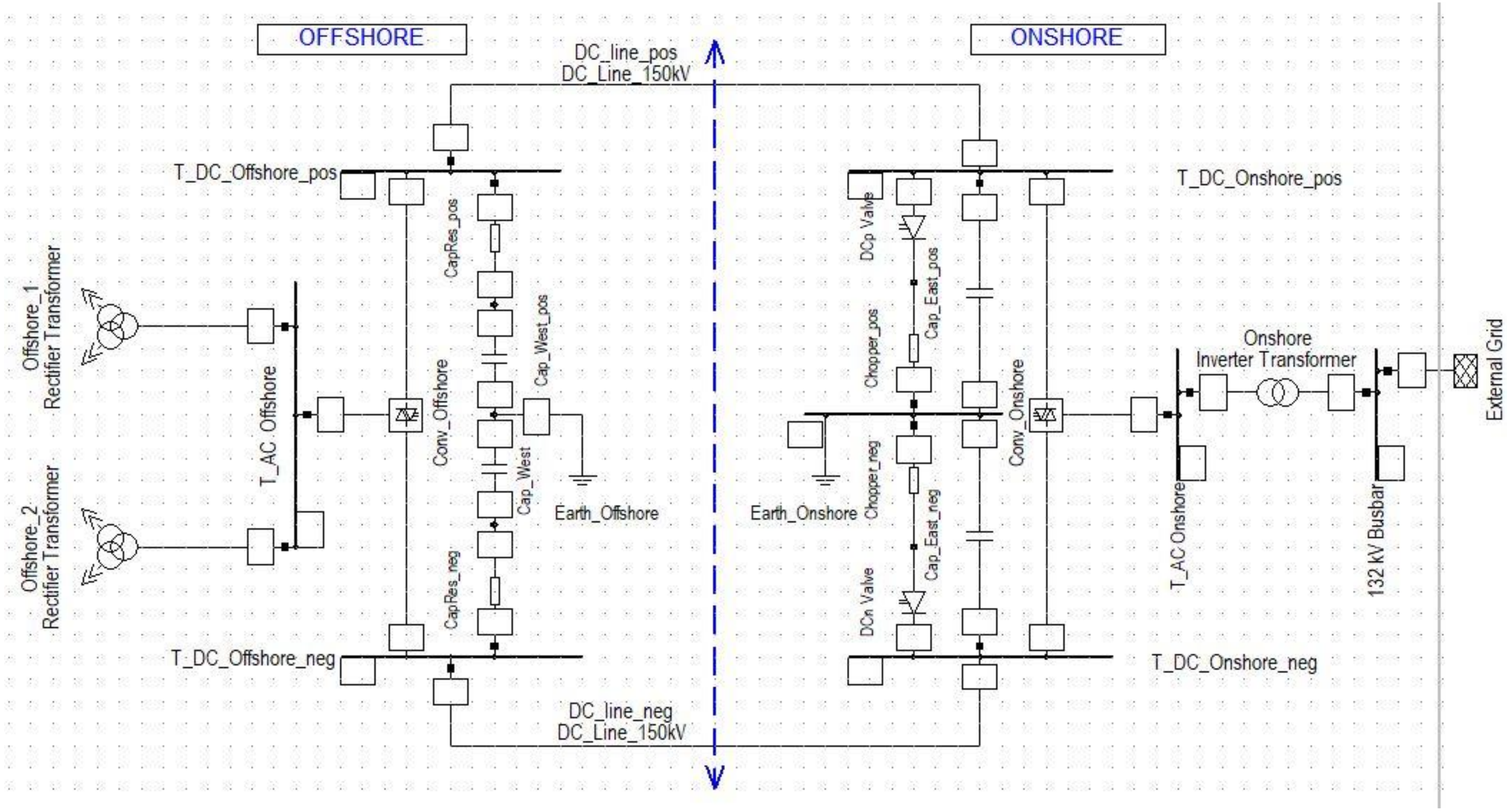

Figure 3-9: VSC-HVDC model *[104]*

3.3 NamPower Reduced Network Model

The NamPower network model used in the study was reduced to 32 load centres with all the generation stations and main transmission lines being included as shown in Appendix A. The distributed generation facilities are lumped up and integrated at the nearest load centre. All NamPower's customers such as towns and mines are modelled as general loads. The imported power from ESKOM and ZESCO are modelled as external grid sources with 330 MW and 50 MW ratings, respectively [117]. The offshore wind farm is coupled to the network at the Kokerboom BB1 as the Namib Substation is modelled as part of this substation.

Conclusion

This chapter elaborated on the software employed in the selection of the site for the offshore wind farm as well as the rationale behind the sizing of the wind farm that is to be used in the study. The chapter further goes on to highlight the parametrization of DigSILENT PowerFactory's VSC-HVDC template as well as the topology of the NamPower reduced network model that is used in the study.

CHAPTER 4: SIMULATION AND RESULTS ANALYSIS

4.1 SMIB Test Network

A single machine infinite bus (SMIB) network is used as a test bed and base case to analyze the integration of a wind farm on the transient stability of a network. The test bed is also of significance as it highlights the behaviour of a network in response to a range of perturbations [118, 119]. The SMIB used in this study consists of a 50 MVA synchronous generator with a PQ busbar operating at a power factor of 0.98, a 90 MVA 11/330 kV transformer, and two 200 km copper overhead lines (OHL) with a current rating of 0. 187 kA. The system supplies two 25 MW,12 MVAR loads connected to an infinite bus, as shown in figure 4-1 below.

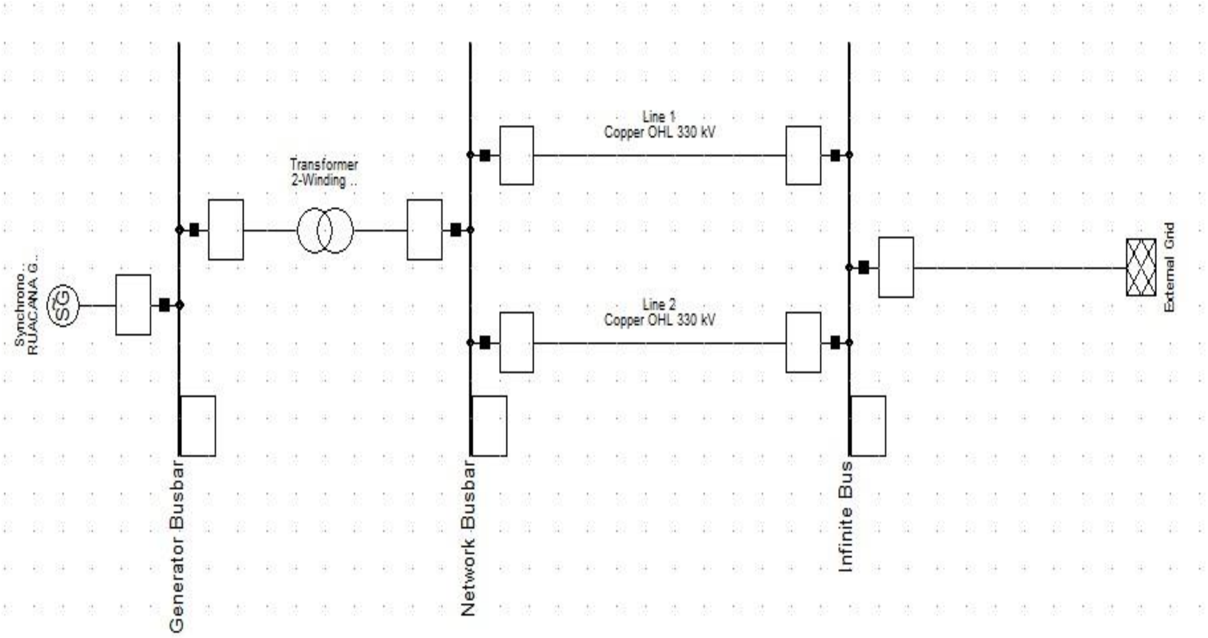

Figure 4-1: Single machine infinite bus

4.1.1 Load Flow Analysis

The load flow analysis of the base case indicates that the synchronous machine generates a maximum of 50 MW and 10.15 MVAR at the 11 kV busbar as shown in Figure 4-2. The external grid generates 1.4 MW in order to compensate for the grid losses that occur in the system. Thus, line 1 and Line 2 generate a total of 24.4 MVAR as compensation for the required reactive power.12 MVAR is consumed by each load, and the rest is absorbed by the external grid. The voltage at the busbars remains within the acceptable limit of 1.05 p.u. as seen in Table 4-1.

Table 4-1: Bus voltage

Element	Rated Voltage (kV)	Actual Voltage (kV)	Voltage (p.u)
Generator busbar	11	11.49	1.04
Network busbar	330	340.96	1.03
Infinite busbar	330	330.00	1.00

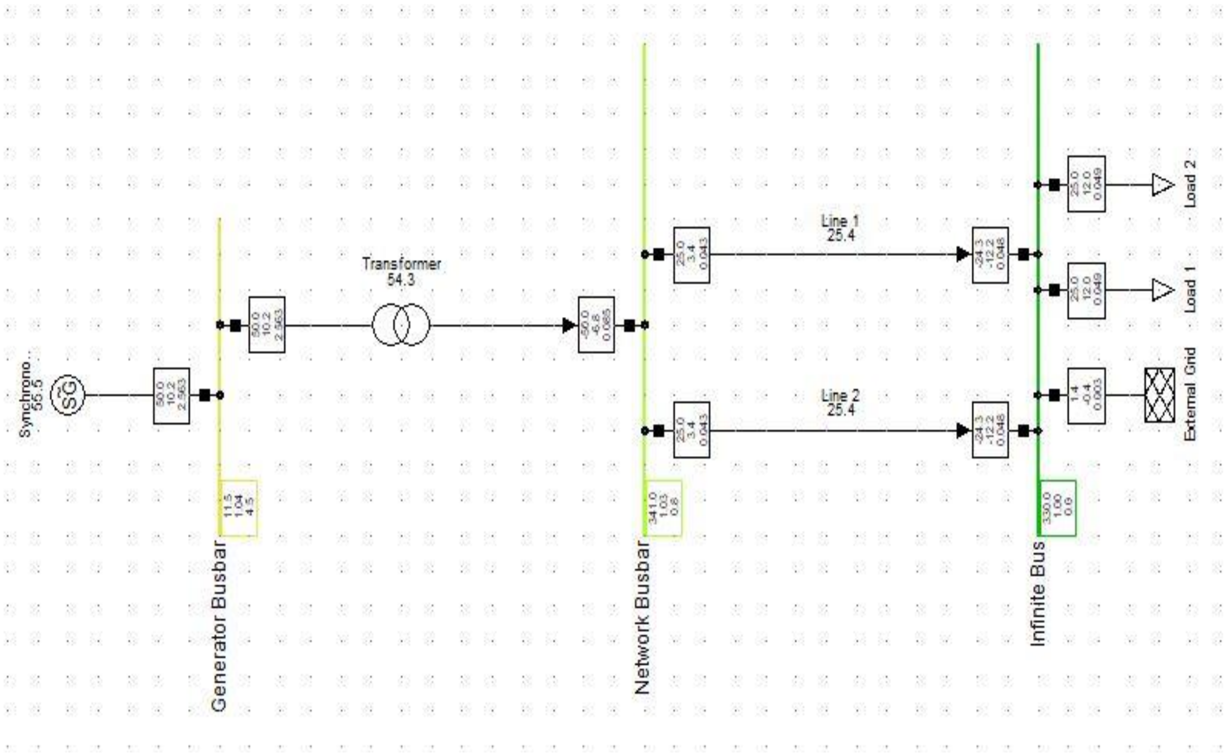

Figure 4-2: SMIB base case load flow analysis

4.1.2 Transient Stability Analysis

The transient stability analysis of the base case SMIB network was carried out in order to determine the rotor angle with reference to the machine in degrees and to determine the speed of the synchronous machine. The transient analysis was carried out for an absolute time of sixty seconds (60s) using the RMS/EMT Simulation tab in DIgSILENT PowerFactory.

The transient stability analysis was carried out by applying the steps highlighted in Figure 4-3:

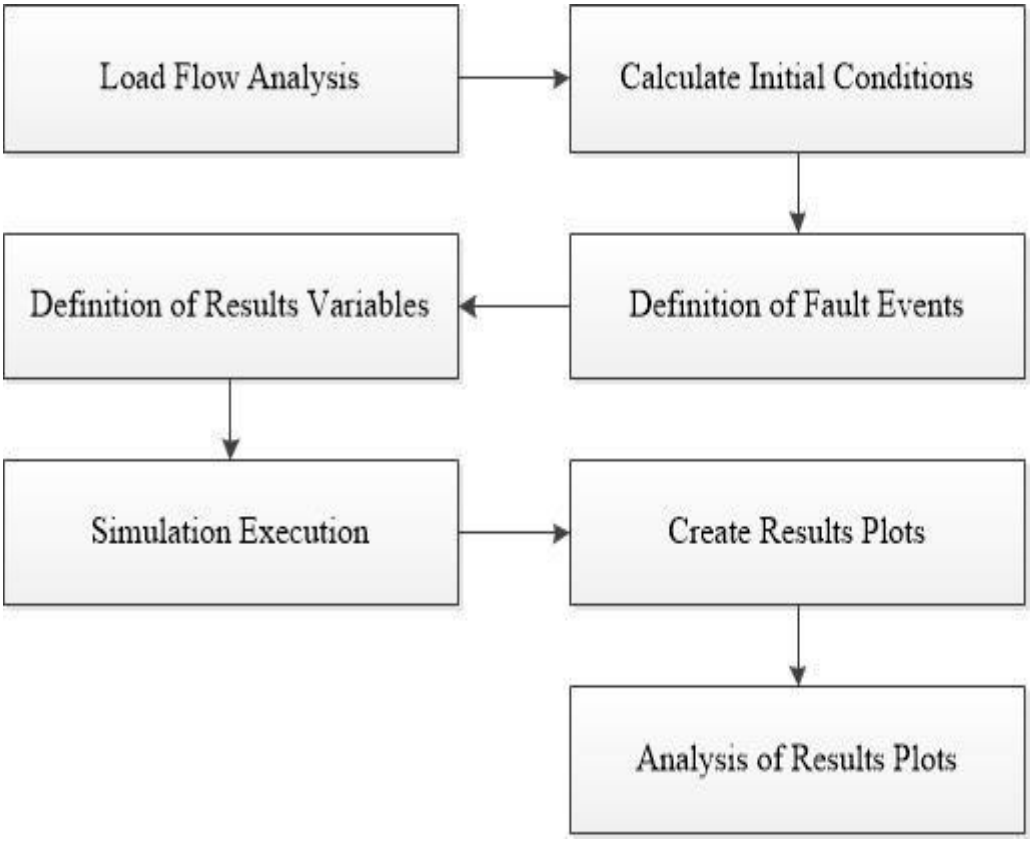

Figure 4-3: Transient analysis flow chart

The fault event is defined as a three-phase short-circuit fault on Line 1. The fault occurs at 5 seconds and is cleared by disconnecting the line after 80 ms, which is in line with NamPower's current protection settings. There is a swing experienced in the rotor angle from a steady-state value of 44.068° to a maximum peak value of 46. 987°. The rotor angle then undergoes oscillations which are eventually damped out after the fault is cleared and a new lower steady-state value is achieved as the impedance of the network decreases due to the disconnection of the line. The speed of the generator also increases on the introduction of the fault as the generator needs to produce more power at that instance due to the short circuit. After the fault is cleared, the speed decreases to the steady-state speed of 1 p.u. as seen in Figure 4-4. The ratings of the voltages at the different busbars also experience a dip and then rise back to the steady-state value as the fault is cleared. The same results are observed for a fault on Line 2 as the two lines have the same characteristics.

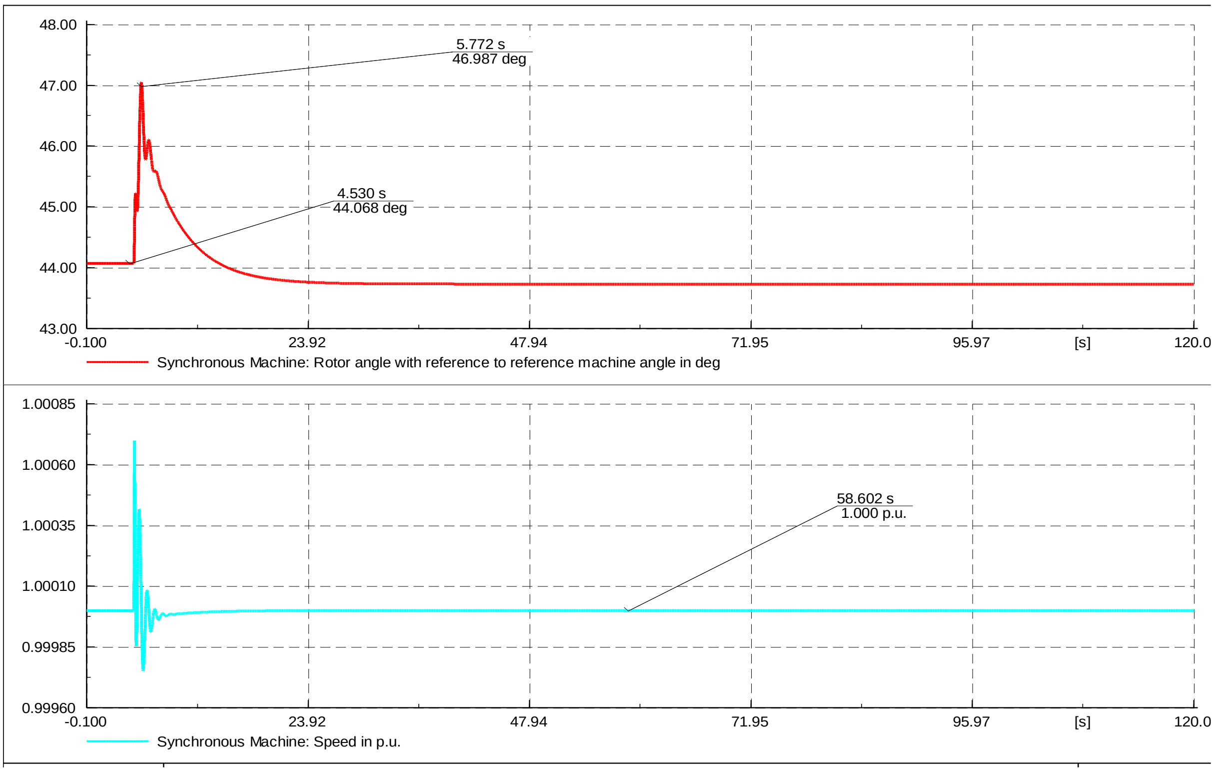

Figure 4-4: SMIB base case synchronous machine rotor angle and speed

4.1.2.1 *Critical Clearing Time*

The critical clearing time of the network was determined by running a Critical Fault Screening Script (CFSS) by executing the script on Line 1 [85]. The results of the CFSS indicate that the critical clearing time of the network is 1 second as shown in Figure 4-5. Therefore, if the contingency event is to last for longer than 1 second, the synchronous generator would experience pole slip and lose its transient stability as shown in Figure 4-6 below where a fault duration of 5 seconds was applied.

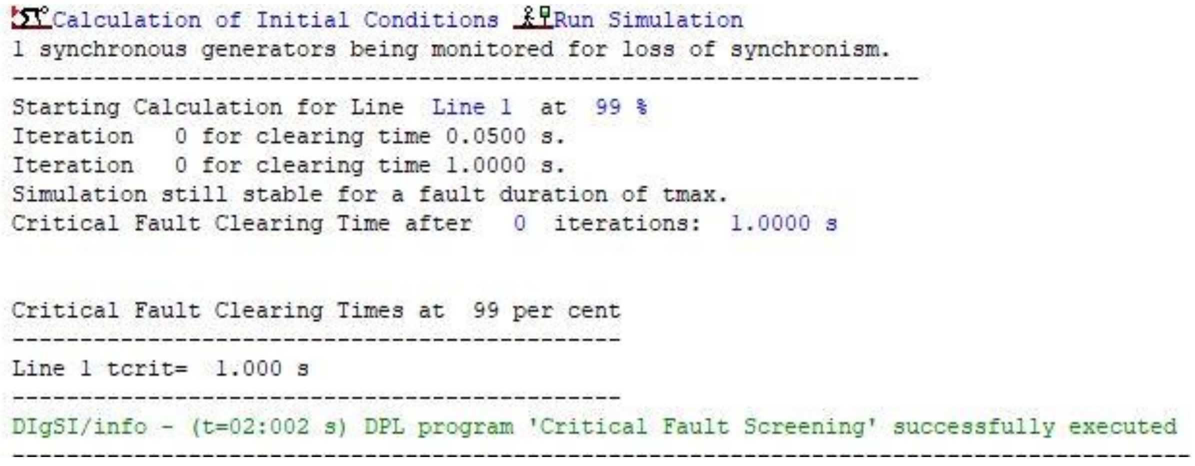

```
Calculation of Initial Conditions  Run Simulation
1 synchronous generators being monitored for loss of synchronism.
-------------------------------------------------------------------
Starting Calculation for Line  Line 1  at  99 %
Iteration    0 for clearing time 0.0500 s.
Iteration    0 for clearing time 1.0000 s.
Simulation still stable for a fault duration of tmax.
Critical Fault Clearing Time after   0  iterations:  1.0000 s


Critical Fault Clearing Times at  99 per cent
---------------------------------------------
Line 1 tcrit=  1.000 s
---------------------------------------------
DIgSI/info - (t=02:002 s) DPL program 'Critical Fault Screening' successfully executed
---------------------------------------------------------------------------------------
```

Figure 4-5: Critical Fault Screening Script (CFSS) of SMIB

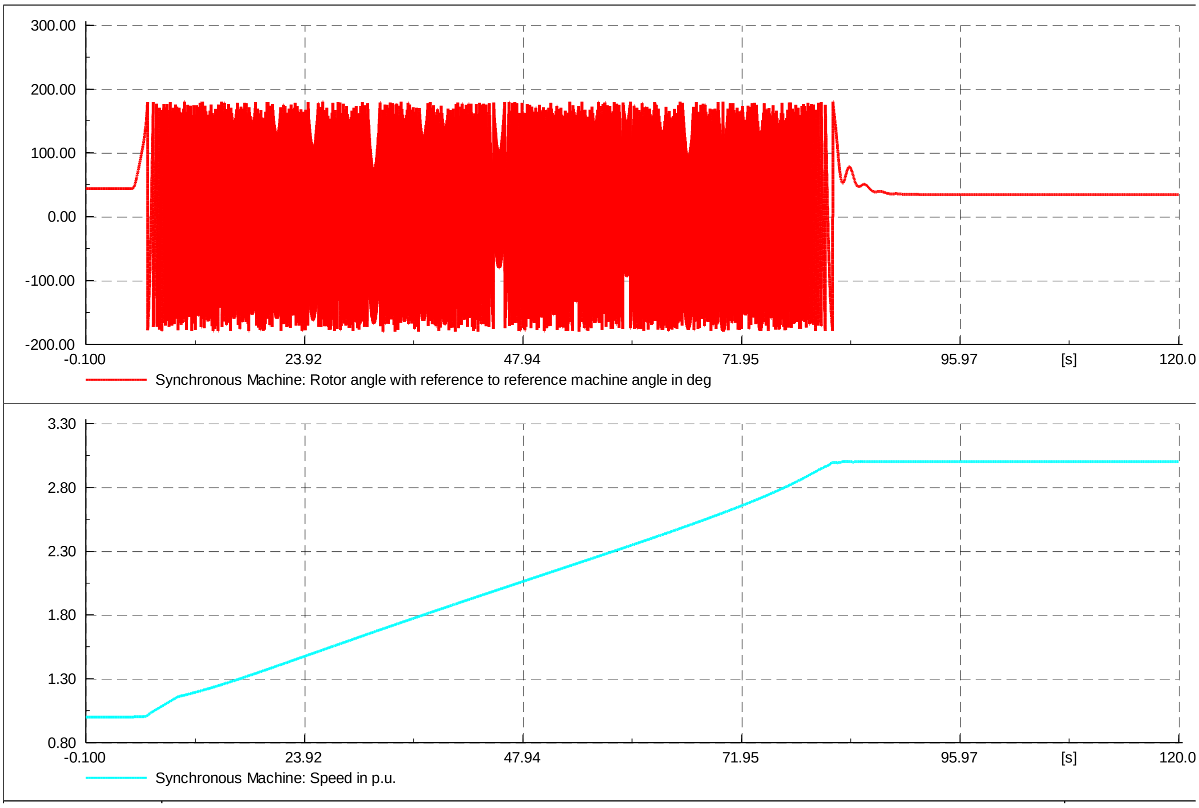

Figure 4-6: Rotor angle and speed for a fault duration of 5 seconds

4.1.3 Small Signal Stability Analysis

The small-signal stability analysis of the SMIB model base case was carried out using the Modal Analysis Simulation tab in DIgSILENT PowerFactory. Eigen value plots were then used to determine the pre-fault stability conditions of the network. Finally, the modal analysis was carried out by applying the steps in Figure 4-7 below:

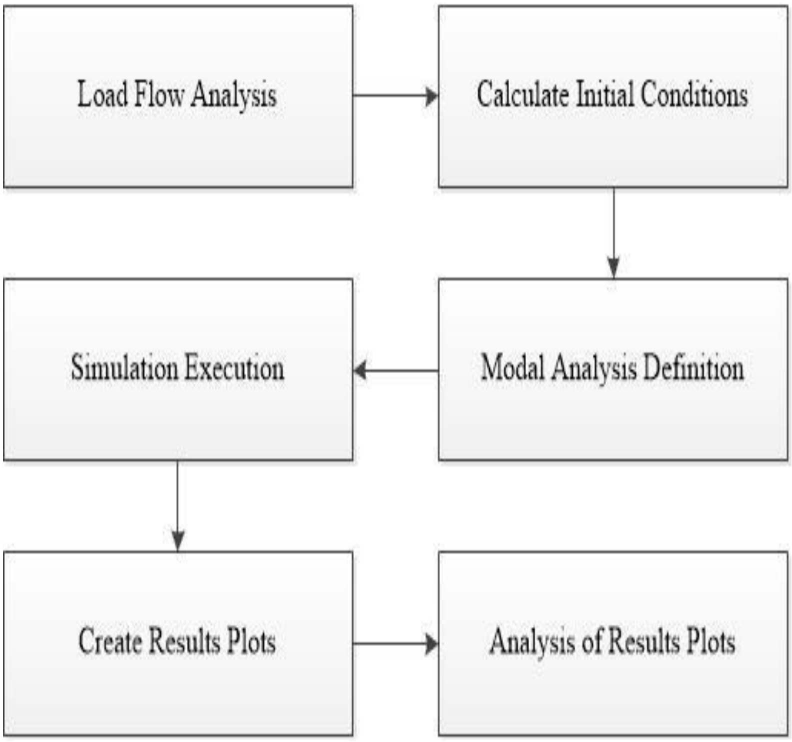

Figure 4-7: Modal analysis flow chart

As per Figure 4-8, the system is stable as all 12 modes have a negative real part and are located to the left of the imaginary plane [48, 120].The stability of modes 5,10,11, and 12 have to be closely monitored as they are close to the imaginary plane and are thus more likely to become unstable as the system is subjected to minor disturbances. Oscillatory modes that have a damping ratio of 1 are said to be critically damped and are more likely to achieve a state of equilibrium faster than under damped modes which have a damping ratio that is less than 1. The oscillatory modes,7 and 8, are poorly damped with a damping ratio of 0.229, as seen in Table 4-2 below. Modes 7and 8 have a frequency of 1.22 Hz and are local area oscillations as the single synchronous generator in the network is rotating against the rest of the network. Local area oscillations may affect the stability of the network by reducing the power transfer from the synchronous generator to the loads. Local modes can be sufficiently damped out by using power system stabilizers should the need arise [66]. The synchronous machine's speed contributes as a participation factor to mode 7 as per Figure 4-9 below.

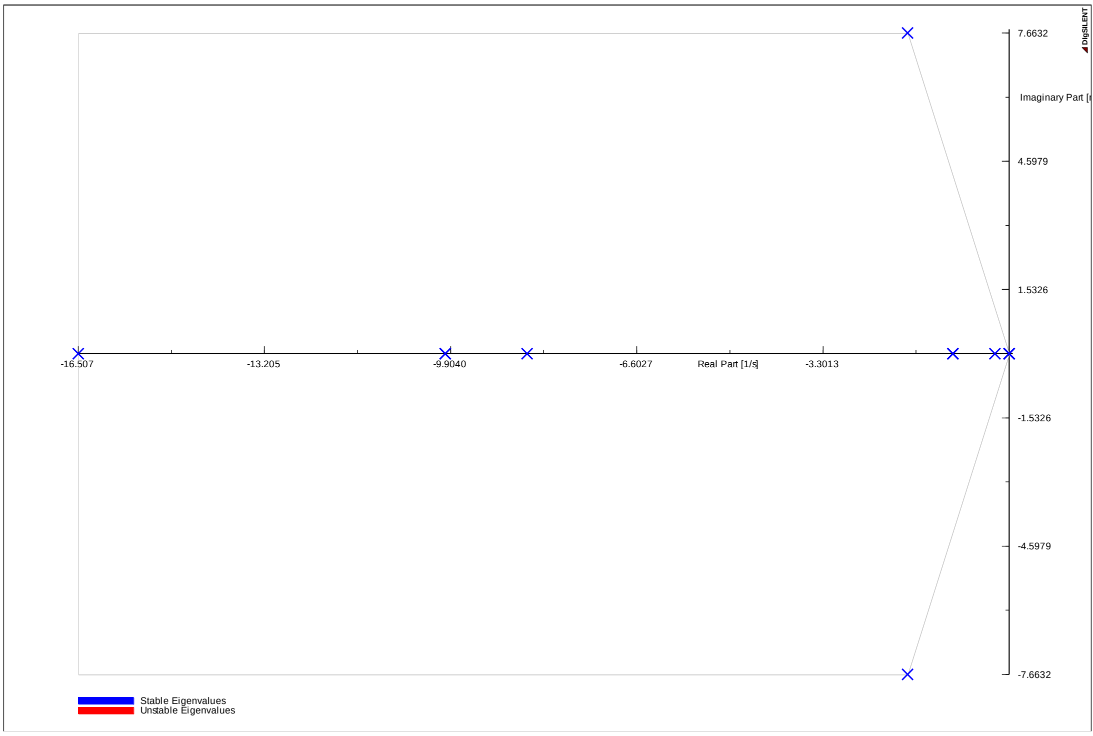

[1][2]

Figure 4-8: SMIB base case eigenvalue plot

Table 4-2: SMIB base case eigen values, frequencies and damping ratios

Mode	Real Part (1/s)	Imaginary Part (rad/s)	Damped Frequency (Hz)	Damping Ratio	Angle (Degrees)
1 & 3	-1.00	0	0	1	180
2 & 4	-10.00	0	0	1	180
5,11& 12	0	0	0	0	0,180,0
6	-16.507	0	0	1	180
7 & 8	-1.800	±7.633	1.22	0.229	±103.221
9	-8.55	0	0	1	180
10	-0.254	0	0	1	180

---

[1] The Blue crosses (x) of Figure 4-8 and all subsequent eigenvalue plots represent “Stable Eigenvalues” and the Red crosses (x) represent “Unstable Eigenvalues”

[2] The X- axis of Figure 4-8 and all subsequent eigenvalue plots is the “Real Part [1/s]” and the Y-Axis is the “Imaginary Part [rad/s]”

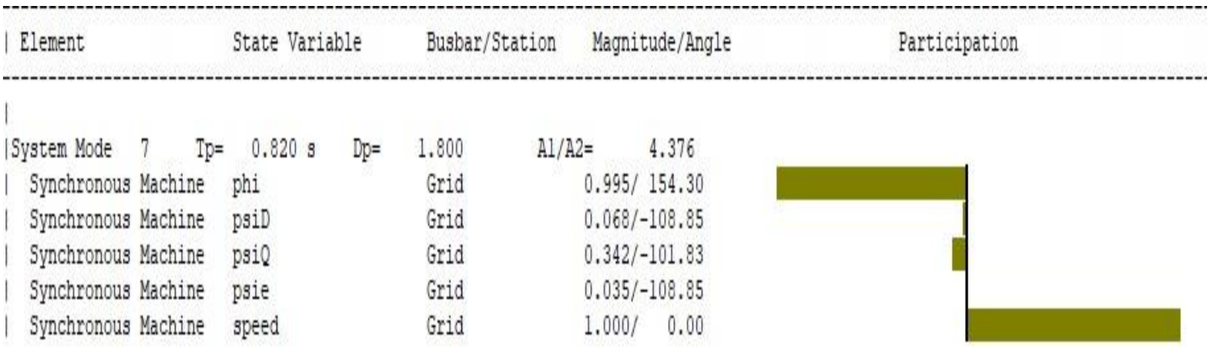

```
------------------------------------------------------------------------------------------------------------------------
| Element              State Variable      Busbar/Station    Magnitude/Angle                Participation
------------------------------------------------------------------------------------------------------------------------
|
|System Mode   7     Tp=   0.820 s     Dp=    1.800       A1/A2=      4.376
|  Synchronous Machine   phi                 Grid            0.995/ 154.30
|  Synchronous Machine   psiD                Grid            0.068/-108.85
|  Synchronous Machine   psiQ                Grid            0.342/-101.83
|  Synchronous Machine   psie                Grid            0.035/-108.85
|  Synchronous Machine   speed               Grid            1.000/   0.00
```

Figure 4-9: Base case participation factor

4.2 SMIB Test Network with DFIG Integration

The rotor angle stability and small-signal stability of the SMIB network are further analysed by adding a number of wind turbines to the system. The wind turbines are made up of doubly-fed induction generators that are rated at 5MW each, and the wind speed variation is not taken into account. The wind turbines are integrated into the network via an 11/330kV 250 MVA transformer as shown in Figure 4-10. The number of wind turbines is increased until the system is close to its small signal stability limit. A perturbation in the form of a short circuit on Line 1 is introduced into the system to better understand how the network will react. The short circuit is then disconnected after a duration of 80 ms, which is in line with NamPower's current protection settings. In order to better understand the small signal stability, the number of wind turbines is increased until the system is close to its small-signal stability limit. This is the point before any eigen values move over to the right half plane and begin to have a positive real part.

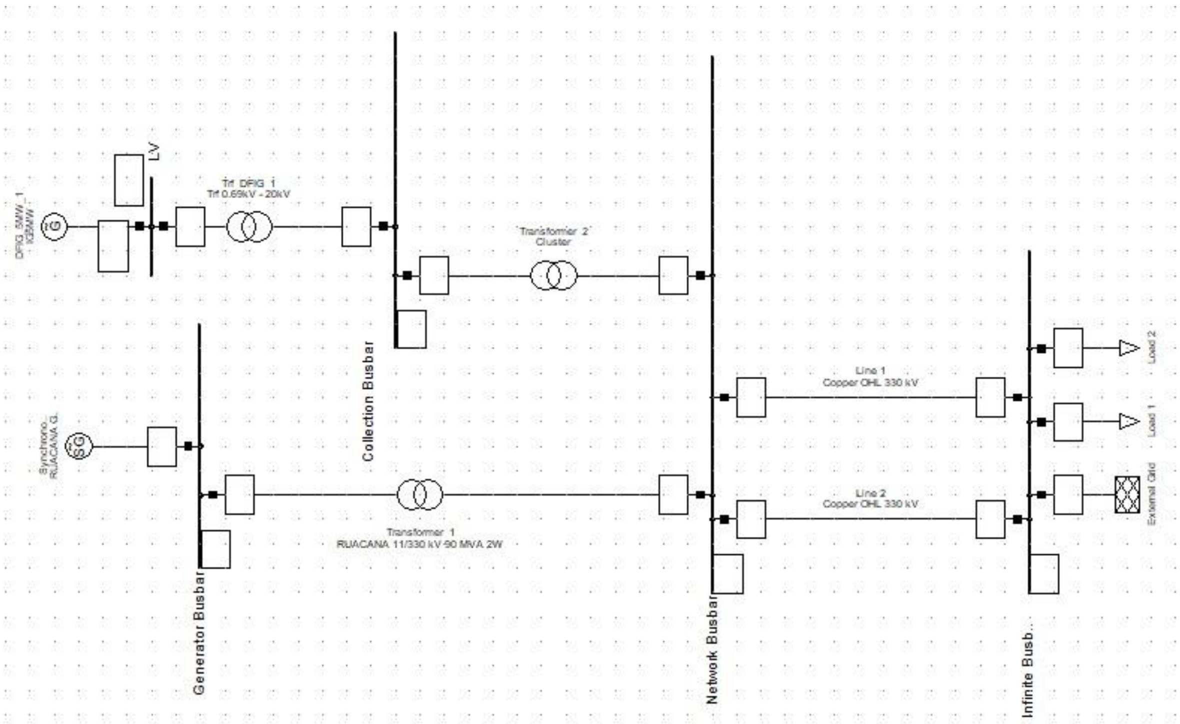

Figure 4-10: SMIB with 5MW DFIG wind turbine

4.2.1 Load Flow Analysis

The load flow analysis indicates that the power generated increases from 50 MW to 75 MW, whereas the reactive power generated by Line 1 and Line 2 decreases to 22 MVAR as the penetration level of the wind turbines is increased from 1 to 5. This is because the DFIGs also assist with reactive power compensation. The network also experiences power losses that equate to 3.91% of the power generated. The voltage at the synchronous generator busbar also increases from 1.04 p.u. in the absence of any DFIG to 1.05 p.u. for 1 DFIG and up to 1.06 p.u. for 5 DFIGs due to the increase in the reactive power of the system.

4.2.2 Transient Stability Analysis

A three-phase short circuit on Line 1 was defined as a fault event for rotor angle analysis of the synchronous generator in the network. The fault was cleared by disconnecting the line after 80 ms. As per Figure 4-11 below, the results indicate that the rotor angle swing only increases slightly as the number of DFIGs integrated into the network increases. The peak swing angle increases slightly from 47.040° for the base case to 47.987° for 5 DFIGs. The rotor angle swing decreases after the fault are cleared and then gradually oscillates to just below the steady state value as Line 1 is disconnected. The addition of DFIGs to the network does not greatly affect the rotor angle stability of the synchronous generator as it has a higher rating than the DFIGs, and thus it is able to anchor the network. The rotor speed also follows the same pattern as the rotor angle as it displays a drastic rise and then returns to its steady state value with time after the fault is cleared.

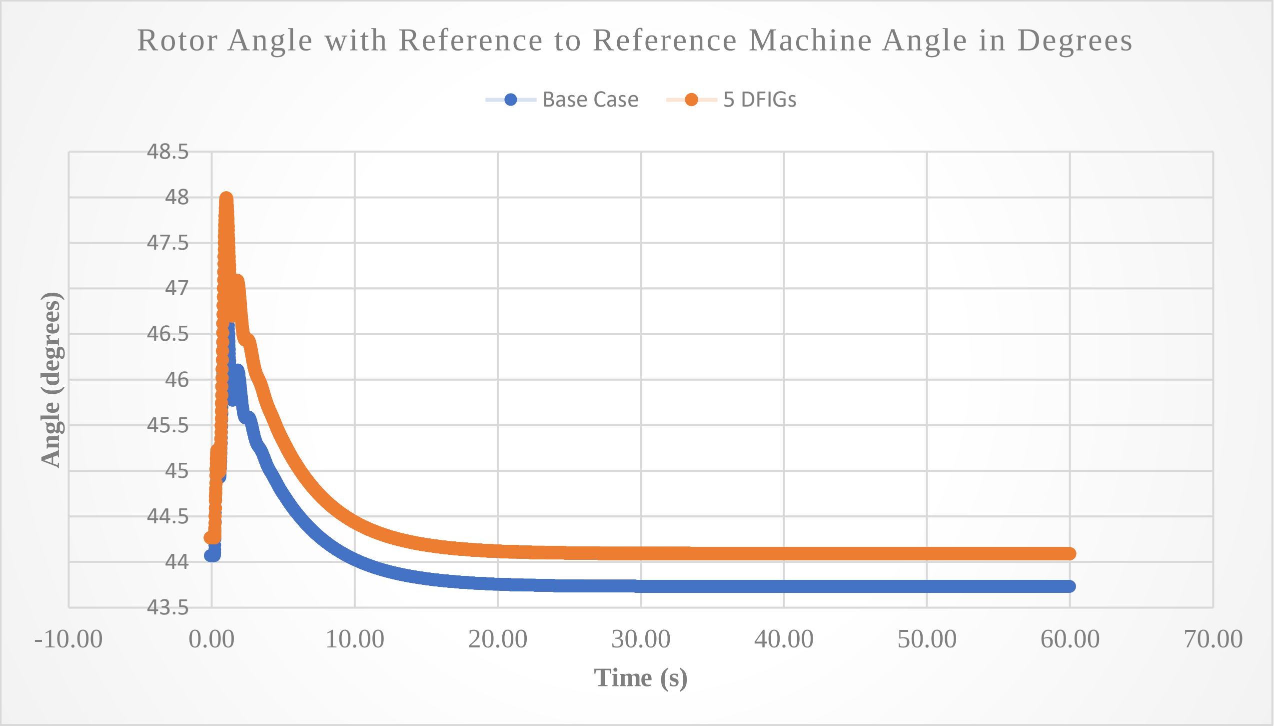

Figure 4-11: Rotor angle with reference to the reference machine angle in degrees

4.2.2.1 Critical Clearing Time

The Critical Fault Screening Script (CFSS) results indicate that the critical clearing time of the SMIB network with the integration of 5 DFIGs is 1 second as shown in Figure 4-12 below. Therefore, the faults within the network should be cleared within 1 second for the synchronous generator to maintain rotor angle stability.

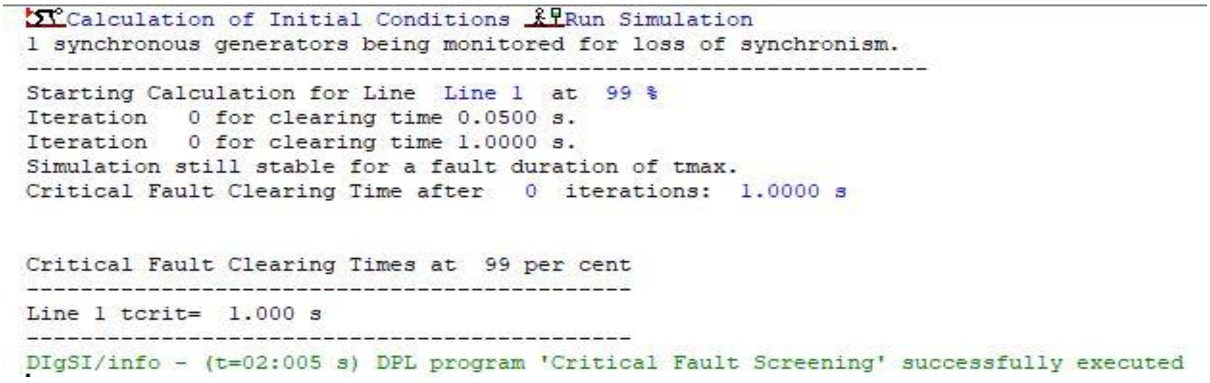

```
Calculation of Initial Conditions Run Simulation
1 synchronous generators being monitored for loss of synchronism.
-------------------------------------------------------------------
Starting Calculation for Line  Line 1  at  99 %
Iteration   0 for clearing time 0.0500 s.
Iteration   0 for clearing time 1.0000 s.
Simulation still stable for a fault duration of tmax.
Critical Fault Clearing Time after   0  iterations:  1.0000 s


Critical Fault Clearing Times at  99 per cent
---------------------------------------------
Line 1 tcrit=  1.000 s
---------------------------------------------
DIgSI/info - (t=02:005 s) DPL program 'Critical Fault Screening' successfully executed
```

Figure 4-12: Critical Fault Screening Script (CFSS) of SMIB with 5 DFIGs

4.2.3 Small-Signal Stability Analysis

The base case model has 12 modes, whereas the network with five DFIGs has 167 modes. The modal analysis of the system indicates that the small-signal stability is compromised as the number of DFIGs is increased from one DFIG to five DFIGs as more mode pairs are added. This is because the eigen values move closer and closer to the imaginary plane as the number of DFIGs increases. The positive (+) real parts of some of the modes also indicate that the system has lost its small-signal stability. The damping ratios of the modes also decrease with the introduction of more DFIGs into the system and thus weakening the overall system damping factor. Figure 4-13 to Figure 4-17 clearly shows the migration of the eigen values towards the unstable region as the number of DFIGs increased.

The DFIG control shaft becomes a major participation state variable as the number of DFIGs increases.

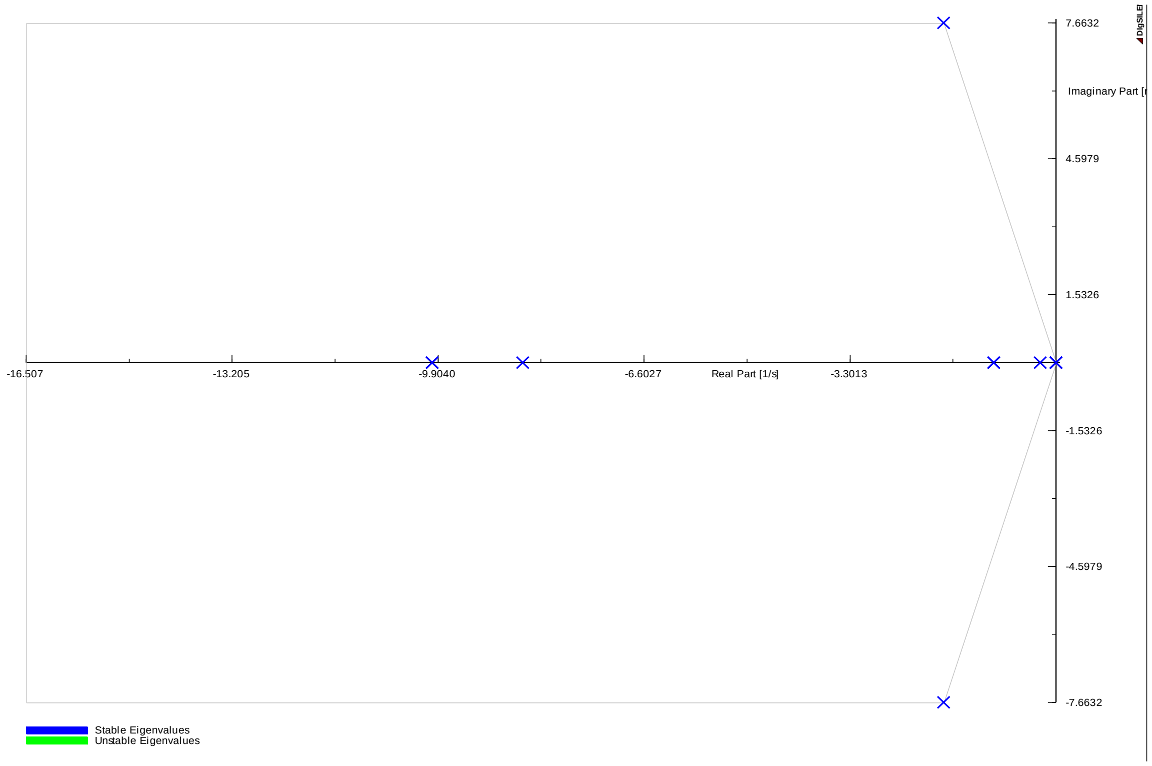

Figure 4-13: Base case eigenvalue plot

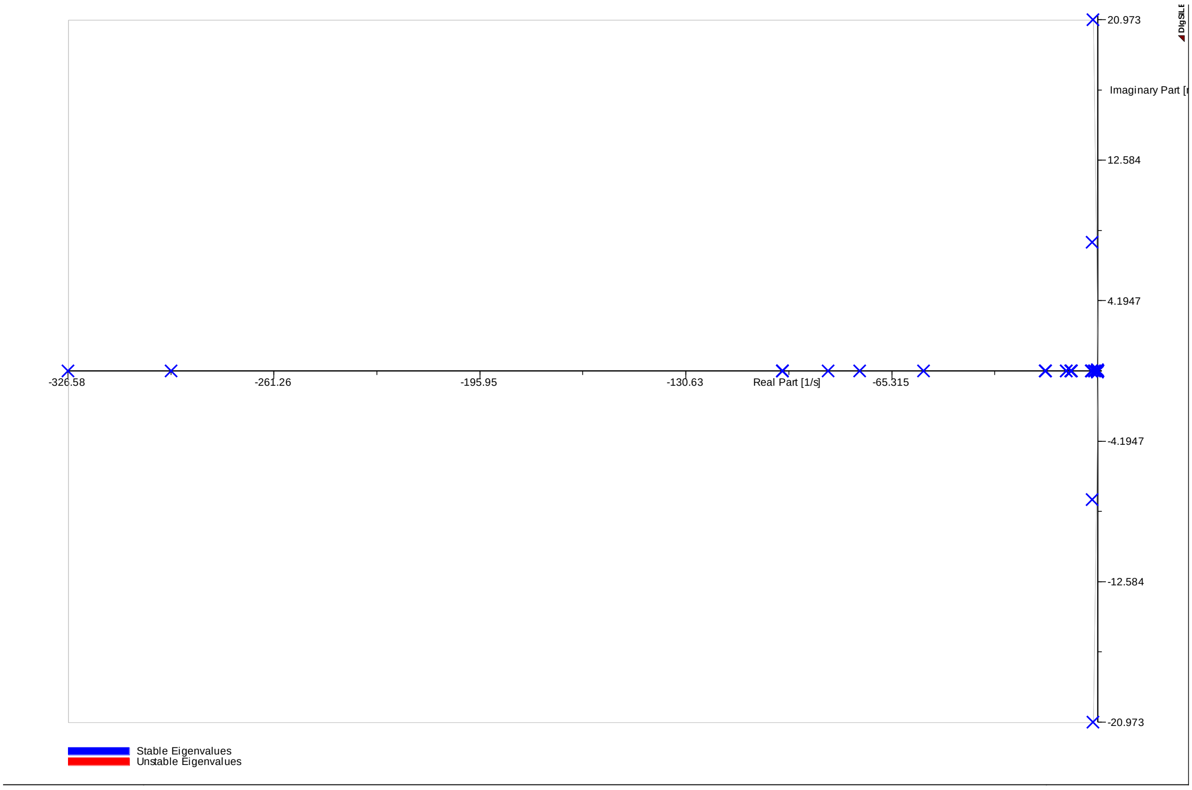

Figure 4-14: Eigenvalue plot of 1 DFIG

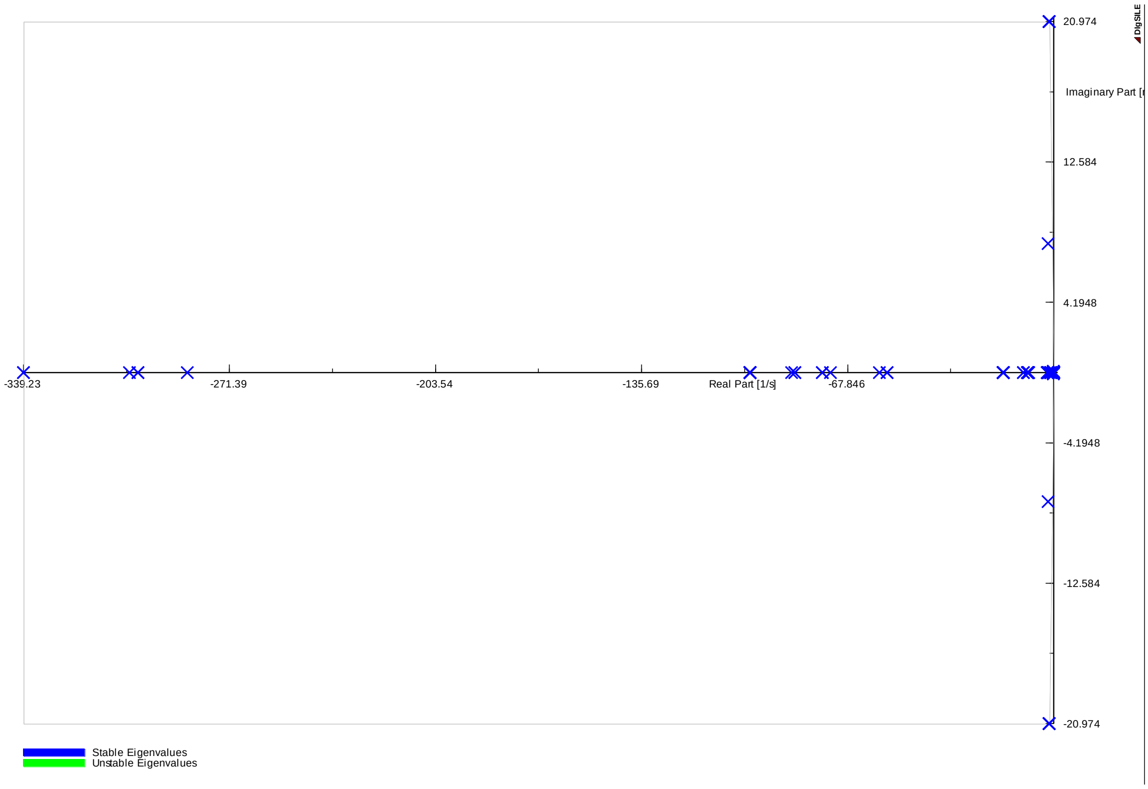

Figure 4-15:Eigenvalue plot of 3 DFIGs

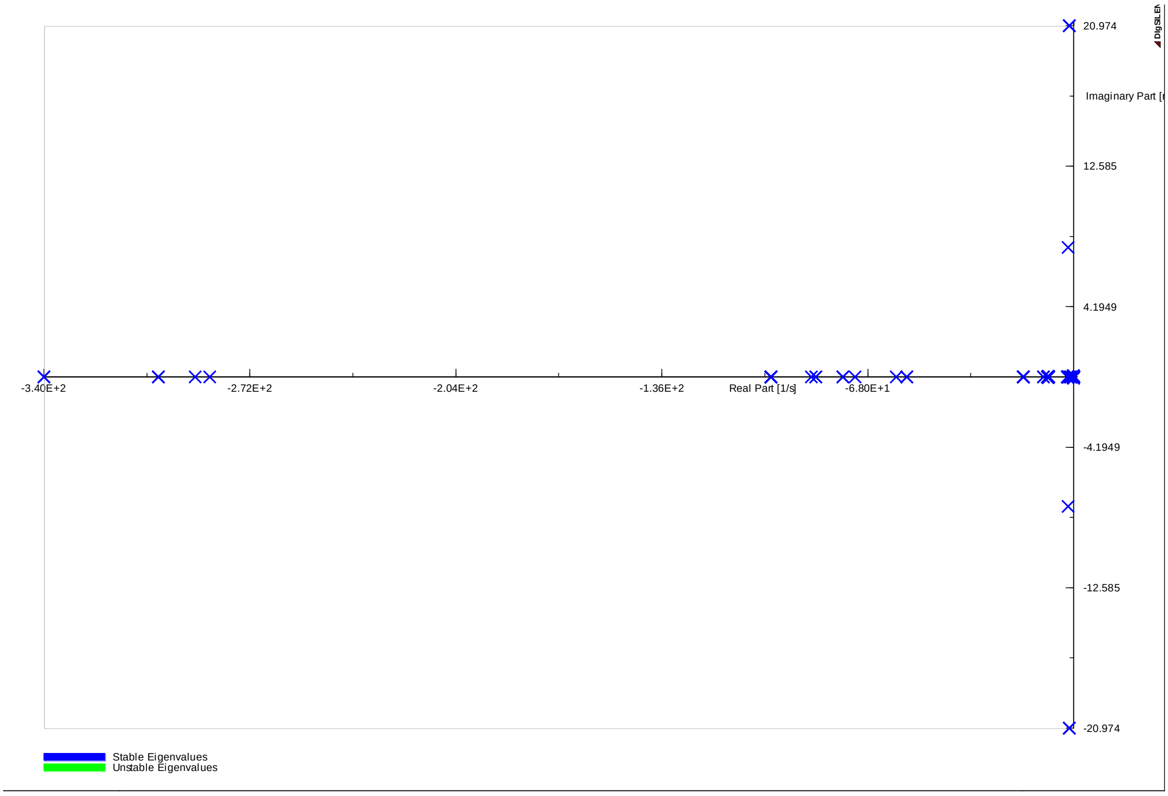

Figure 4-16:Eigenvalue plot of 4 DFIGs

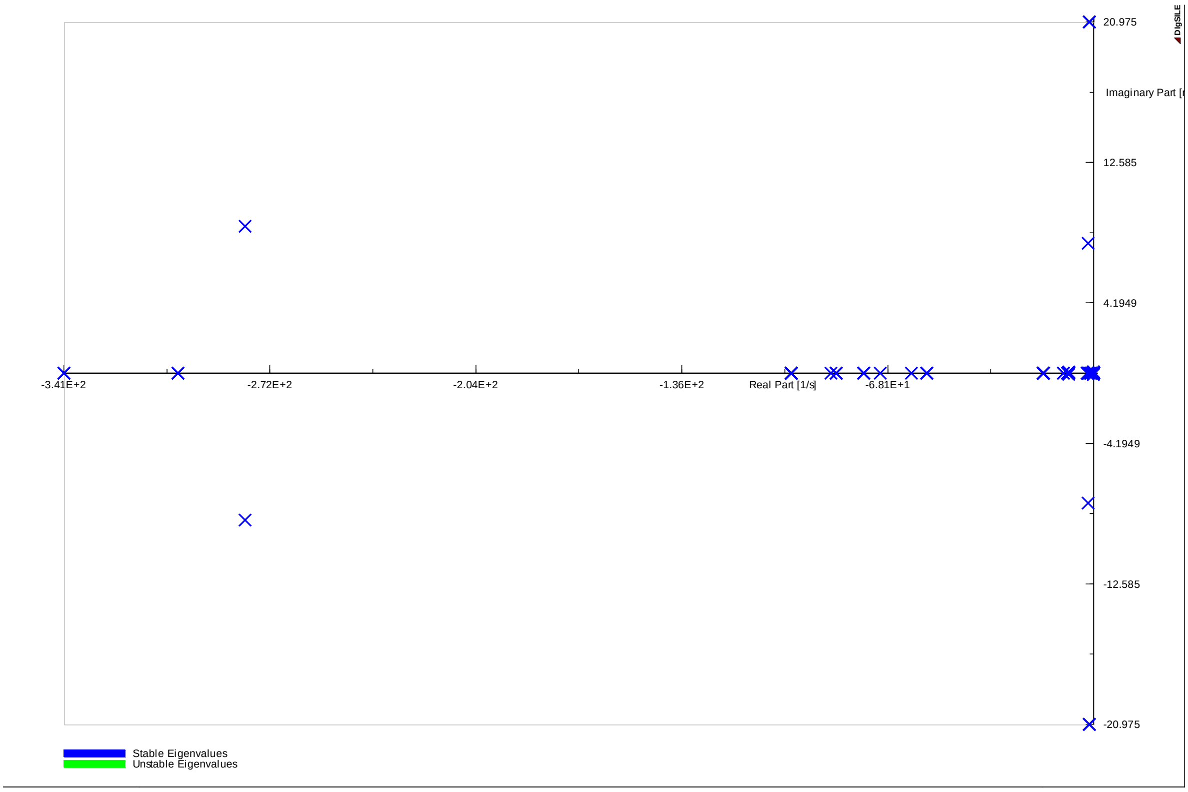

Figure 4-17: Eigenvalue plot of 5 DFIGs

4.2.4 Summary

The integration of DFIGs to the SMIB does not seem to greatly affect the rotor angle stability of the synchronous generator as the generator has a much higher rating (50 MVA) than the DFIGs (25 MVA). The rotor angle does experience swing as a fault is introduced, but the oscillations are damped out in a short time, with the rotor angle settling at a new equilibrium point as seen in Figure 4-11. The voltage at the different busbars also remains within the set limits except for the voltage at the generator busbar, which rises to 1.06 p.u. as the DFIGs and the external grid supply reactive power to the network when the contingency event occurs. The synchronous machine produces as much as 120 MVAr as the fault occurs. On the other hand, the small-signal stability is compromised with the addition of more DFIGs to the network as the damping requirements of the network increase. In addition to this, the eigen values migrate towards the imaginary plane, indicating decreased stability as explained in the revised literature. Moreover, the number of mode pairs that do not have a negative real part increases as the number of DFIGs is increased and thus further indicating that the small-signal stability is compromised.

4.3 NamPower Reduced Network Model

Load flow, transient stability, and modal analysis are carried out on the NamPower reduced network model to better understand the steady state and post-fault parameters of the network before the integration of the offshore wind farm via the VSC-HVDC link.

4.3.1 Load Flow Analysis

The network has an installed capacity of 574.79 MW but only generates a total of 179 MW that is supplemented by an external infeed of 343.43 MW, primarily from ESKOM and ZESCO. Therefore, the total power demand of the loads is 473.54 MW, whereas the system loses within the grid amount to approximately 8.98% of the generated power. The voltage at Kokerboom BB2, which is the point of integration for the offshore wind farm, has a rating of 1.03 p.u.

Table 4-3: Voltage at the busbars

Element	Rated Voltage (kV)	Actual Voltage (kV)	Voltage (p.u)
Kokerboom BB2	400	410.70	1.03
Auas BB2	400	407.60	1.02
Aries BB	400	400.00	1.00
Ruacana BB1	330	336.50	1.02

4.3.1.1 Fault Levels

The short-circuit levels of the network were calculated in DIgSILENT PowerFactory according to IEC60609. The short-circuit level is an important parameter in planning for the protection system of the network as well as in determining the short-circuit ratio upon integration of the wind farm. The short-circuit ratio (S_{CR}) is given by equation (4-1) [121].

$$S_{CR} = \frac{S_{CC}}{S_{wf}} \tag{4-1}$$

Where S_{CC} is the short-circuit level at the point of common coupling in MVA and S_{wf} rating of the wind farm in MW. The strength of the grid is defined by the short-circuit ratio as follows [94, 121]:

- If $S_{CR} > 3$, the AC system is considered to be strong
- If $2 \leq S_{CR} \leq 3$, the AC system is considered to be weak
- If $S_{CR} < 2$, the AC system is considered to be very weak

Table 4-4: Busbar fault levels

Busbar	Fault Level (MVA)	Peak Fault Current (kA)
Aries	10626	37.55
Auas BB2	2240	6.94
Harib	1929.1	14.62
Kokerboom BB1	2516.5	14.35
Kokerboom BB2	2796.3	8.64
Omburu BB2	2638.5	9.20
Ruacana BB1	1557.5	6.57

4.3.2 Transient Stability Analysis

The transient stability analysis of the reduced network model was carried out by introducing faults on the powerlines that make up NamPower's transmission network backbone. The short-circuit fault was cleared after 400 ms by disconnecting the line. The backbone powerlines ensure the reliability and the security of the supply of the network. The contingency events on the backbone were carried out as per the following scenarios:

Scenario 1: Three-phase short-circuit fault on the 400 kV Aries-Kokerboom line.

The rotor angle with reference to the machine angle of both the generators at Ruacana experiences a large rotor angle swing with the maximum peak value being 26.363° and the minimum peak value being 22.996° for Ruacana Generator 1. The rotor angle keeps on rising asymptotically as the fault is cleared, indicating that the generator has experienced slip and thus rotor angle stability has been compromised. The rotor angle of Van Eck Generator 1 swings to a minimum peak value of 40.583° and then continues to rise beyond the initial steady state value post-fault, as shown in Figures 4-18 below. The rotor angle stability of Van Eck Generator 1 is therefore compromised due to the contingency event. The voltage at Kokerboom BB2 and Aries BB drops below the set minimum value to 0.226 p.u. and 0.695 p.u. respectively as the fault occurs. The voltage at the Aries BB busbars then rises to within the acceptable range of 0.963 p.u. as the fault is cleared, whereas the voltage at Kokerboom BB2 is at 0.843 p.u, which is below the set value

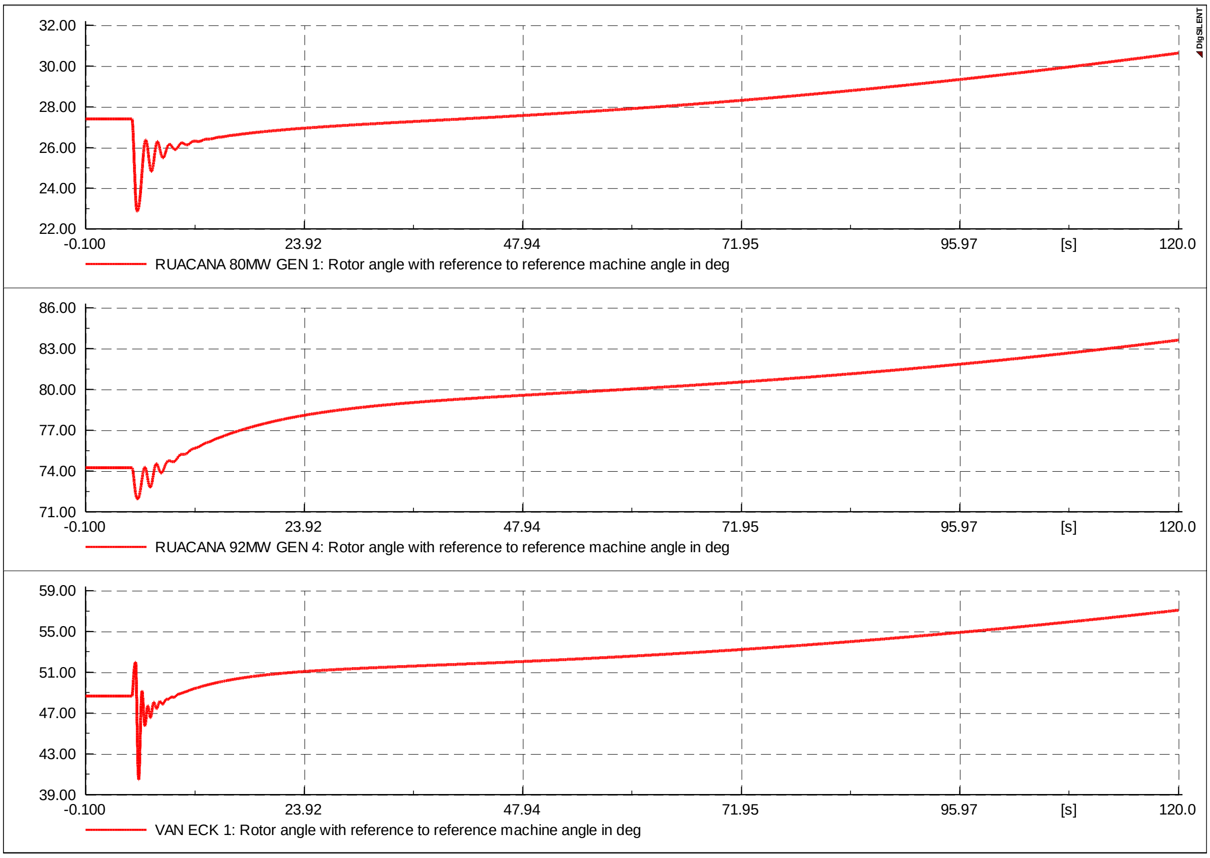

Figure 4-18: Scenario 1 rotor angle with reference to the reference machine angle

Scenario 2: Three-phase short-circuit fault on the 400 kV Auas-Kokerboom line.

The rotor angle with reference to the machine angle for all the generators at Ruacana experiences a small swing and undergoes minor, short-lived oscillations as a result of the fault being introduced as shown in Figure 4-19 below. However, the rotor angle continues to rise asymptotically above the initial steady-state value after the oscillations have been damped out and the fault is cleared. The generator at Van Eck experiences a larger swing than Ruacana and also follows the same pattern in terms of the rotor angle. The rotor angle continues to increase as the generators strive to compensate for the removed 400 kV transmission line. The voltage stability is also affected as the voltage at Kokerboom BB2, and AUAS BB2 drops below the fixed limit of 0.95 p.u. to 0.347 p.u. and 0.228 p.u. respectively as the fault occurs. This voltage at Kokerboom BB2 recovers to a value of 0.92 p.u. whereas the voltage at Auas BB2 recovers to a value of 0.809 p.u. which is still below the allowable limit. The drop in voltage below the allowable limit is experienced by all the busbars upstream of the Auas busbar, including Van Eck BB2, with a reading of 0.820 p.u. The collapse in the voltage plays a significant effect on the generators as they strive to carry out compensation, thus contributing to the rotor angle instability.

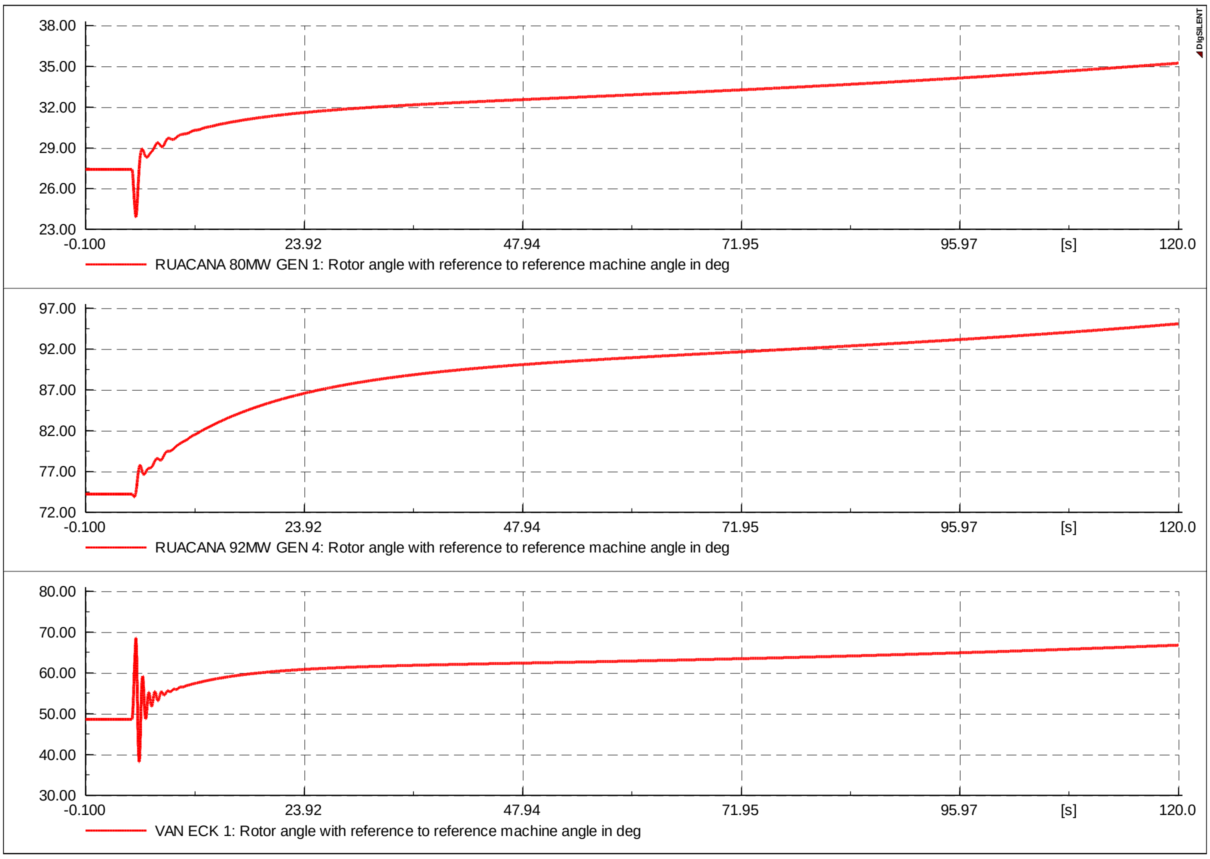

Figure 4-19: Scenario 2rotor angle with reference to the reference machine angle

Scenario 3: Three-phase short-circuit fault on the 200 kV Harib-Aggeneis Line 1.

The rotor angle for the generators at Ruacana experiences a reduced swing, with the maximum peak rotor angle being 36.363° for Generator 1 and the minimum peak rotor angle being 23.757°. Both the rotor angles of Generator 1 and 4 stabilise to a new equilibrium point after undergoing oscillations as the fault is cleared. The rotor angle of Van Eck Generator 1 experiences a much larger swing with a short settling time. All the generators still maintain their rotor angle stability as they stabilise to new equilibrium points once the fault is cleared and the oscillations have undergone damping as shown in Figure 4-20. The removal of the 200 kV line does not have a significant effect on the system as there is a backup line that still supplies the load. The voltage level at Aggeneis BB1 and Harib BB is not significantly affected by the fault as the voltage levels are still within the allowable limits after the fault is cleared at 1.022 p.u. and 0.972 p.u. respectively.

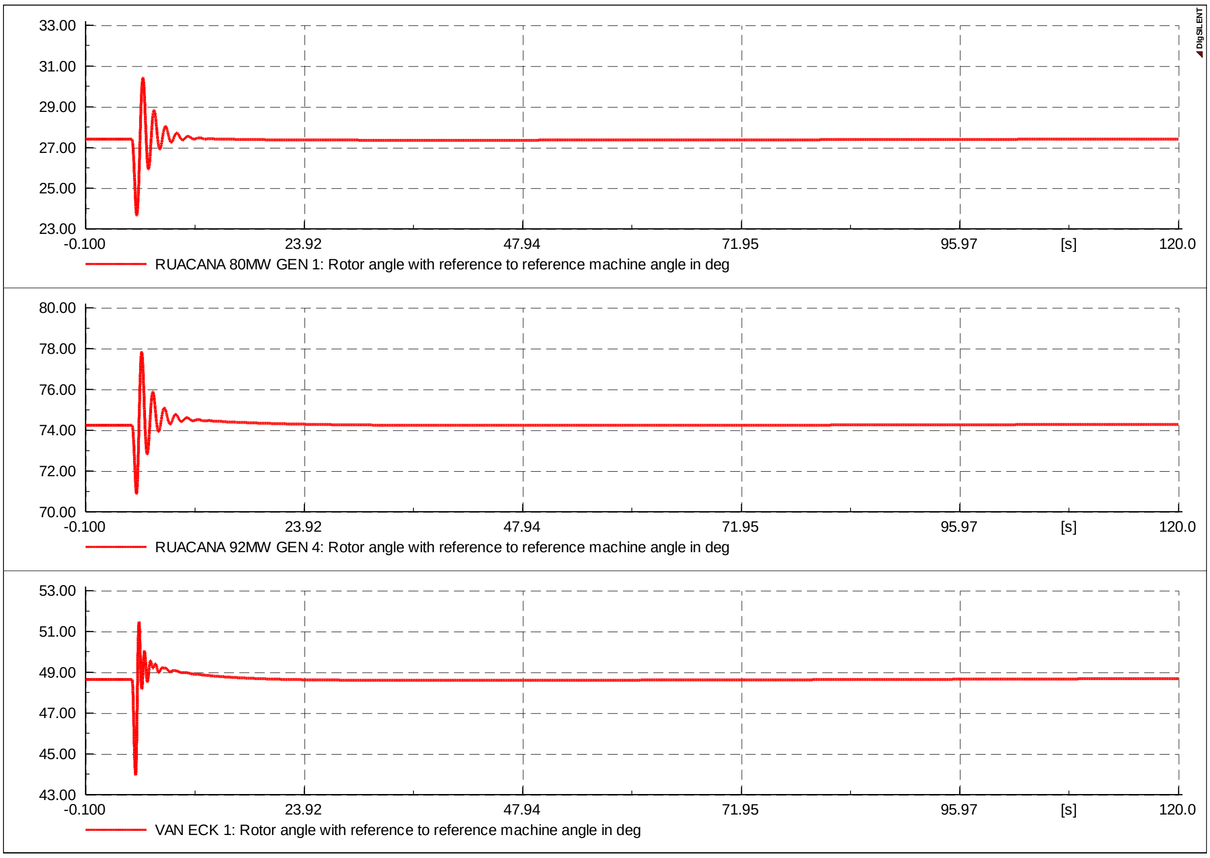

Figure 4-20: Scenario 3 rotor angle with reference to the reference machine angle

Scenario 4: Three-phase short-circuit fault on the 330 kV Ruacana-Omburu Line.

The rotor angle of Ruacana Generator 4 drops to 0° as the 330 kV Ruacana- Omburu line is disconnected as shown in Figure 4-21 below. However, the generators' speed at Ruacana continues rising with time as the generators continue to produce more reactive power than active power when the fault is cleared. The disconnection of the line significantly affects the stability of the power system as the generators at Ruacana lose their synchronism due to the loss of the transmission line supplying the load. The rotor angle of Van Eck Generator 1 experiences a large swing with a maximum peak of 54.594° and a minimum peak of 34.225° as seen in Figure 4-21. The rotor angle then steadily stabilises to a new equilibrium value after the oscillations are damped out. The voltage magnitude at Ruacana BB1 rises to 1.36 p.u. whereas that of Omburu BB1 rises to 1.04 p.u. which is still within the maximum set value of 1.05 p.u.

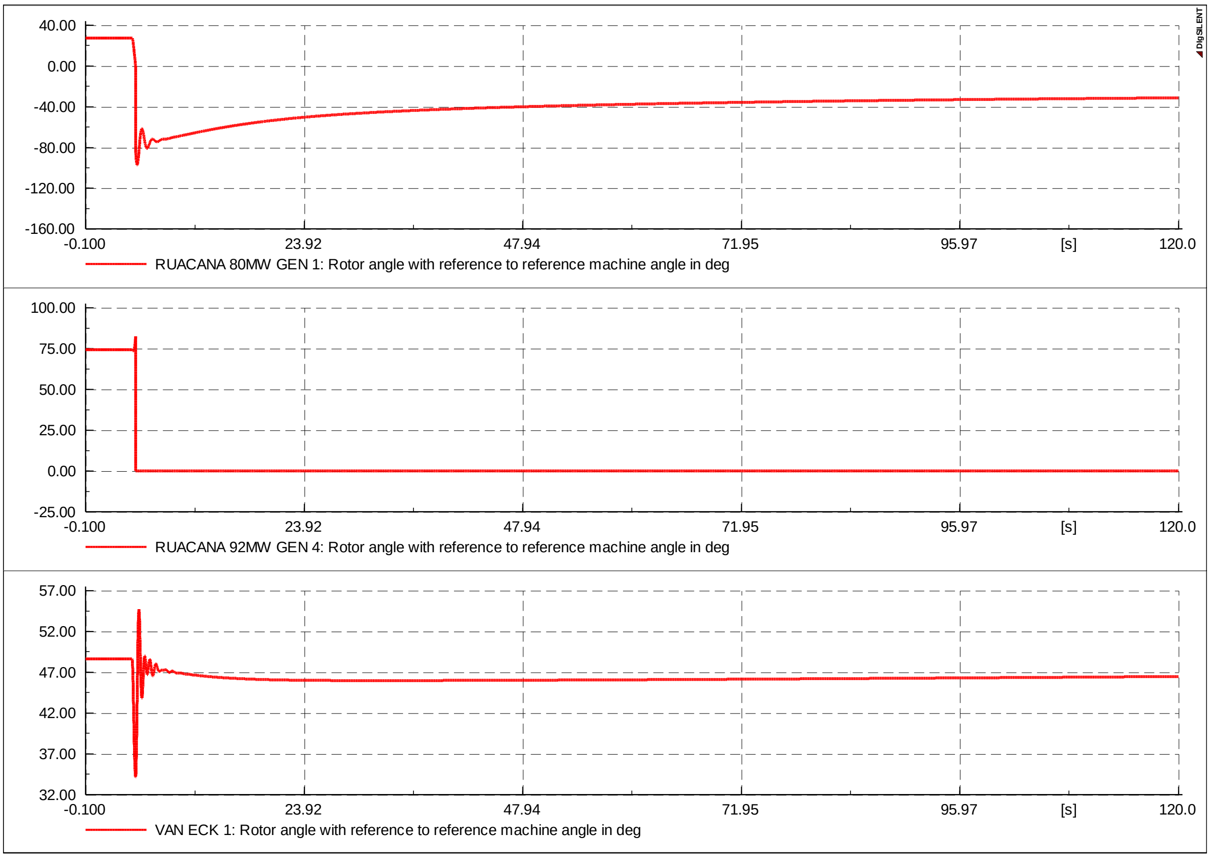

Figure 4-21: Scenario 4 rotor angle with reference to the reference machine angle

Scenario 5: Load rejection by tripping Generator 1 at Ruacana

The rotor angle with reference to the machine angle of Ruacana Generator 1 drops to 0° as the generator is tripped. The rotor angle of Ruacana Generator 4 swings down to a minimum peak value of 72.271° before the oscillations are damped out, rises, and settles at a steady state value of 74.273°, thus maintaining rotor angle stability as shown in Figure 4-22 below. The tripping of Ruacana Generator 1 does not adversely affect the other generators at the station. The rotor angle for Van Eck Generator 1 undergoes oscillations which are then damped out, but the rotor angle continues to rise to a new steady-state value, also maintaining synchronism. The voltages at Ruacana BB1, Omburu BB2 and Kokerboom BB2 also experience a slight drop as Ruacana Generator 1 is removed but still remain within the set voltage limits at 1.01p.u.,1.02 p.u. and 1.03 p.u. respectively.

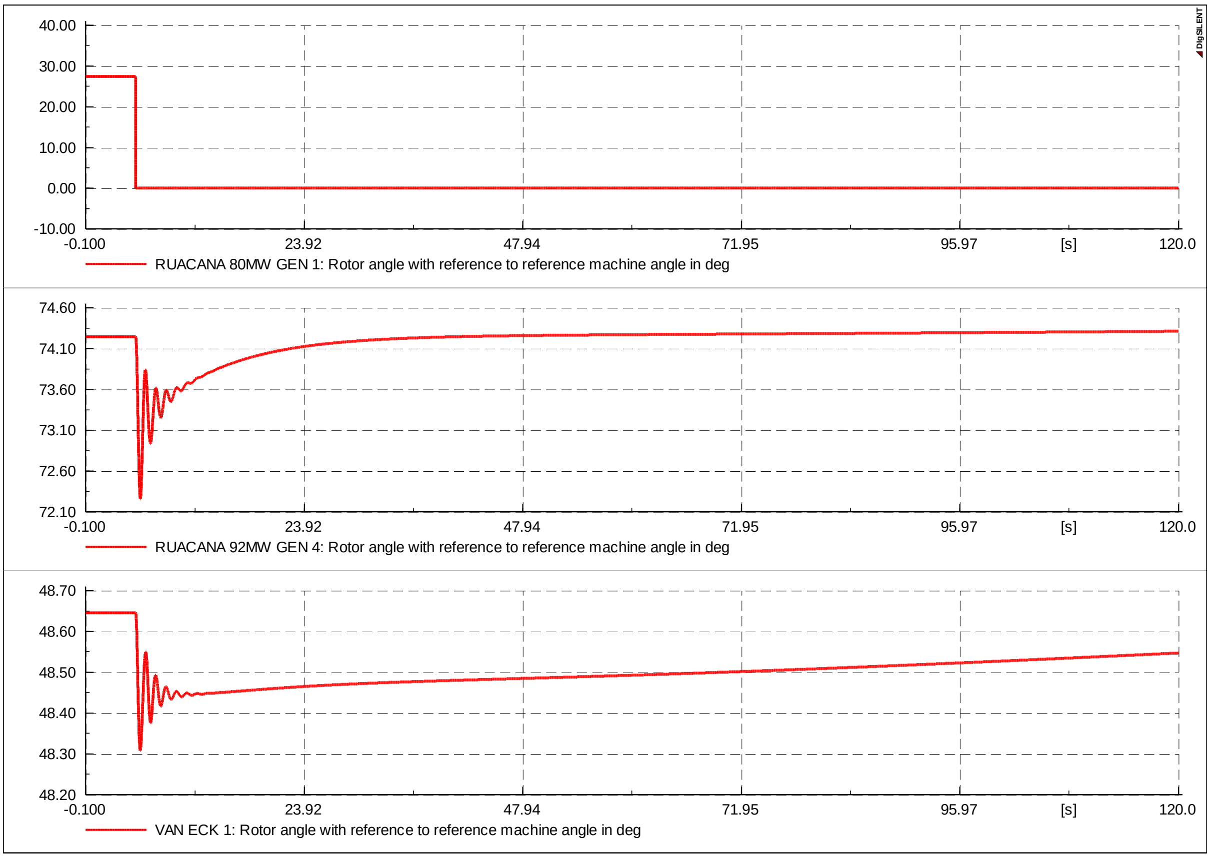

Figure 4-22: Scenario 5 rotor angle with reference to the reference machine angle

4.3.2.1 *Critical Clearing Time*

The results of the Critical Fault Screening Script (CFSS) that was run on the Auas-Kokerboom 400 kV line indicate that the critical clearing time of the reduced NamPower network is one second. All contingency events within the network should be cleared within one second in order for the synchronous generators to maintain rotor angle stability.

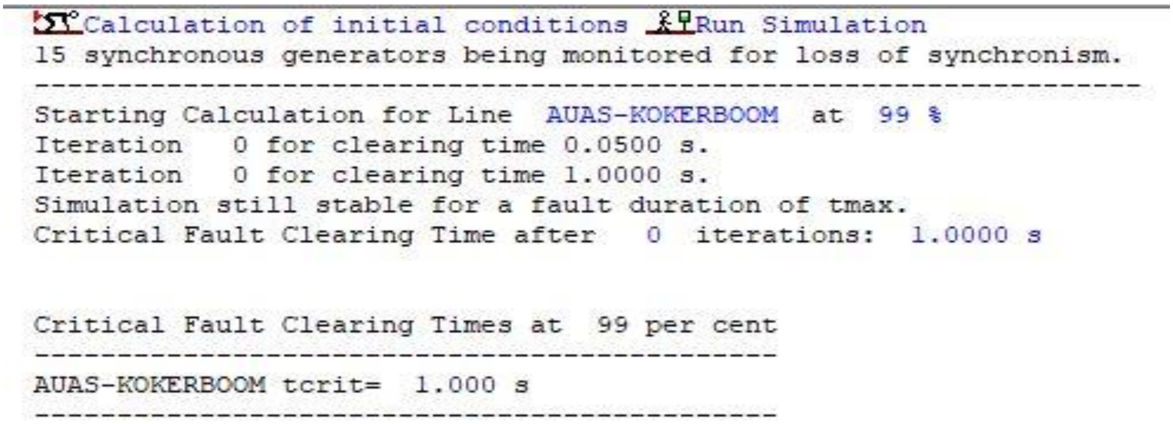

```
Calculation of initial conditions  Run Simulation
15 synchronous generators being monitored for loss of synchronism.
--------------------------------------------------------------------
Starting Calculation for Line  AUAS-KOKERBOOM  at  99 %
Iteration    0 for clearing time 0.0500 s.
Iteration    0 for clearing time 1.0000 s.
Simulation still stable for a fault duration of tmax.
Critical Fault Clearing Time after   0  iterations:  1.0000 s


Critical Fault Clearing Times at  99 per cent
---------------------------------------------
AUAS-KOKERBOOM tcrit=  1.000 s
---------------------------------------------
```

Figure 4-23: Critical Fault Screening Script (CFSS) of the NamPower reduced network

4.3.3 Small-Signal Stability Analysis

The modal analysis results in a total of 96 modes and all these modes have a negative real part. Therefore, the power system is considered to be stable as all the eigenvalues are located in the left-half plane. There are also 15 pairs of oscillatory modes with the most poorly damped modes shown in Table 4-5 below. All the oscillatory modes in Table 4-5 are local area oscillations as the generators in the system oscillate against each other. If not damped out in the required time, these oscillations may cause the failure of the backbone transmission lines that interconnect the generators. Modes 5,95, and 96 have a damping ratio of 0.

Table 4-5: Poorly damped oscillatory modes

Mode	**Real Part (1/s)**	**Imaginary Part (rad/s)**	**Damped Frequency (Hz)**	**Damping Ratio**
29 & 30	-1.540	±10.464	1.665	0.146
34 & 35	-0.924	±7.251	1.154	0.126
36 & 37	-1.984	±8.333	1.326	0.232
38 & 39	-1.803	±8.262	1.315	0.213
44 & 45	-0.732	±5.121	0.815	0.142
50 & 51	-2.039	±9.641	1.534	0.207
52 & 53	-2.039	±9.641	1.534	0.207
54 & 55	-2.354	±8.754	1.393	0.260
56 & 57	-2.354	±8.754	1.393	0.260

The largest participation factors in terms of the state variables are the speed Axis flux (psiQ) and the D Axis flux(psiD). Thus, the participation factor of these state variables is one for the majority of the system modes.

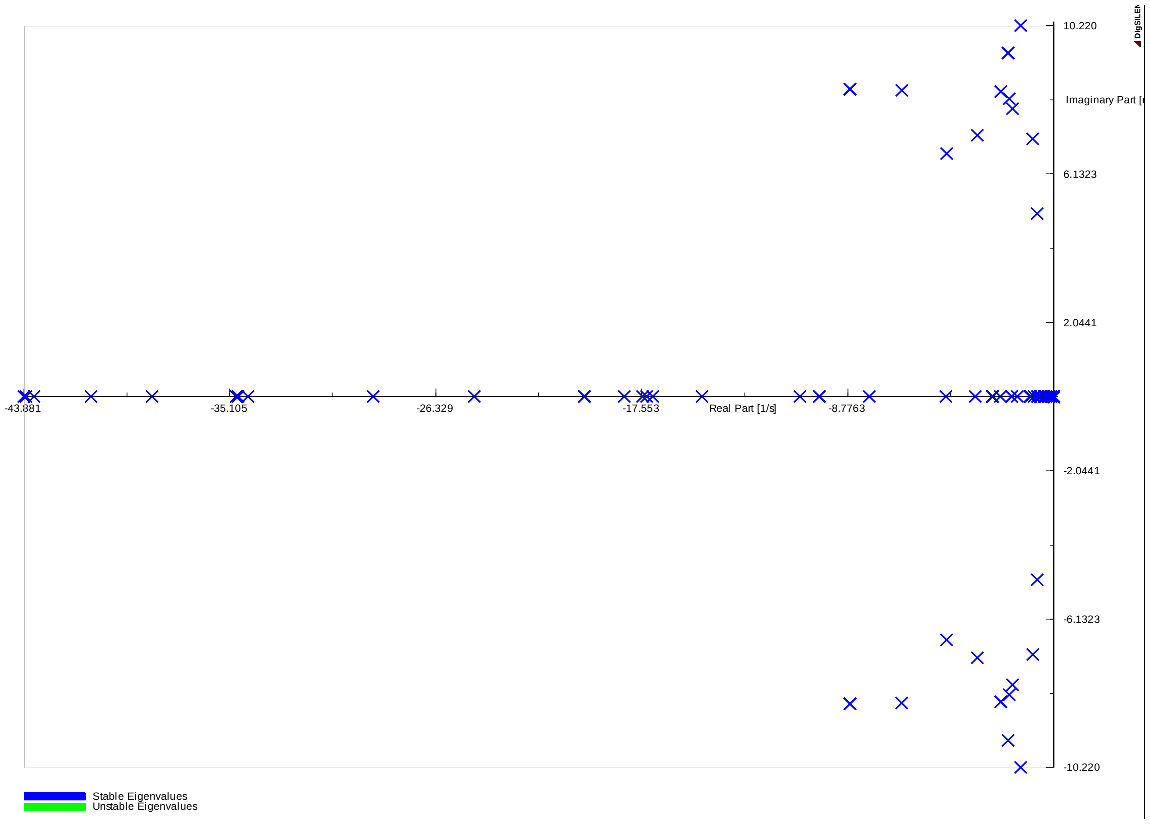

Figure 4-24: Eigenvalue plot of the reduced NamPower network model

4.3.4 Summary

The introduction of three-phase short circuit events on the 400 kV lines that link the NamPower grid to ESKOM through Aries had a significant effect on the rotor angle stability of the synchronous generators in the network as well as on the voltage. The synchronous generators at both Ruacana and Van Eck are unable to arrive at a new equilibrium point after the fault is cleared as they experience a slip, even after the oscillation is damped out and the contingency event has been cleared. Moreover, the voltage within the network collapses to as low as 0.226 p.u. at Kokerboom BB2 in Scenario 1 and 0.228 p.u. at Auas BB2 in Scenario 2 as the fault occurs. The drastic collapse of the voltage pushes the static compensators and filters in the network to their limit as they aim to provide voltage support. The synchronous generators at Ruacana have very low rotor angle values for Scenario 4 and are largely observed to produce reactive power to assist with reactive power compensation. The increase in the reactive power also causes an increase in the busbar voltage at Ruacana BB1 to 1.32 p.u. The modal analysis results indicate that the system is stable as all the eigen values are in the left-half plane. However, the poorly damped modes in Tables 4-5 need to be monitored as the offshore wind farms are integrated to the network.

4.4 Integrated Network with Offshore Wind Farm Integration

Offshore wind farms that are rated at 50 MW,100 MW,200 MW, and 300 MW were coupled to the NamPower reduced network via two parallel 400 kV,30 km overhead lines that run from the Onshore Slack bus (400 kV) to Kokerboom BB2 (400 kV). Load flow, transient stability, and modal analysis are carried out to better understand the integrated network's steady state and post-fault parameters. The transient stability analysis of the integrated network model was carried out by introducing a number of faults on the powerlines that make up NamPower’s transmission network backbone as well as on major busbars of the offshore wind farm and VSC-HVDC link. The short-circuit faults were introduced after 5s and were cleared by disconnecting the affected transmission lines and busbars. The contingency events on the integrated network were carried out as per the following scenarios:

- **Scenario 1: Three-phase short-circuit fault on the 400 kV Aries-Kokerboom line**
- **Scenario 2: Three-phase short-circuit fault on the 400 kV Auas-Kokerboom line**
- **Scenario 3: Three-phase short-circuit on T_AC Onshore and Onshore Slack Busbars**
- **Scenario 4: Short-circuit on the HVDC Transmission Line**

Modal analysis was carried out by plotting the eigen values of the network and by observing the major participating factors of the different mode pairs.

4.4.1 Load Flow Analysis

The efficiency with which power is transferred from the offshore wind farm to the NamPower grid improves as the offshore wind farms' penetration level increases from 50 MW to 300 MW. The power transfer losses from a 50 MW offshore wind farm are 11.6%, whereas a 300 MW offshore wind farm is only 3.1%. The voltage levels within the NamPower network also improve significantly as the offshore wind farms' penetration levels increases due to an increase in the reactive power support provided by the offshore wind farms. The voltage levels at Kokerboom BB2 and Auas BB2 stabilize to 1.03 p.u. and 1 p.u., respectively, as offshore wind farms offer a higher capacity are integrated into the NamPower network. The offshore wind farm and VSC-HVDC scheme provide a maximum of 26.54 MVAr to the NamPower grid as reactive power compensation.

Table 4-6: Voltage at busbars

	Element	Rated Voltage (kV)	Actual Voltage (kV)	Voltage (p.u.)
50 MW	T_AC Onshore busbar	110	110.2	1.00
	Onshore Slack busbar	400	416.7	1.04
	Kokerboom BB2	400	416.4	1.04
	Auas BB2	400	411.5	1.03
	Aries BB	400	400.0	1.00
100 MW	T_AC Onshore busbar	110	110.4	1.00
	Onshore Slack busbar	400	417.5	1.04
	Kokerboom BB2	400	417.0	1.04
	Auas BB2	400	411.1	1.03
	Aries BB	400	400.0	1.00
200 MW	T_AC Onshore busbar	110	110.4	1.00
	Onshore Slack busbar	400	417.0	1.04
	Kokerboom BB2	400	416.2	1.04
	Auas BB2	400	407.1	1.02
	Aries BB	400	400.0	1.00
300 MW	T_AC Onshore busbar	110	111.0	1.01
	Onshore Slack busbar	400	414.5	1.04
	Kokerboom BB2	400	413.3	1.03
	Auas BB2	400	400.0	1.00
	Aries BB	400	400.0	1.00

4.4.2 Scenario 1: Three-phase Short-circuit on the 400 kV Aries-Kokerboom Line

A three-phase short circuit fault was introduced on the Aries-Kokerboom line. The fault was introduced at five seconds and was cleared between 100 ms and 400 ms after the fault by disconnecting the line. The rotor angle stability of the generators at Ruacana and Van Eck was not maintained after the fault was cleared, as seen in Figure 4-25 and Table 4-7 below. The 200 MW offshore wind farm had the shortest fault clearing time of 100 ms, whereas the same fault could be cleared beyond 400 ms for the 50 MW and 300 MW offshore wind farm installations. The reactive power compensation provided by the HVDC link for the fault decreases as the capacity of the offshore wind farm increases from 50 MW to 300 MW. The voltages at both Kokerboom, BB2, and Aries BB remain within the acceptable limits as the fault is cleared.

Table 4-7: Scenario 1 results

	Fault clearing time (ms)	**Rotor angle stability maintained?**	**Reactive power compensation from offshore wind farm and VSC-HVDC Link (MVAR)**	**Kokerboom BB2 Voltage (p.u.)**	**Aries BB Voltage (p.u.)**
50 MW	400	No	161.6	0.99	0.97
100 MW	200	No	156.8	0.99	0.97
200 MW	100	No	151.4	0.99	0.97
300 MW	400	No	151.2	0.99	0.97

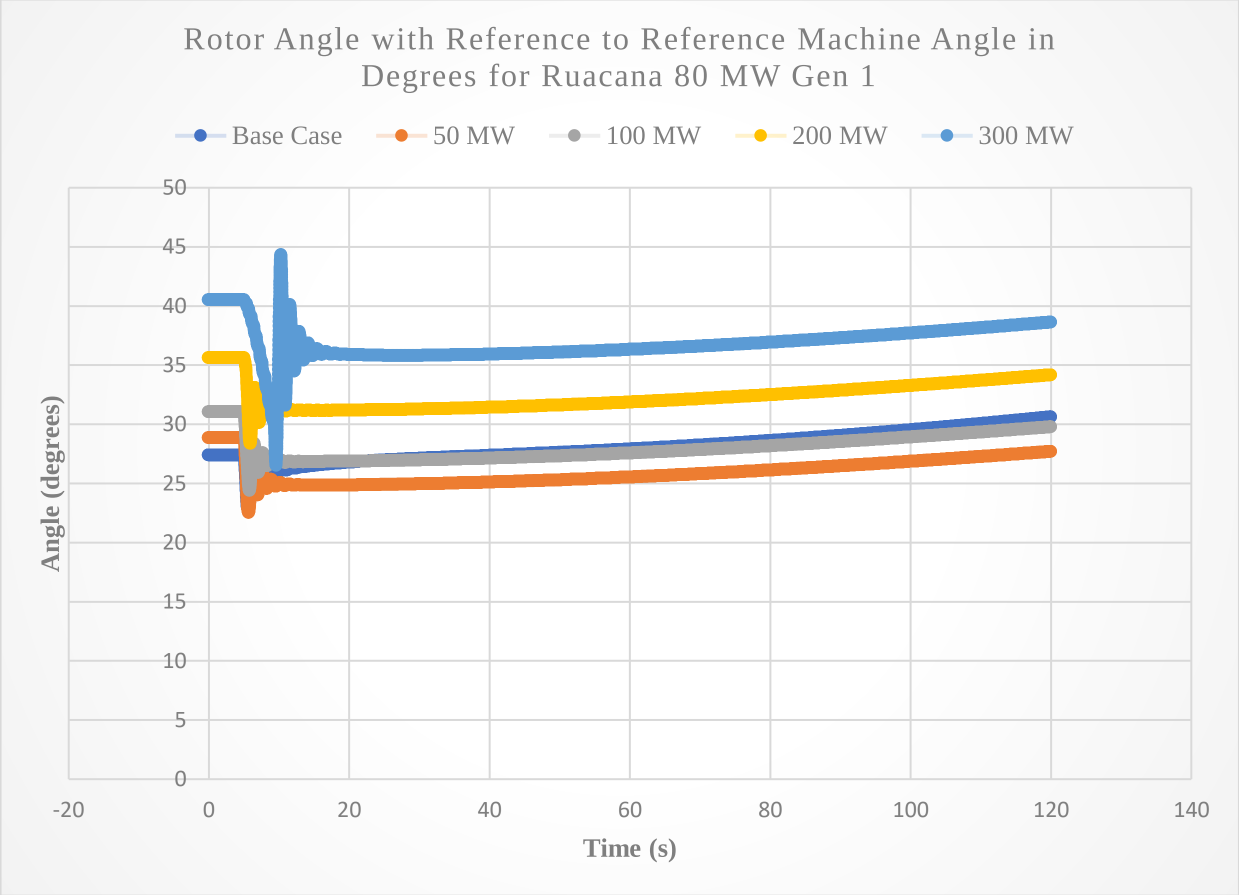

Figure 4-25: Rotor angle with reference to the reference machine angle in degrees for Ruacana Generator 1

4.4.3 Scenario 2: Three-phase Short-circuit on the 400 kV Auas-Kokerboom Line

A three-phase short circuit fault was introduced on the Auas-Kokerboom line. The fault was introduced at five seconds and was cleared between 100 ms and 400 ms by disconnecting the line. The rotor angle stability of the generators at Ruacana and Van Eck was not maintained as the generator goes out of step even after the fault is cleared, as seen in Figure 4-26 and Table 4-8 below. The reactive power compensation provided by the VSC-HVDC link for the fault increases as the capacity of the offshore wind farm increases from 50 MW to 300 MW. The voltages at both Kokerboom BB2 and the Onshore Slack BB remain within the acceptable limits as the fault is cleared. On the other hand, the voltage at Auas BB2 collapses to as low as 0.6 p.u. when a 300 MW offshore wind farm is coupled to the onshore ac grid.

Table 4-8: Scenario 2 results

	Fault clearing time (ms)	**Rotor angle stability maintained?**	**Reactive power compensation from offshore wind farm (MVAR)**	**Kokerboom BB2 Voltage (p.u.)**	**Auas BB2 Voltage (p.u.)**
50 MW	400	No	151.7	1.00	0.81
100 MW	400	No	155.0	1.00	0.80
200 MW	100	No	163.0	0.99	0.75
300 MW	400	No	188.5	0.98	0.60

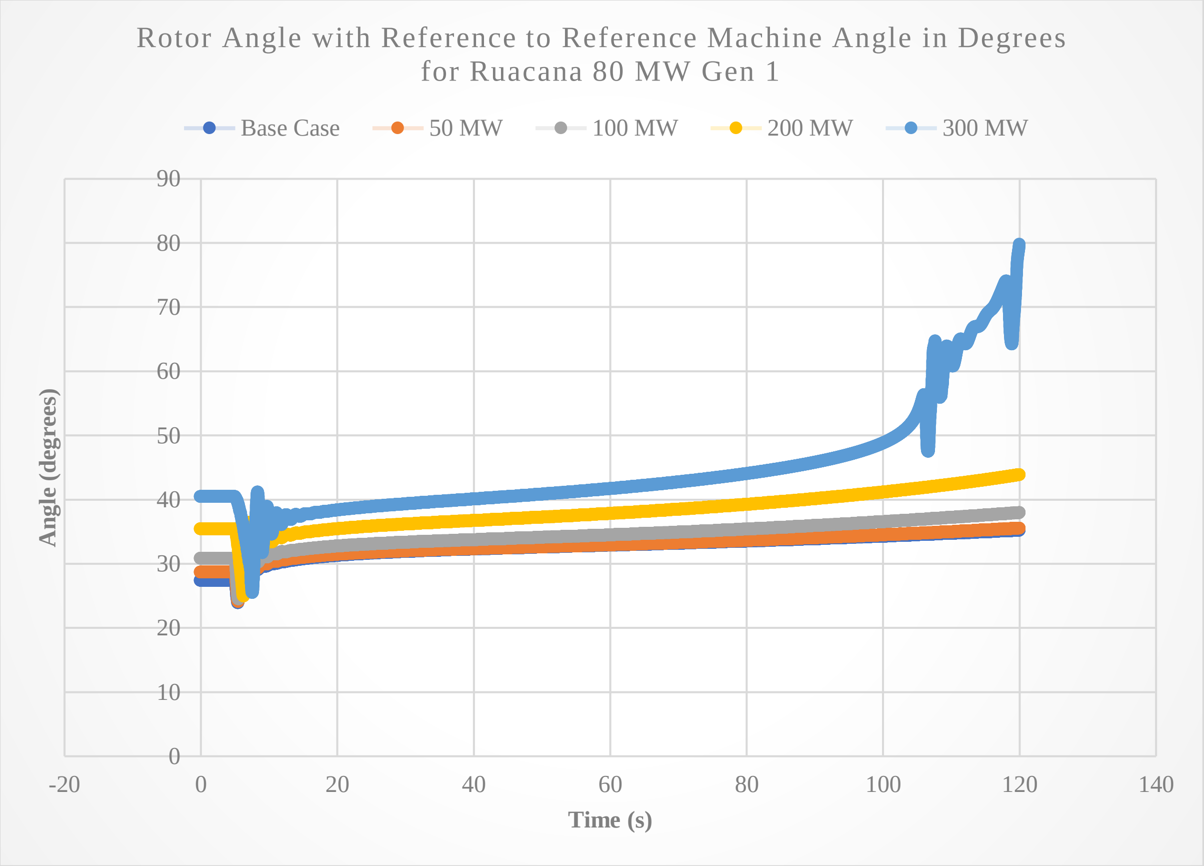

Figure 4-26: Scenario 2 rotor angle with reference to the machine angle with 300 MW offshore wind farm integrated

4.4.4 Scenario 3: Three-phase short-circuit on T_AC Onshore and Onshore Slack Busbar

A three-phase short-circuit fault is applied on the T_AC Onshore and Onshore Slack busbars by using the DIgSILENT Complete Method. The results of the short-circuit analysis will determine the size and settings of the protection devices that are to be installed at the point of common coupling. The fault has a breaking time of 0.1s and is cleared within 1s.

Table 4-9: Short-circuit analysis results

	Element	**SK" (MVA)**	**IK" (kA)**	**IK' (kA)**
50 MW	T_AC Onshore busbar	1808.74	9.493	10.191
	Onshore Slack busbar	2524.05	3.643	3.772

100 MW	T_AC Onshore busbar	1803.54	9.466	10.169
	Onshore Slack busbar	2517.31	3.633	3.765
200 MW	T_AC Onshore busbar	1787.40	9.381	10.096
	Onshore Slack busbar	2495.24	3.602	3.738
300 MW	T_AC Onshore busbar	1758.50	9.230	9.953
	Onshore Slack busbar	2462.79	3.555	3.697

The short-circuit capacity in MVA (SK”) decreases by 2.43% as the capacity of the offshore wind farms increases from 50 MW to 300 MW. This may be due to the reactive power compensation provided by the VSC-HVDC link and the SVCs within the AC network as the fault occurs. The sub-transient short-circuit current (IK”) and transient short-circuit current (IK’) also experience a decrease as the capacity of the offshore wind farms increases as seen in Table 4-9 above. This means the sizes of the relevant protection equipment would also decrease and become more economical as the wind farms' capacity increases.

4.4.5 Scenario 4: Short-circuit on HVDC Transmission Line

A short-circuit fault is applied to the positive HVDC transmission line at five seconds. The line is re-energized by clearing the fault after 20 ms. The rotor angle undergoes oscillation for the duration of the fault and then stabilizes to the pre-fault value as shown from Figure 4-27 to Figure 4-30. The rotor angle stability of both the generators at Ruacana and Van Eck and the voltage ratings of the busbars of the onshore network are not adversely affected by the fault occurrence as the HVDC link isolates the DC fault from the onshore AC network. The bulk of the power is transferred through the negative DC line when the fault occurs on the positive DC line. There is no convergence in the simulation when the fault is cleared beyond 20 ms.

Table 4-10: Scenario 4 transient stability results

	Rotor angle stability maintained?	**Positive DC line power transfer (MW)**	**Negative DC line power transfer (MW)**	**Onshore Slack BB Voltage (p.u.)**	**Kokerboom BB2 Voltage (p.u.)**
50 MW	Yes	1.1	45.9	1.04	1.04
100 MW	Yes	1.4	95.4	1.05	1.04
200 MW	Yes	1.2	197.2	1.04	1.04
300 MW	Yes	5.1	299.6	1.04	1.03

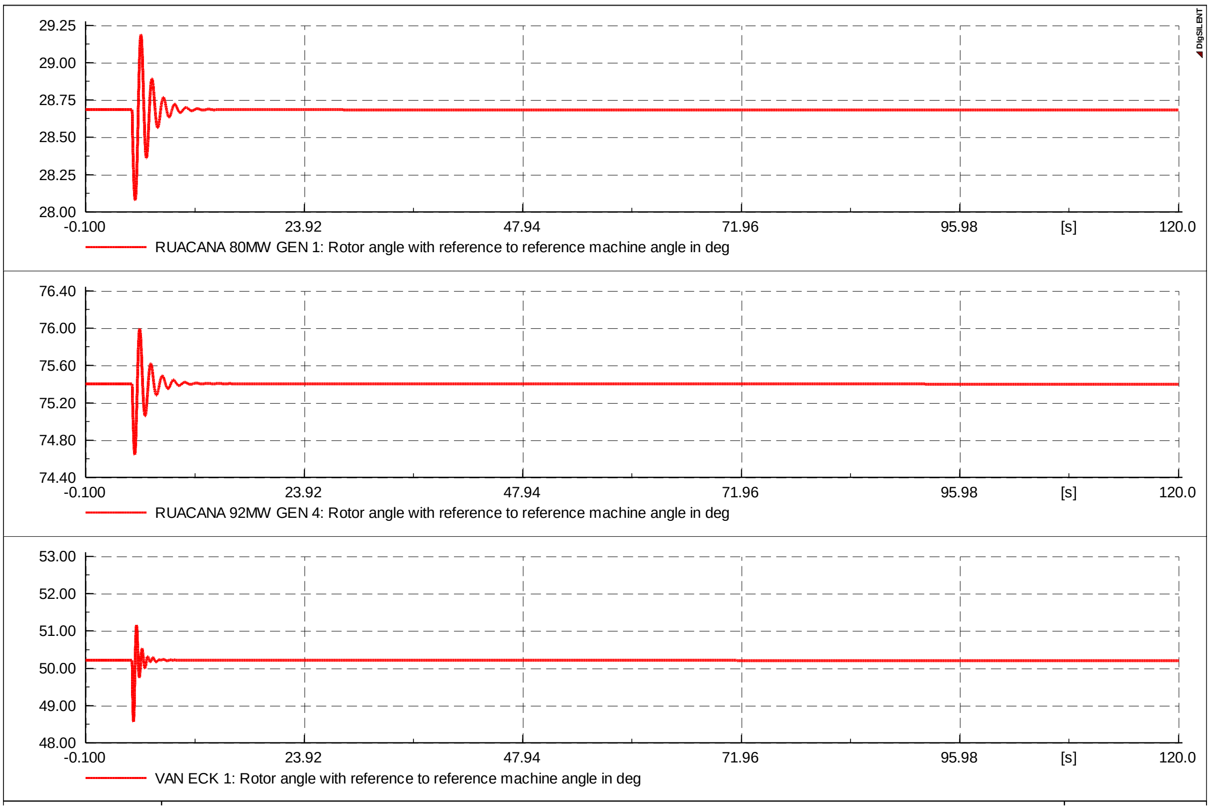

Figure 4-27: Scenario 4 rotor angle with reference to the machine angle for HVDC line fault with 50MW offshore wind farm integrated

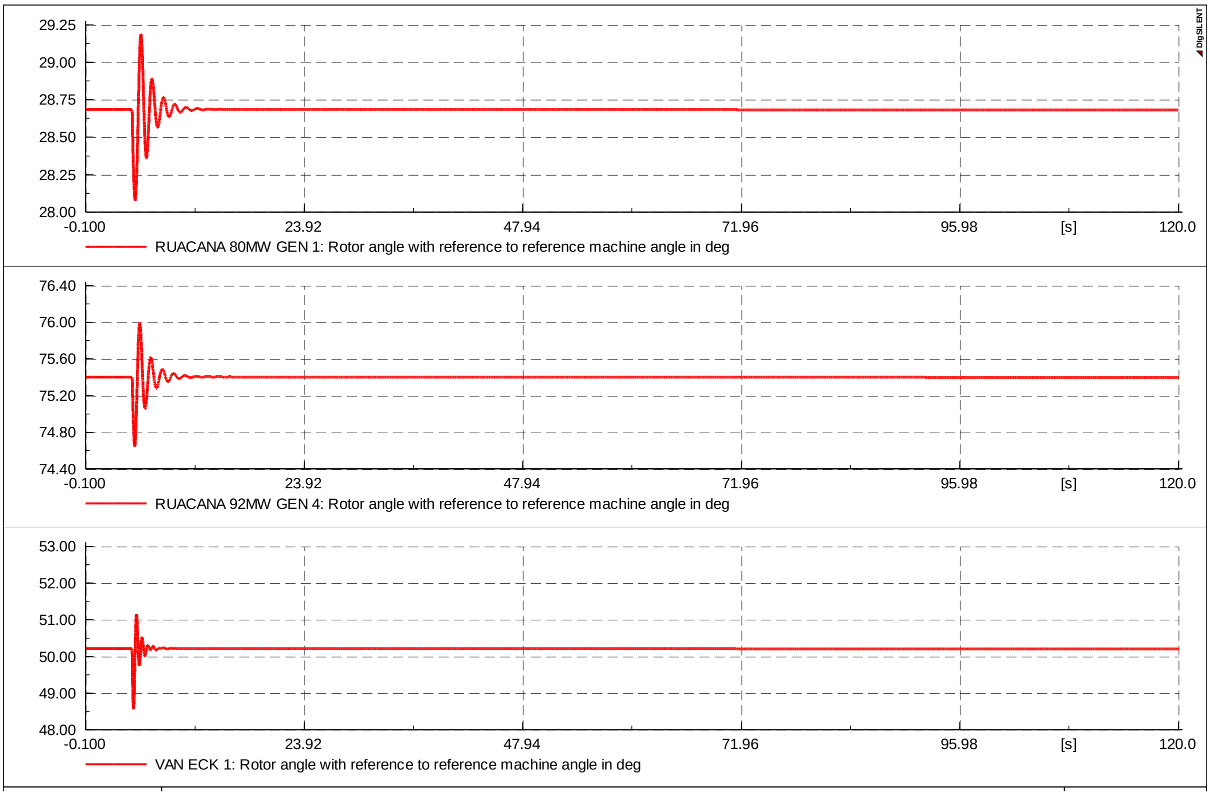

Figure 4-28: Scenario 4 rotor angle with reference to the machine angle for HVDC line fault with 100MW offshore wind farm integrated

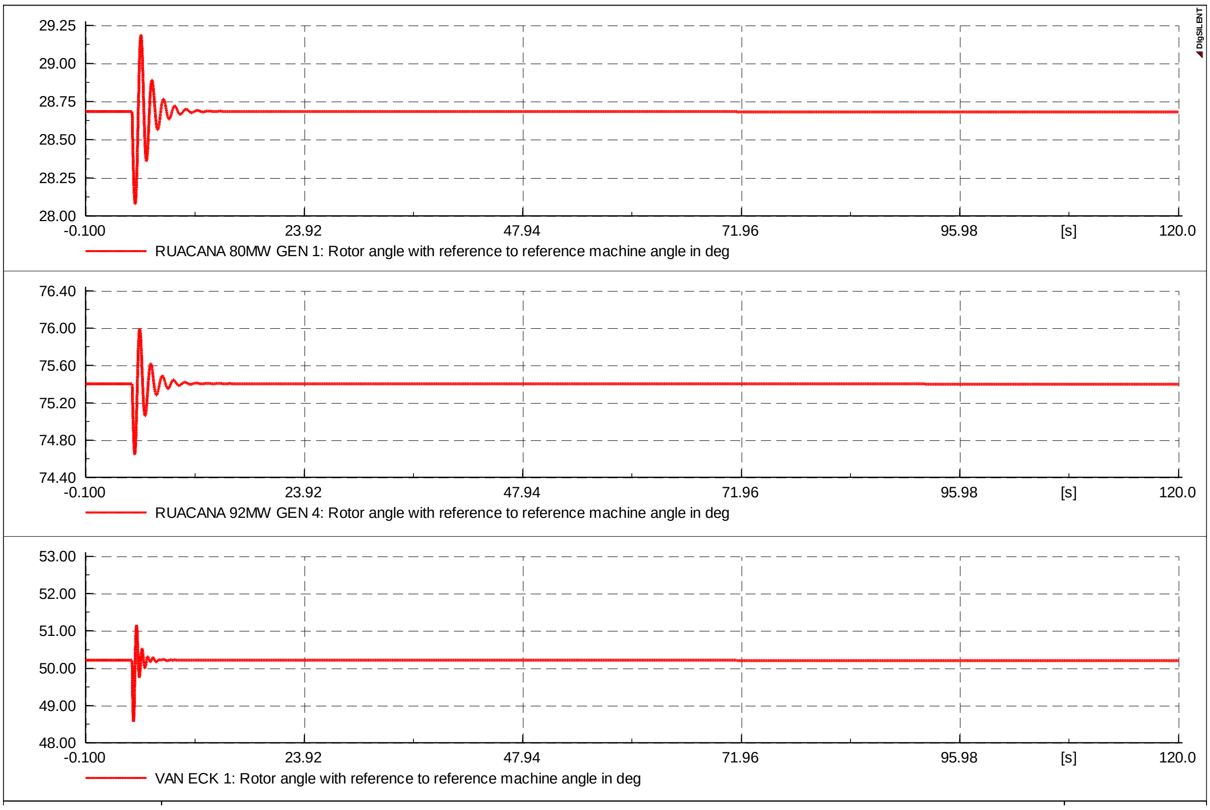

Figure 4-29: Scenario 4 rotor angle with reference to the machine angle for HVDC line fault with 200MW offshore wind farm integrated

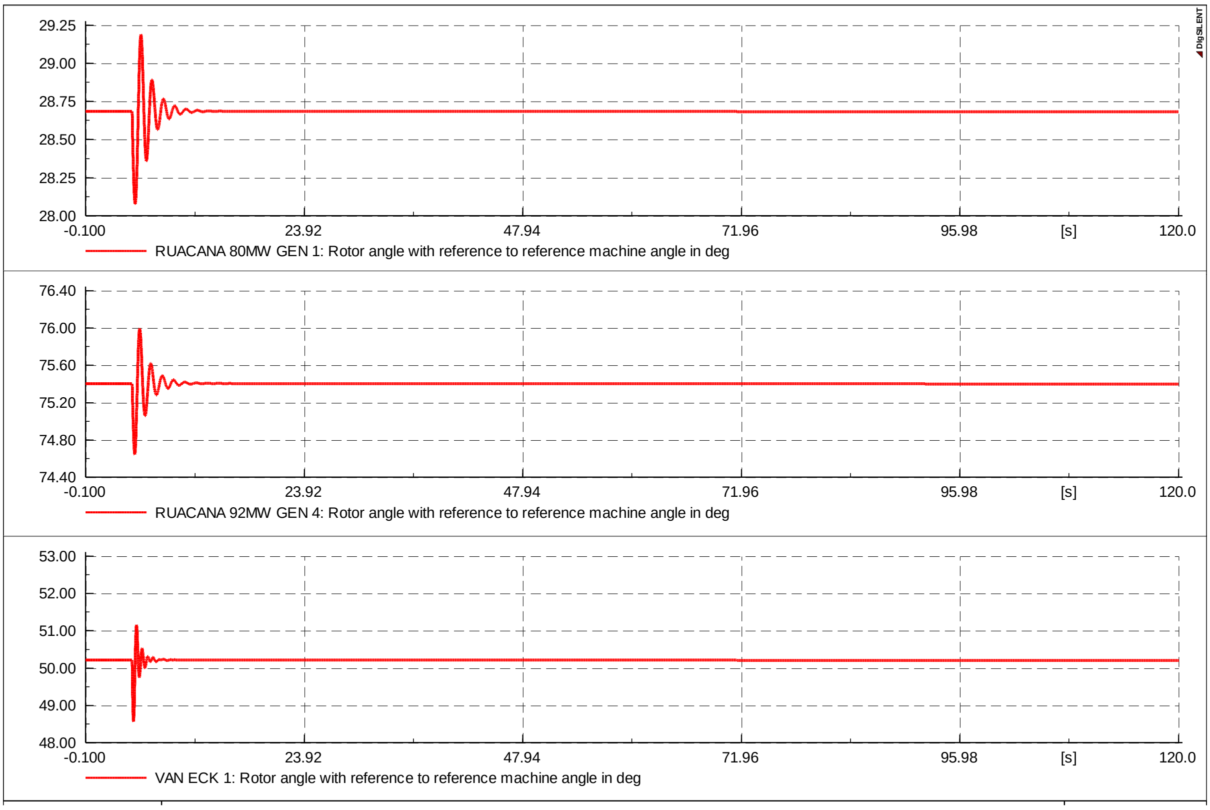

Figure 4-30: Scenario 4 rotor angle with reference to the reference machine angle with 300MW offshore wind farm integrated

4.4.6 Fault Levels

The short-circuit levels of the network were calculated in DIgSILENT PowerFactory using the complete method as it takes into account the effects of the wind turbines on the fault levels. The fault level at the point of common coupling (PCC) and the short-circuit ratio (SCR) decrease as the penetration level of the offshore wind farm increases as shown in Table 4-11 below. The decrease in the SCR indicates that the strength of the grid decreases with the increase in offshore wind farm integration.

The short-circuit ratio is calculated with the point of common coupling taken as Kokerboom BB2 with a short-circuit level reading of 2796.3 MVA. The short-circuit ratio experiences a decline as the penetration level of the offshore wind farm increases. The grid strength in terms of the short-circuit ratio is therefore compromised with the increase in wind farm penetration level.

Table 4-11:Short-circuit analysis results

	Element	**SK” (MVA)**	**IK” (kA)**	**IK’ (kA)**	**SCR**
50 MW	Onshore Slack busbar	2518.52	3.635	3.765	55.926
	Kokerboom BB2	2731.90	3.943	4.063	
100 MW	Onshore Slack busbar	2511.56	3.625	3.757	27.963
	Kokerboom BB2	2724.31	3.932	4.055	
200 MW	Onshore Slack busbar	2488.94	3.592	3.729	13.982
	Kokerbomm BB2	2699.66	3.897	4.024	
300 MW	Onshore Slack busbar	2457.87	3.548	3.690	9.321
	Kokerboom BB2	2665.28	3.847	3.980	

4.4.7 Critical Clearing Time

The critical fault screening script (CFSS) results indicate that the critical clearing time of the network is one second as per Figure 4-31 below. Therefore, there is no change in the critical clearing time for the reduced NamPower network model and the model with the integrated offshore wind farms.

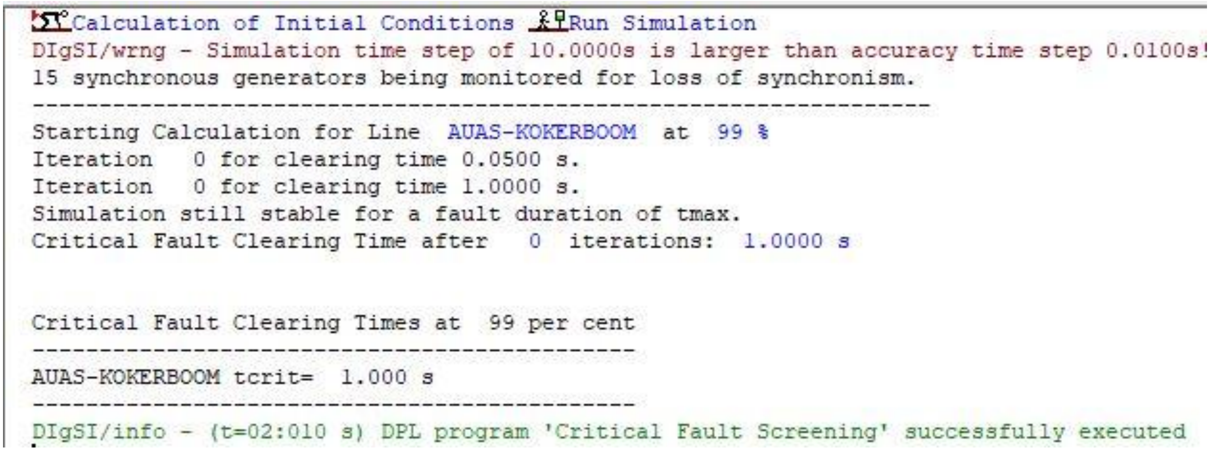

```
Calculation of Initial Conditions  Run Simulation
DIgSI/wrng - Simulation time step of 10.0000s is larger than accuracy time step 0.0100s!
15 synchronous generators being monitored for loss of synchronism.
------------------------------------------------------------------
Starting Calculation for Line  AUAS-KOKERBOOM  at  99 %
Iteration   0 for clearing time 0.0500 s.
Iteration   0 for clearing time 1.0000 s.
Simulation still stable for a fault duration of tmax.
Critical Fault Clearing Time after   0  iterations:  1.0000 s


Critical Fault Clearing Times at  99 per cent
--------------------------------------------
AUAS-KOKERBOOM tcrit=  1.000 s
--------------------------------------------
DIgSI/info - (t=02:010 s) DPL program 'Critical Fault Screening' successfully executed
```

Figure 4-31: Results of critical fault screening script

4.4.8 Small-Signal Stability

The oscillatory modes increase from 101 modes for a 50 MW offshore wind farm to 164 modes for a 300 MW integrated offshore wind farm as seen in Table 4-12. The damping ratios of a large number of the modes indicate that they are local area oscillations. The 200 MW and 300 MW offshore wind farm integrated networks are considered stable as all their eigenvalues have a negative real part as seen in Figure 4-32 and Figure 4-33 respectively. In contrast, the 50 MW and 100 MW installations are considered to be unstable as they have modes (mode 64 for 50 MW and mode 65 for 100 MW) that have positive real parts as seen in Figure 4-32 and Figure 4-33 respectively. In summary, the small-signal stability of the NamPower network is compromised as the eigenvalues migrate towards the left half-plane with the increase in the penetration level of the offshore wind farms as seen from Figures 4-32 to Figure 4-35.

Table 4-12: Small-signal stability results

	50 MW	**100 MW**	**200 MW**	**300 MW**
No. of modes	101	100	132	164
Unstable modes	Mode 64	Mode 65	-	-
No. of control modes	8	7	10	11
No. of oscillatory mode pairs	10	9	14	16

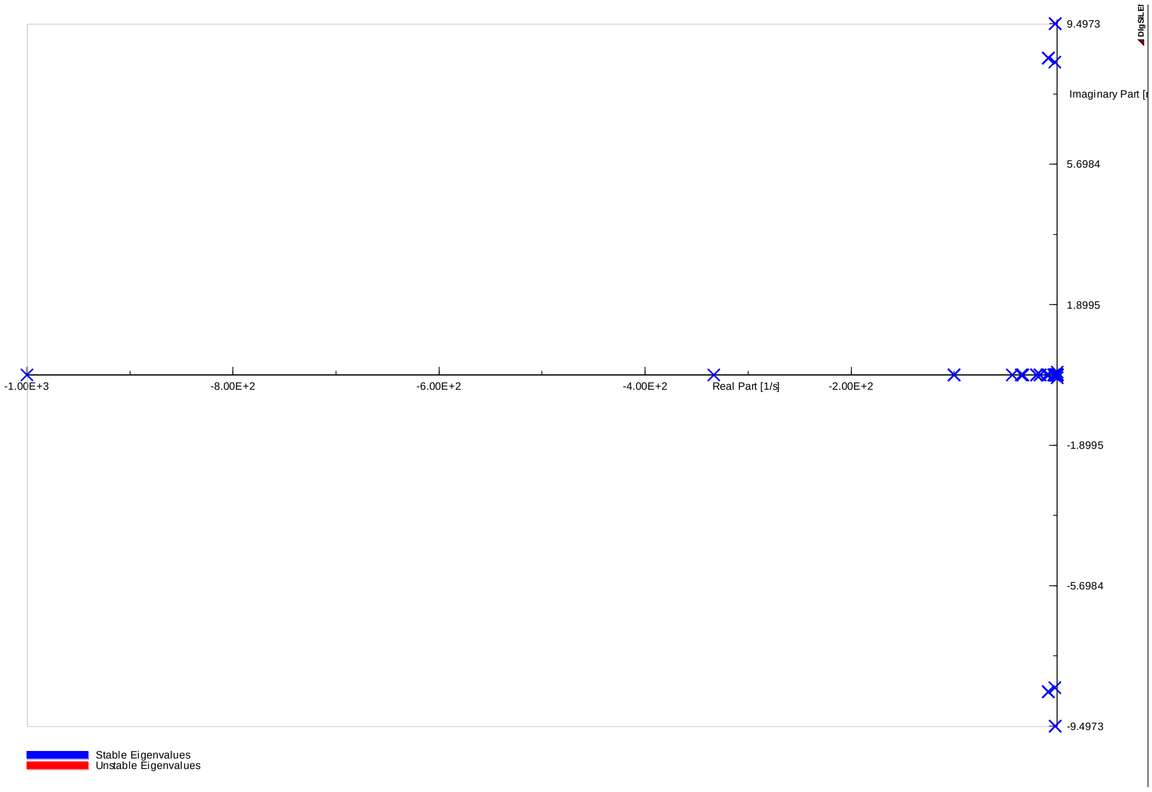

Figure 4-32:Eigenvalue plot of 50MW integrated offshore wind farm

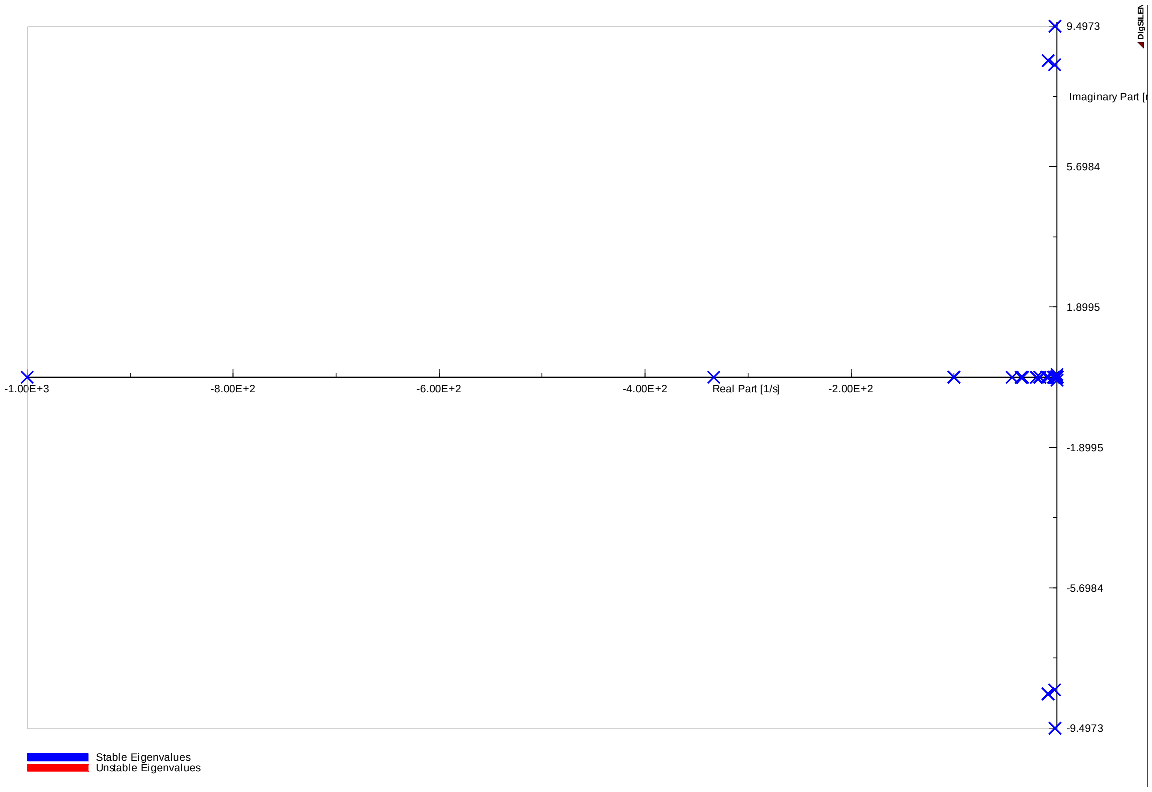

Figure 4-33: Eigenvalue plot of 100MW integrated offshore wind farm

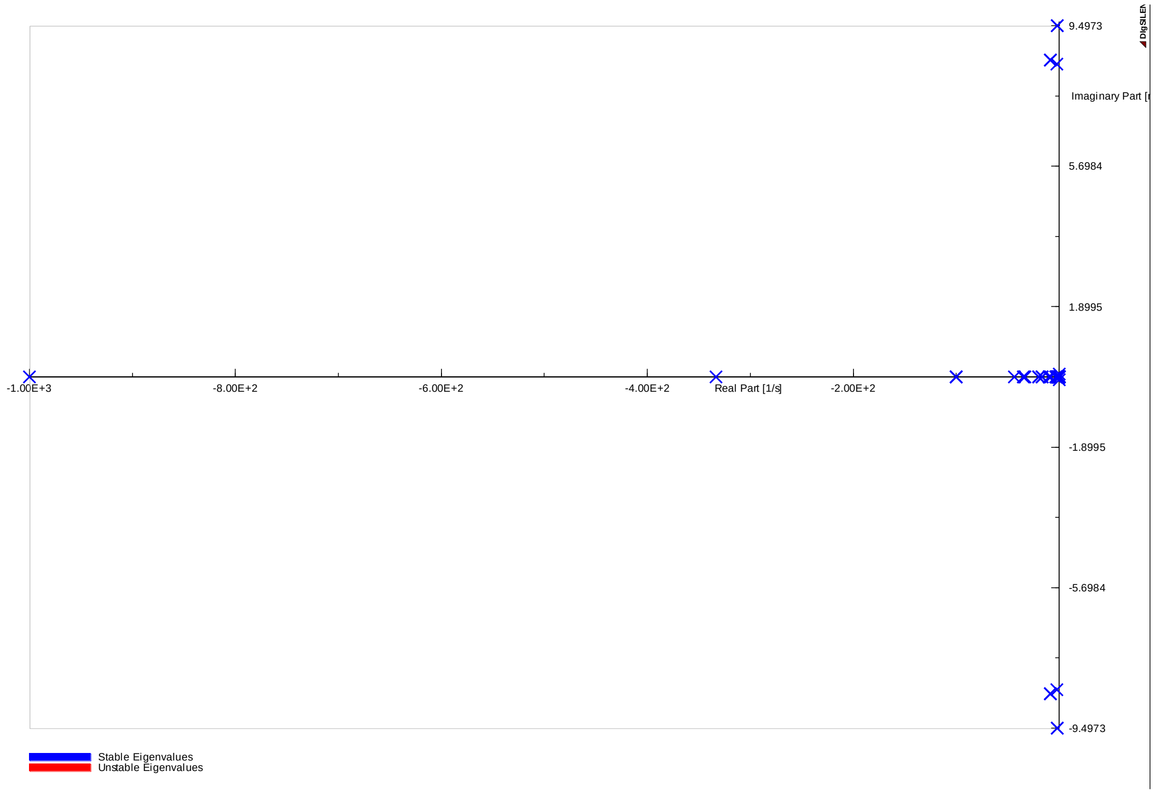

Figure 4-34: Eigenvalue plot of 200MW integrated offshore wind farm

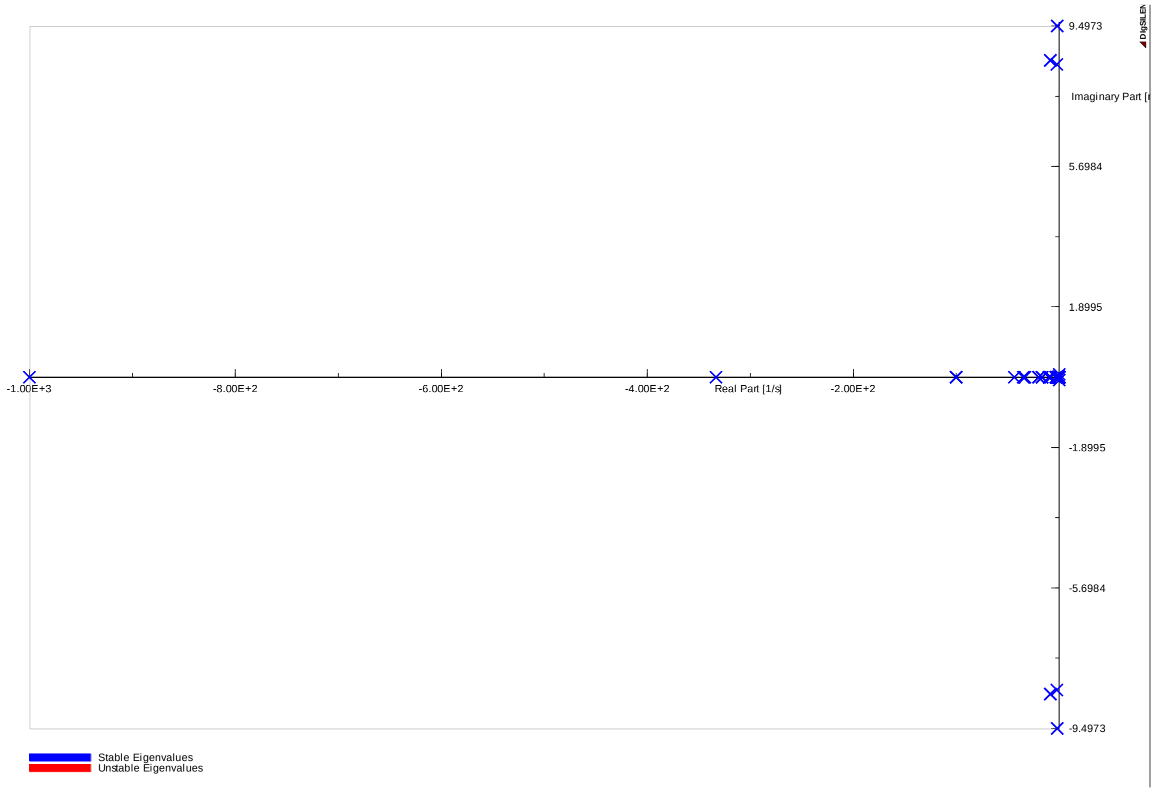

Figure 4-35: Eigenvalue plot of 300MW integrated offshore wind farm

4.4.9 Summary

The transfer of power from the offshore wind farms to the onshore AC network and the voltage levels of the onshore network improve as the capacity of the offshore wind farm increases. In scenario 1, the reactive power injection from the VSC-HVDC link decreases as the offshore wind farm's penetration level increases as the network's voltage levels are not adversely affected. Contrastingly, the reactive power compensation from the VSC-HVDC link increases as the penetration level of the offshore wind farms increases in Scenario 2. The increase in reactive power compensation in Scenario 2 is due to the voltage levels that collapse to as low as 0.6 p.u. as the capacity of the offshore wind farm is coupled to the onshore ac grid increases. The short-circuit levels of the onshore slack busbar, which is the point of common coupling, also decrease as the penetration level of the onshore wind farm increases due to the increase in the equivalent impedance of the system as the number of offshore wind farms increases. In scenario 4, it is shown that faults that occur on the VSC-HVDC do not affect the rotor angle stability and voltage stability of the onshore ac grid. The bi-pole VSC-HVDC link also shows an element of reliability as the power is still transferred even when there is a fault on one of the HVDC lines. The small-signal stability of the network is affected when the 50 MW and 100 MW offshore wind farms are interconnected as eigen values with a positive real part are detected. The small signal stability of the 200 MW and 300 MW offshore wind farms is stable but should be closely monitored as the eigen values migrate towards the right half-plane indicating that the rotor angle continues oscillating with time. The number of oscillatory mode pairs also increases as the penetration level of the offshore wind farms increases from 50 MW to 300 MW.

CHAPTER 5: CONCLUSIONS AND RECOMMENDATIONS

5.1 Conclusions

The following conclusions were observed from the analysis of the results in relation to the research objectives.

- A single machine infinite bus (SMIB) network was modelled as the test bed for transient and small signal stability analysis.
- The SMIB network maintained transient voltage and small-signal stability when subjected to several faults.
- DFIGs were integrated into the SMIB network at different penetration levels through a collector busbar.
- The SMIB network maintained transient and voltage stability when subjected to a number of line faults with the DFIGs coupled to the network.
- The small-signal stability of the SMIB was compromised as the penetration levels of the DFIGs increased from 5 MW to 25 MW.
- Load flow, transient stability, and small-signal stability analysis were carried out on a reduced model of the NamPower network.
- The reduced NamPower network model did not maintain rotor angle stability for contingency events on backbone transmission lines. However, the network is stable in terms of small-signal stability, with all oscillatory modes being local area oscillations.
- Offshore wind farms at different penetration levels were integrated into the reduced NamPower network through a VSC-HVDC link.
- According to the results of the load flow analysis; the efficiency of power transfer from the offshore wind farm to the onshore NamPower network improves as the penetration level of the offshore wind farms increases from 50 MW to 300 MW. There was also an overall improvement in the voltage level of the NamPower network as the penetration level of offshore wind farms increased.
- Rotor angle stability was not maintained for both scenarios 1, and 2 as the rotor angles of all the synchronous generators in the NamPower network continued oscillating over time. All the offshore wind farms, except the 200 MW installation, remained connected to the onshore AC network beyond 200 ms, which is in compliance with the low-voltage ride-through of the Namibian transmission grid-code requirements. The results of the CFSS also indicates that the critical clearing time of the network is one second. The

VSC-HVDC link laboured to improve the voltage levels of the NamPower network by providing maximum reactive power compensation in both scenarios as per the requirements of the Namibian transmission grid code.

- The short-circuit fault levels at the PCC were investigated in scenario 3. The short-circuit fault levels at the PCC experience a decrease as the penetration level of the offshore wind farm increases. This means that cheaper protection equipment will be required.
- The rotor angle stability of the NamPower network and the voltage levels are not affected by faults that occur on the HVDC line. The VSC-HVDC link isolates the onshore AC NamPower network from faults that occur on the offshore wind farm.
- The NamPower network is considered to be have lost small-signal stability when the 50 MW and 100 MW offshore wind farms are integrated as some of the eigen values have positive real parts.
- Small-signal stability is maintained when the 200 MW and 300 MW offshore wind farms are coupled to the NamPower network. However, the small-signal stability should be monitored and improved through the installation of power system stabilizers at optimal locations within the network.

Overall, the integration of offshore wind farms to the reduced NamPower network through a VSC-HVDC scheme does not improve the rotor angle stability but rather negatively affects both the transient stability and the small-signal stability of the network due to the addition of more oscillatory modes. In contrast, the voltage levels within the network show an improvement due to reactive power compensation provided by the VSC-HVDC link. Therefore, the results of this study would give potential offshore wind farm developers insight into the transient stability response of the NamPower network with regards to offshore wind farm integration. These results could also be used to improve the current grid-code by developing guidelines that are exclusively for offshore wind farms.

5.2 Recommendations for Future Research

It is recommended that future research focus on improving the transient stability of the NamPower network through the design and placement of power system stabilizers (PSS), flexible AC transmission system (FACTS) controllers or unified power flow controllers (UPFC) across the network. It is furthermore recommended that the voltage stability of the network be analysed in more detail. The NamPower network is characterized by long transmission lines that are lightly loaded and this will also significantly affect the location of FACTS controllers across the network. The intermittent nature of the wind resource should also be considered to allow for the improvement strategies to be more dynamic in nature.

In addition to the above, the results of the small-signal stability analysis should be used as a precursor for designing and implementing the best control strategy for the VSC-HVDC link and for the best damping strategies of the oscillatory modes that have been highlighted as being unstable. This would improve the network’s response to minor perturbations.

REFERENCES

[1] Electricity Control Board, “Namibia Electricity Supply Industry. National Integrated Resource Plan Review and Update- Final Report,” Ministry of Mines and Energy, Windhoek, Namibia, 2016.

[2] Global Business Network Programme, “Partnership Ready Namibia: Renewable Energy,” Deutsche Gesellschaft für Internationale Zusammenarbeit (GIZ) GmbH, Eschborn, Germany, 2020.

[3] Namibia Power Corporation (Pty) Ltd, “NamPower Annual Report,” Namibia Power Corporation (Pty) Ltd, Windhoek, Namibia,2020.

[4] W. Kruger, O. Alao, and A. Eberhard, "Namibia Country Report. Report 3: Energy and Economic Growth Research Programme," Graduate School of Business, Cape Town, 2019.

[5] E. Tareka and S. Chowdhury, "Statistical Assessment of Potential Wind Energy Sites in Coastal and Southern Part of Namibia," in 2020 International SAUPEC/RobMech/PRASA Conference, 2020: IEEE, pp. 1-6.

[6] M. Barnes, D. Van Hertem, S. P. Teeuwsen, and M. Callavik, "HVDC Systems in Smart Grids," Proceedings of the IEEE, vol. 105, no. 11, pp. 2082-2098, 2017.

[7] S. D. Ahmed, F. S. Al-Ismail, M. Shafiullah, F. A. Al-Sulaiman, and I. M. El-Amin, "Grid Integration Challenges of Wind Energy: A Review," *IEEE Access,* vol. 8, pp. 10857-10878, 2020.

[8] “International Renewable Energy Agency,” International Renewable Energy Agency, [Online]. Available: https://www.irena.org/wind. [Accessed 24 April 2020].

[9] British Wind Energy Association, "Wind Turbine Technology," Kent Art Printers, London, 2005.

[10] A. Sarkar and D. K. Behera, "Wind Turbine Blade Efficiency and Power Calculation with Electrical Analogy," International Journal of Scientific and Research Publications, vol. 2, no. 2, pp. 1-5, 2012.

[11] W. Tong, "Fundamentals of Wind Energy," Wind Power Generation and Wind Turbine Design, pp. 3-48, 2010.

[12] M. Ragheb and A. M. Ragheb, "Wind Turbines Theory-The Betz Equation and Optimal Rotor Tip Speed Ratio," Fundamental and advanced topics in wind power, vol. 1, no. 1, pp. 19-38, 2011.

[13] A. Kalmikov and K. Dykes, Wind Power Fundamentals, Massachussets: MIT Wind Energy Group & Renewable Energy Projects in Action.

[14] D. Bansal and K. Pandey, "Blade Pitch Angle and Tip Speed Ratio Control Schemes for Constant Power Generation of WECS," in 2016 IEEE 1st International Conference on Power Electronics, Intelligent Control and Energy Systems (ICPEICES), 2016: IEEE, pp. 1-6.

[15] N. S. F. M. Murad, M. N. Kamarudin, S. M. Rozali, and M. H. Hairi, "Achieving Optimum Tip-Speed-Ratio of a Two-Mass Wind Turbine System," in 2016 IEEE International Conference on Power and Energy (PECon), 2016: IEEE, pp. 757-762.

[16] A. Sharma, B. K. Saxena, and K. Rao, "Comparison of Wind Speed, Wind Directions, and Weibull Parameters for Sites Having Same Wind Power Density," in 2017 International

Conference on Technological Advancements in Power and Energy (TAP Energy), Kota,2017: IEEE, pp. 1-6.

[17] A. Rajeevan, P. Shouri, and U. Nair, "Identification of Reliability of Wind Power Generation and its Mathematical Modeling," in 2013 Annual International Conference on Emerging Research Areas and 2013 International Conference on Microelectronics, Communications and Renewable Energy, 2013: IEEE, pp. 1-5.

[18] A. Yıldız and B. Dandıl, "Power Generation Potential of Small Wind Turbine in Elazig Province, Turkey," in 2019 4th International Conference on Power Electronics and their Applications (ICPEA), 2019: IEEE, pp. 1-6.

[19] “Kohilo University,” Kohilo Wind LLC, 2015. [Online]. Available: http://kohilowind.com/kohilo-university/202-types-of-wind-turbines-their-advantages-disadvantages/. [Accessed 15 April 2020].

[20] “Turbine Generator,” Turbine Generator.org, [Online]. Available: https://www.turbinegenerator.org/wind/types-wind-turbines/vertical/. [Accessed 15 April 2020].

[21] Y. Baghzouz, "Characteristics of Wind Power Systems," University of Nevada, Las Vegas, 2000.

[22] “New York Wind Energy Guide for Local Decision Makers: Wind Energy Basics,” State of New York, New York, 2014.

[23] P. J. Schubel and R. J. Crossley, "Wind Turbine Blade Design," Energies, vol. 5, no. 9, pp. 3425-3449, 2012.

[24] “The Inside of a Wind Turbine,” US Department of Energy, [Online]. Available: https://www.energy.gov/eere/wind/inside-wind-turbine. [Accessed 28 April 2020].

[25] N. Kangwa, "Small Signal Stability Analysis of a Voltage Source Converter (VSC) Based High Voltage Direct Current System with Onshore Wind Power Generation," 2017.

[26] M. G. Molina and J. M. G. Alvarez, "Technical and Regulatory Exigencies for Grid Connection of Wind Generation," Wind Farm-Technical Regulations, Potential Estimation and Siting Assessment, p. 29, 2011, doi: 10.5772/16474.

[27] H. Louie, “Off-Grid Electrical Systems in Developing Countries,” Seattle: Springer International Publishing, 2018.

[28] D. K. Bhutto, J. A. Ansari, S. S. H. Bukhari, and F. A. Chachar, "Wind Energy Conversion Systems (WECS) Generators: A Review," in 2019 2nd International Conference on Computing, Mathematics and Engineering Technologies (iCoMET), 2019: IEEE, pp. 1-6.

[29] S. Sumathi, L. A. Kumar, and P. Surekha, "Wind Energy Conversion Systems," in Solar PV and Wind Energy Conversion Systems: Springer, 2015, pp. 247-307.

[30] A. M. Rauf, V. Khadkikar, and M. S. El Moursi, "A New Fault Ride-Through (FRT) Topology for Induction Generator Based Wind Energy Conversion Systems," IEEE Transactions on Power Delivery, vol. 34, no. 3, pp. 1129-1137, 2019.

[31] J. C. González, N. J. Castrillón, and S. Hincapié, "Applications and Validation of WECC Model for Type 4 Wind Generator Controller for the Colombian Power System," in 2018 IEEE PES Transmission & Distribution Conference and Exhibition-Latin America (T&D-LA), 2018: IEEE, pp. 1-5.

[32] A. V. Deshpande and V. Kulkarni, "Doubly Fed Induction Generator-A Wind Technology in the Power System," in 2019 Third International conference on I-SMAC (IoT in Social, Mobile, Analytics and Cloud)(I-SMAC), 2019: IEEE, pp. 667-672.

[33] S. Singh, "Study and Control of Direct Driven Type-4 Grid Connected Wind Energy Conversion System," in 2019 5th International Conference on Signal Processing, Computing and Control (ISPCC), 2019: IEEE, pp. 298-305.

[34] T. Renuka, P. Reji, and S. Sreedharan, "Enhancement of Small Signal Stability of a DFIG-Based Wind Power System Using Fuzzy Logic Control," International Journal of Engineering, Science and Technology, vol. 8, no. 3, pp. 48-63, 2016.

[35] M. E. Montilla-DJesus, S. Arnaltes, E. D. Castronuovo, and D. Santos-Martin, "Optimal Power Transmission of Offshore Wind Power Using a VSC-HVDC Interconnection," Energies, vol. 10, no. 7, p. 1046, 2017.

[36] A. D. Hansen, F. Iov, P. E. Sørensen, N. A. Cutululis, C. Jauch, and F. Blaabjerg, "Dynamic Wind Turbine Models in Power System Simulation Tool DIgSILENT," 2007.

[37] I. P. a. I. C. T. M. C. Park, Software Implementation. User guide, microsemi. com.

[38] I. Khan et al., "Dynamic Modeling and Robust Controllers Design for Doubly Fed Induction Generator-Based Wind Turbines Under Unbalanced Grid Fault Conditions," Energies, vol. 12, no. 3, p. 454, 2019.

[39] B. Rached, M. Elharoussi, and E. Abdelmounim, "Control Strategies for DFIG Based on Wind Energy Conversion System using RST and Fuzzy Logic Controllers," in 2019 International Conference of Computer Science and Renewable Energies (ICCSRE), 2019: IEEE, pp. 1-6.

[40] L. Dong, S. Liu, R. Liu, and Y. Guo, "Modeling and Fault Analysis of Doubly Fed Wind Power Generation Systems," in 2016 IEEE PES Asia-Pacific Power and Energy Engineering Conference (APPEEC), 2016: IEEE, pp. 2574-2579.

[41] H. Shih-Min, Power Systems-Basic Concepts and Applications- Part I, Fairfax: PDH Online,PDH Center, 2012.

[42] S. W. Blume, Electric Power System Basics for the Nonelectrical Professional. John Wiley & Sons, 2016.

[43] A. Bose, "Power System Stability: New Opportunities for Control," in Stability and Control of Dynamical Systems with Applications: Springer, 2003, pp. 315-330.

[44] P. Kundur et al., "Definition and Classification of Power System Stability IEEE/CIGRE Joint Task Force on Stability Terms and Definitions," IEEE transactions on Power Systems, vol. 19, no. 3, pp. 1387-1401, 2004.

[45] J. Crisp, Power System Stability Guidelines, Australian Energy Market Operator Ltd, 2012.

[46] H. Fayek, I. Elamvazuthi, N. Perumal, and B. Venkatesh, "The impact of DFIG and FSIG Wind Farms on the Small Signal Stability of a Power System," in 2014 5th International Conference on Intelligent and Advanced Systems (ICIAS), 2014: IEEE, pp. 1-6.

[47] N. Hatziargyriou et al., "Definition and Classification of Power System Stability – Revisited & Extended," in IEEE Transactions on Power Systems, vol. 36, no. 4, pp. 3271-3281, July 2021, doi: 10.1109/TPWRS.2020.3041774.

[48] Z. Yanfang, J. Yanbing, M. Rongrong, X. Yingping, and C. Xueting, "Control Parameters Setting Strategy of Converter Used in DFIG Wind Turbine Considering the Small Signal Stability of Power Grid," in 2018 IEEE International Power Electronics and Application Conference and Exposition (PEAC), 2018: IEEE, pp. 1-4.

[49] R. Guan, N. Deng, Y. Xue, and X.-P. Zhang, "Small-Signal Stability Analysis of the Interactions Between Voltage Source Converters and DC Current Flow Controllers," IEEE Open Access Journal of Power and Energy, vol. 7, pp. 2-12, 2019.

[50] T. Van Cutsem, Transient Stability Analysis and Improvement, Liege: Liege Universite, 2019.

[51] G. Deshmukh and S. Deore, "Impact of Wind Power Integration on Transient Stability of Power System," in 2018 International Conference on Recent Innovations in Electrical, Electronics & Communication Engineering (ICRIEECE), 2018: IEEE, pp. 2160-2162.

[52] A. Al-Faoury, “Stability of Power System: Transient Stability,” presented to ECE310,Al-Balqa Applied University, Salt, Jordan, 2017.

[53] J. D. Glover, M. Sarma, and T. Overbye, "Power System-Analysis & Design. sl: Cengage Learning," 2012.

[54] A. Ghosh, “National Programme on Technology Enhanced Learning,” National Programme on Technology Enhanced Learning, [Online]. Available: https://nptel.ac.in/content/storage2/courses/108104051/ui/Course_home-9.htm. [Accessed 13 July 2020].

[55] S. Padhi and B. Mishra, "Solution of Swing Equation for Transient Stability Analysis in Dual-Machine System," IOSR Journal of Engineering, p. 6, 2015.

[56] “Phasor Diagram of Synchronous Motor,” EEEGuide.com, 13 November 2016. [Online]. Available: https://www.eeeguide.com/phasor-diagram-of-synchronous-motor/. [Accessed 16 July 2020].

[57] A. Y. Abdelaziz, A. M. Ibrahim, and Z. G. Hasan, "Transient Stability Analysis With Equal-Area Criterion for Out of Step Detection Using Phasor Measurement Units," International Journal of Engineering, Science and Technology, vol. 5, no. 1, pp. 1-17, 2013.

[58] A. M. Simeon, T. Wanjekeche, E. Hamatwi, and N. K. Mbangula, "Impacts of Distributed Energy Resources on the Grid Transient Stability: A Case Study of Namibia," in 2019 Open Innovations (OI), 2019: IEEE, pp. 184-189.

[59] M. N. Pala, A. Thakar, and A. Patel, "Power Swing and out of Step Protection Using Equal Area Criteria," in 2019 IEEE 5th International Conference for Convergence in Technology (I2CT), 2019: IEEE, pp. 1-7.

[60] B. Sun, Z. He, Y. Jia, and K. Liao, "Small-Signal Stability Analysis of Wind Power System Based on DFIG," Energy and Power Engineering, vol. 5, no. 4, pp. 418-422, 2013.

[61] M. Gu, L. Meegahapola, and K. Wong, "Review of Rotor Angle Stability in Hybrid AC/DC Power Systems," in 2018 IEEE PES Asia-Pacific Power and Energy Engineering Conference (APPEEC), 2018: IEEE, pp. 7-12.

[62] R. Bhushan and K. Chatterjee, "Modelling and Investigation of Small-Signal Stability of DFIG-Based Wind Energy System Using Linear Quadratic Integral Controller," in 2016 National Power Systems Conference (NPSC), 2016: IEEE, pp. 1-6.

[63] S. Ghimire, P. K. Dhital, and A. K. Mishra, "Small Signal Stability Analysis Toolbox: A MATLAB Based GUI," in 2019 Second International Conference on Advanced Computational and Communication Paradigms (ICACCP), 2019: IEEE, pp. 1-5.

[64] D. R. Chandra et al., "Impact of SCIG, DFIG Wind Power Plant on IEEE 14 Bus System with Small Signal Stability Assessment," in 2014 Eighteenth National Power Systems Conference (NPSC), 2014: IEEE, pp. 1-6.

[65] D. Gautam, "Impact of Increased Penetration of DFIG Based Wind Turbine Generators on Rotor Angle Stability of Power Systems," Arizona State University, 2010.

[66] D. T. Oyedokun, "Power Flow and Rotor Angle Stability Studies of HVAC-HVDC Power System Interconnections Using DigSILENT," University of Cape Town, Cape Town, South Africa,2010.

[67] P. Kundur, N. J. Balu, and M. G. Lauby, Power System Stability and Control. McGraw-hill New York, 1994.

[68] K.-S. Shim, S.-J. Ahn, and J.-H. Choi, "Synchronization of Low-Frequency Oscillation in Power Systems," Energies, vol. 10, no. 4, p. 558, 2017.

[69] A. Naderipour, Z. Abdul-Malek, V. K. Ramachandaramurthy, M. R. Miveh, M. J. H. Moghaddam, and J. M. Guerrero, "Optimal SSSC-Based Power Damping Inter-Area Oscillations Using Firefly and Harmony Search Algorithms," Scientific Reports, vol. 10, no. 1, pp. 1-11, 2020.

[70] J. D. Pinzón and D. G. Colomé, "Chaos in Power Systems: Towards Short-term Voltage Stability Analysis," in 2018 IEEE PES Transmission & Distribution Conference and Exhibition-Latin America (T&D-LA), 2018: IEEE, pp. 1-5.

[71] G. Lammert, D. Premm, L. D. P. Ospina, J. C. Boemer, M. Braun, and T. Van Cutsem, "Control of Photovoltaic Systems for Enhanced Short-Term Voltage Stability and Recovery," IEEE Transactions on Energy Conversion, vol. 34, no. 1, pp. 243-254, 2018.

[72] C. Dwivedi, "Literature Survey on Short-Term Voltage Stability Effect, Cause and Control," in 2018 IEEE Green Technologies Conference (GreenTech), 2018: IEEE, pp. 15-20.

[73] S. Johansson, "Long-Term Voltage Stability in Power Systems: Alleviating the Iimpact of Generator Current Limiters," Doctor of Philosophy, School of Electrical and Computer Engineering, Chalmers University of Technology, Goteborg, Sweden, 1998.

[74] S. Gong and W. Zhang, “Real-time Coordinated Control of Long-term Voltage Stability in Power Grid with VSC-MTDC Considering Time Response Characteristics of Components,” in 2020 IEEE Power & Energy Society General Meeting (PESGM), 2020.

[75] M. R. S. Tirtashi, J. Svensson, and O. Samuelsson, "VSC-HVDC Application to Improve the Long-Term Voltage Stability," in 2017 IEEE Manchester PowerTech, Manchester, 2017: IEEE, pp. 1-6.

[76] Namibia Power Corporation, NamPower Transmission Master Plan,Presentation to AEDU Namibia, Swakopmund: NamPower, 2019.

[77] K. Gül, "Control Methods of The VSC-HVDC Connected Offshore Wind Power Plants For Fulfilling; LVRT and Frequency Regulation Support," Ejovoc (Electronic Journal of Vocational Colleges), vol. 8, no. 2, pp. 167-170.

[78] H. Guo, K. Rudion, C. Heyde, and Z. Styczynski, "Stability Studies of Offshore Wind Farms," in 2010 5th International Conference on Critical Infrastructure (CRIS), 2010: IEEE, pp. 1-7.

[79] Electricity Control Board, Transmission Grid Code: Electricity Act,2007, Windhoek: Electricty Control Board, 2018.

[80] National Energy Regulator of South Africa (NERSA), Grid Connection Code for Renewable Power Plants (RPPs) Connected to the Electricity Transmission System (TS) or the Distribution System (DS) in South Africa, National Energy Regulator of South Africa (NERSA), 2019.

[81] M. M. Rahman, M. F. Rabbi, M. K. Islam, and F. M. Rahman, "HVDC over HVAC Power Transmission System: Fault Current Analysis and Effect Comparison," in 2014 International Conference on Electrical Engineering and Information & Communication Technology, 2014: IEEE, pp. 1-6.

[82] W. Li, S. Gao, L. Ding, Z. Wang, and Z. Liu, "Solutions for the Transmission and Storage of Electric Power," in 2018 4th International Conference on Electrical Energy Systems (ICEES), 2018: IEEE, pp. 208-211.

[83] J. Jesus, R. Castro, and J. F. de Jesus, "HVDC Connection of Offshore Wind Parks: VSC vs LCC with STATCOM," in Power Systems Transients, 2011.

[84] L. Yan, L. Chao, C. Yongning, and T. Haiyan, "Fault Ride Through Characteristics of Connection of Large Wind Power Island To VSC-HVDC Grid," in 2016 IEEE PES Asia-Pacific Power and Energy Engineering Conference (APPEEC), 2016: IEEE, pp. 1230-1234.

[85] K. N. I. Mbangula, "An investigation into the Impact of HVDC Schemes on Eskom HV Network's Transient Stability," Master of Science in Engineering, College of Agricultural Engineering and Science, University of KwaZulu-Natal, Durban, 2016.

[86] H. Liu, "Islanded Large Scale Wind Power Integration Based on LCC-HVDC and STATCOM," 2019.

[87] O. E. Oni, I. E. Davidson, and K. N. Mbangula, "A Review of LCC-HVDC and VSC-HVDC Technologies and Applications," in 2016 IEEE 16th International Conference on Environment and Electrical Engineering (EEEIC), Florence, 2016: IEEE, pp. 1-7.

[88] I. Arrambide, I. Zubía, and I. Zamora, "VSC-HVDC Technology on Power Systems and Offshore Wind Farms Integration," in International Conference on Modern Electrical Power Engineering, 2016.

[89] S. T. Schröder, "Wind Energy in Offshore Grids," PhD Degree, DTU Management Engineering, Technical University of Denmark, Roskilde, 2013. [75] M. Barnes, D. Van Hertem, S. P. Teeuwsen, and M. Callavik, "HVDC Systems in Smart Grids," Proceedings of the IEEE, vol. 105, no. 11, pp. 2082-2098, 2017.

[90] M. Barnes, D. Van Hertem, S. P. Teeuwsen, and M. Callavik, "HVDC Systems in Smart Grids," Proceedings of the IEEE, vol. 105, no. 11, pp. 2082-2098, 2017.

[91] N. M. Kangwa, C. Venugopal, and I. E. Davidson, "A Review of the Performance of VSC-HVDC and MTDC Systems," in 2017 IEEE PES PowerAfrica, 2017: IEEE, pp. 267-273.

[92] M. Singh, M. Ansari, P. Tripathi, and A. Wadhwani, "VSC-HVDC Transmission System and Its Dynamic Stability Analysis," in 2018 International Conference on Computational and Characterization Techniques in Engineering & Sciences (CCTES), 2018: IEEE, pp. 177-182.

[93] T. Shrivastava, A. Shandilya, and S. Gupta, "Overview Strategy of Wind Farm in VSC-HVDC Power Transmission," in 2016 IEEE 7th Power India International Conference (PIICON), 2016: IEEE, pp. 1-6.

[94] A. Ahmed, "Investigation of Multi-terminal Voltage Source Converter HVDC for Wind Power Integration," Master of Science in Electrical Engineering (Electrical Power and Machines), Electrical Engineering Department, Port-said University, Egypt, 2016.

[95] M. Hannan et al., "Advanced Control Strategies of VSC Based HVDC Transmission System: Issues and Potential Recommendations," IEEE Access, vol. 6, pp. 78352-78369, 2018.

[96] N. Freire, J. Estima, and A. Cardoso, "A Comparative Analysis of PMSG Drives Based On Vector Control and Direct Control Techniques for Wind Turbine Applications," Przegląd Elektrotechniczny, vol. 88, no. 1, pp. 184-187, 2012.

[97] H. Y. Mahmoud, A. H. Besheer, H. M. Hasanien, and A. Y. Abdelaziz, "Different Control Strategies for Converter Based DC Energy Transmission In Offshore Wind Power: A Literature Survey," in 2018 Twentieth International Middle East Power Systems Conference (MEPCON), 2018: IEEE, pp. 190-197.

[98] V. Sood and H. Patel, "Comparison Between Direct and Vector Control Strategy for VSC-HVDC System In EMTP-RV," in 2010 Joint International Conference on Power Electronics, Drives and Energy Systems & 2010 Power India, 2010: IEEE, pp. 1-6.

[99] Y. Ye, Z. Lu, L. Xie, and Y. Qiao, "A Coordinated Frequency Regulation Strategy for VSC-HVDC Integrated Offshore Wind Farms," in 2018 IEEE Power & Energy Society General Meeting (PESGM), 2018: IEEE, pp. 1-5.

[100] SIEMENS, “Fact Sheet: BorWin3 Grid Interconnection System,” SIEMENS, 2020.

[101] G. E. C. (. G. Solutions), “DolWin3 HVDC Voltage Source Converters for Efficient Connection of Renewable Energy:GE's HVDC VSC Solution Connects 900MW of Offshore Wind Power to the German High Voltage Grid,” GE Grid Solutions, 2019.

[102] T. Magg, M. Manchen, E. Krige, J. Wasborg, and J. Sundin, "Connecting Networks with VSC-HVDC in Africa: Caprivi Link interconnector," in IEEE Power and Energy Society Conference and Exposition in Africa: Intelligent Grid Integration of Renewable Energy Resources (PowerAfrica), 2012: IEEE, pp. 1-6.

[103] T. Magg, M. Manchen, E. Krige, E. Kandjii, R. Palsson, and J. Wasbor, "Caprivi Link HVDC Interconnector: Comparison Between Energized System Testing and Real-Time Simulator Testing," in 2012 CIGRE Session, vol. 4: CIGRE, 2012, pp. 1-16.

[104] DIgSILENT PowerFactory, HVDC Connected Offshore Wind Farm, DIgSilent PowerFactory.

[105] R. Ryndzionek and Ł. Sienkiewicz, "Evolution of the HVDC Link Connecting Offshore Wind Farms to Onshore Power Systems," Energies, vol. 13, no. 8, p. 1914, 2020.

[106] Global Wind Atlas and as, “Introduction,” Global Wind Atlas, 2020. [Online]. Available: https://globalwindatlas.info/about/introduction. [Accessed 2 June 2020].

[107] Global Wind Atlas, “Methodology,” Global Wind Atlas, 2020. [Online]. Available: https://globalwindatlas.info/about/method. [Accessed 2 June 2020].

[108] T. Robertson, A. Jarvis, J. Mendelsohn and R. Swart, "Namibia's Coast: Ocean Riches and Desert Treasures," Directorate of Environmental Affairs, Ministry of Environment and Tourism, Windhoek, 2012.

[109] “Global Wind Atlas,” Global Wind Atlas, [Online]. Available: https://globalwindatlas.info/. [Accessed 24 August 2020].

[110] R. Villena-Ruiz, A. Lorenzo-Bonache, A. Honrubia-Escribano, F. Jiménez-Buendía, and E. Gómez-Lázaro, "Implementation of IEC 61400-27-1 Type 3 Model: Performance Analysis under Different Modeling Approaches," Energies, vol. 12, no. 14, p. 2690, 2019.

[111] G. Lal, R. Geetha, and R. Deekshit, "Converter Topologies in VSC-HVDC Systems-an Overview," International Journal of Engineering research & Technology, vol. 3, no. 8, 2014.

[112] M. Svean and A. Thoen, "2-Dimensional Control of VSC-HVDC," Master Thesis, Department of Energy Technology, Aalborg University, Aalborg, 2018.

[113] S. Srivastava and M. Chaudhari, "Comparison of SVPWM and SPWM Schemes for NPC Multilevel Inverter," in 2020 IEEE International Students' Conference on Electrical, Electronics and Computer Science (SCEECS), 2020: IEEE, pp. 1-6.

[114] A. Hilawie, "Investigation of VSC-HVDC System for Dynamic Performance Improvement of EEPCO High Voltage Grid," Master of Science, Addis Ababa University, 2011.

[115] T. W. Shire, "VSC-HVDC Based Network Reinforcement," Master of Science in Electrical Power Engineering, Faculty of Electrical Engineering, Mathematics and Computer Science, High-Voltage Components and Power Systems, Delft University of Technology, Stedin, 2009.

[116] A. F. Abouzeid, A. A. Daoud, S. S. Dessouky, and J. M. Guerrero, "Factors Affecting Offshore Wind Power Integration to Grid through VSC-HVDC," in 2016 Eighteenth International Middle East Power Systems Conference (MEPCON), 2016: IEEE, pp. 184-189.

[117] A. M. Simeon, "The Impact of Increased Penetration of Distributed Generators on the Namibian Grid Stability," Bachelor of Science (Honours), in Electrical Engineering, Department of Electrical and Computer Engineering, University of Namibia, Ongwediva, 2018.

[118] T. Wang, D. Mi, T. Ji, and Z. Wang, "Small Signal Stability Analysis of Wind Integrated Power Systems Based on SDEs with Random Coefficients and Excitations," in 2020 IEEE Power & Energy Society General Meeting (PESGM), 2020: IEEE, pp. 1-5.

[119] M. Gunasegaran, C. Tan, and A. Bakar, "Investigation of Power Swing Phenomenon and Verification of Critical Clearing Time Through Theoretical Calculations and Simulated Studies," 2014.

[120] M. Germanos, "Power System Stability Response and Control Using Small Signal Analysis," Master of Science in the Field of Electrical and Computer Engineering, Department of Electrical and Computer Engineering, North-Eastern University, Boston, Masssachusets, 2015.

[121] R. D. Goud, R. Rayudu, V. Mantha, and C. Moore, "Impact of Short-circuit Ratio on Grid Integration of Wind Farms-A New Zealand Perspective," in 2nd International Conference on Large-Scale Grid Integration of Renewable Energy in India,2019, pp. 4-6.

APPENDICES

Appendix A: NamPower Reduced Network

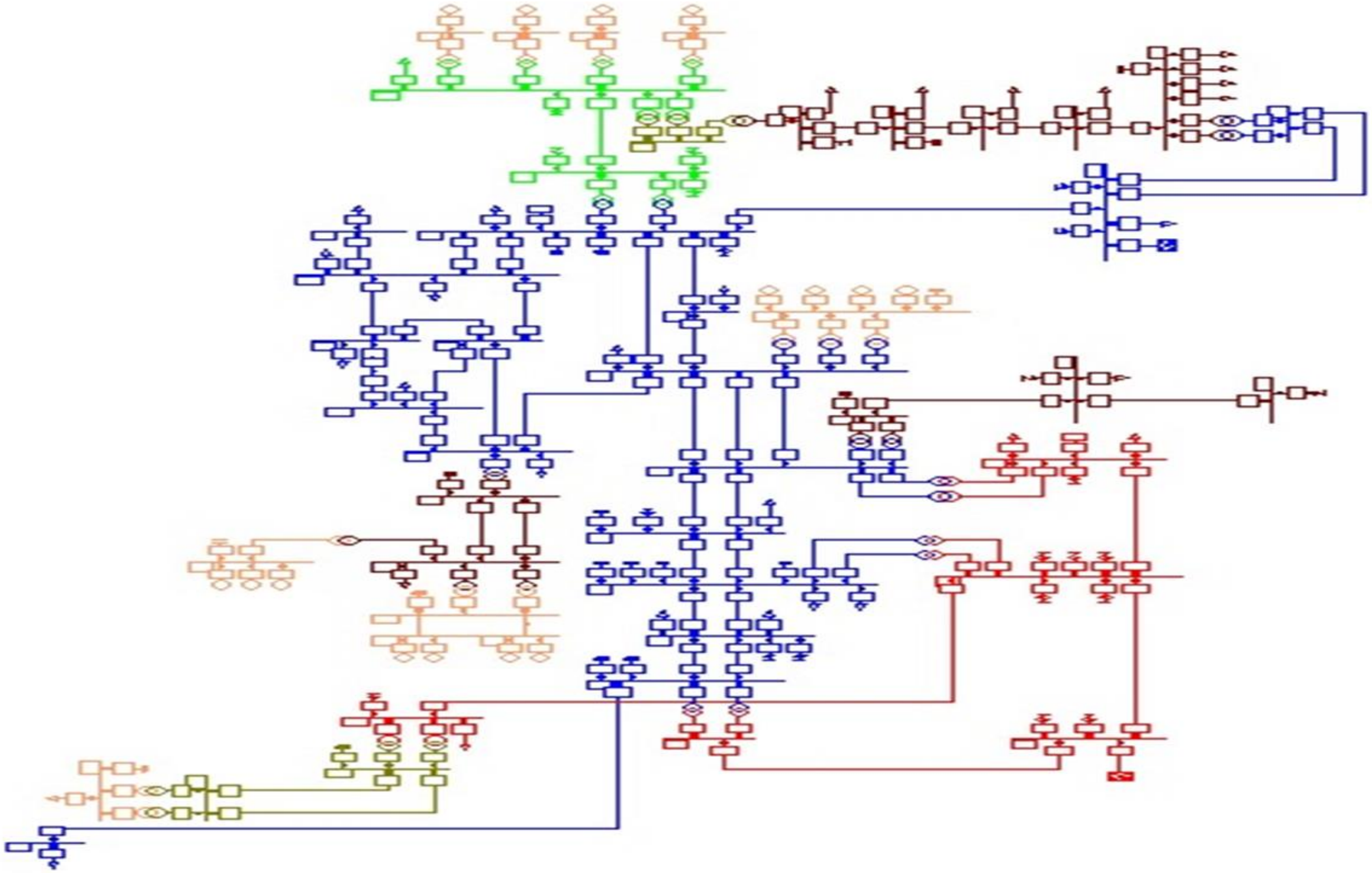

Figure A-0-1:NamPower reduced network model

Appendix A: NamPower Reduced Network Model Load Flow Analysis Results

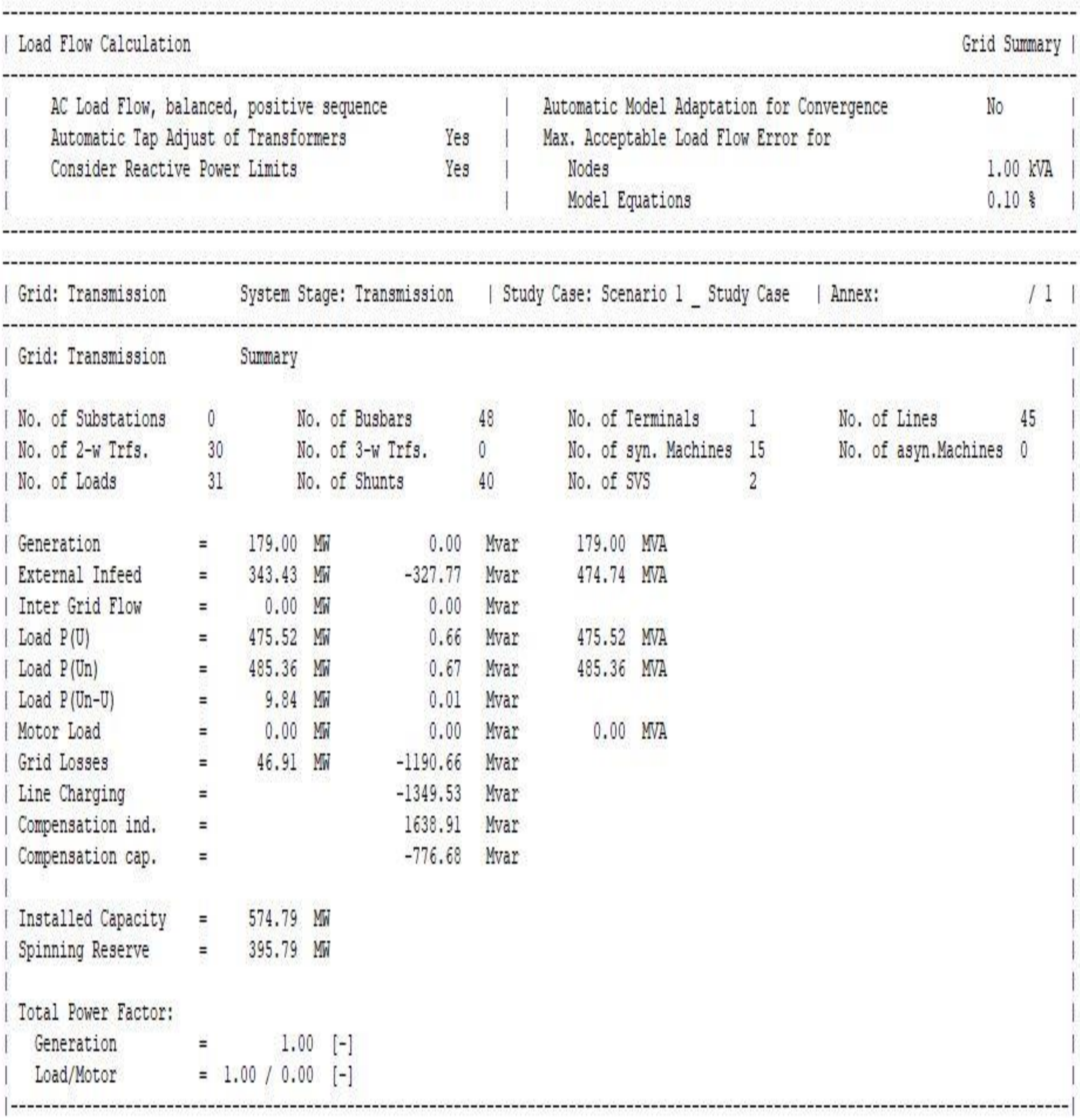

```
----------------------------------------------------------------------------------------------------------------
| Load Flow Calculation                                                                            Grid Summary |
----------------------------------------------------------------------------------------------------------------
|    AC Load Flow, balanced, positive sequence          |   Automatic Model Adaptation for Convergence        No      |
|    Automatic Tap Adjust of Transformers          Yes   |   Max. Acceptable Load Flow Error for                       |
|    Consider Reactive Power Limits                Yes   |     Nodes                                         1.00 kVA  |
|                                                        |     Model Equations                               0.10 %    |
----------------------------------------------------------------------------------------------------------------
----------------------------------------------------------------------------------------------------------------
| Grid: Transmission       System Stage: Transmission     | Study Case: Scenario 1 _ Study Case    | Annex:            / 1  |
----------------------------------------------------------------------------------------------------------------
| Grid: Transmission       Summary                                                                              |
|                                                                                                               |
| No. of Substations    0       No. of Busbars      48      No. of Terminals      1       No. of Lines         45   |
| No. of 2-w Trfs.      30      No. of 3-w Trfs.    0       No. of syn. Machines  15      No. of asyn.Machines 0    |
| No. of Loads          31      No. of Shunts       40      No. of SVS            2                                 |
|                                                                                                               |
| Generation          =    179.00  MW          0.00  Mvar     179.00  MVA                                        |
| External Infeed     =    343.43  MW       -327.77  Mvar     474.74  MVA                                        |
| Inter Grid Flow     =      0.00  MW          0.00  Mvar                                                        |
| Load P(U)           =    475.52  MW          0.66  Mvar     475.52  MVA                                        |
| Load P(Un)          =    485.36  MW          0.67  Mvar     485.36  MVA                                        |
| Load P(Un-U)        =      9.84  MW          0.01  Mvar                                                        |
| Motor Load          =      0.00  MW          0.00  Mvar       0.00  MVA                                        |
| Grid Losses         =     46.91  MW      -1190.66  Mvar                                                        |
| Line Charging       =                    -1349.53  Mvar                                                        |
| Compensation ind.   =                     1638.91  Mvar                                                        |
| Compensation cap.   =                     -776.68  Mvar                                                        |
|                                                                                                               |
| Installed Capacity  =    574.79  MW                                                                           |
| Spinning Reserve    =    395.79  MW                                                                           |
|                                                                                                               |
| Total Power Factor:                                                                                           |
|   Generation        =        1.00  [-]                                                                        |
|   Load/Motor        =  1.00 / 0.00  [-]                                                                       |
|---------------------------------------------------------------------------------------------------------------|
```

Figure A-0-1: Load flow analysis grid summary results

Appendix B: NamPower Reduced Network Model Voltage Results

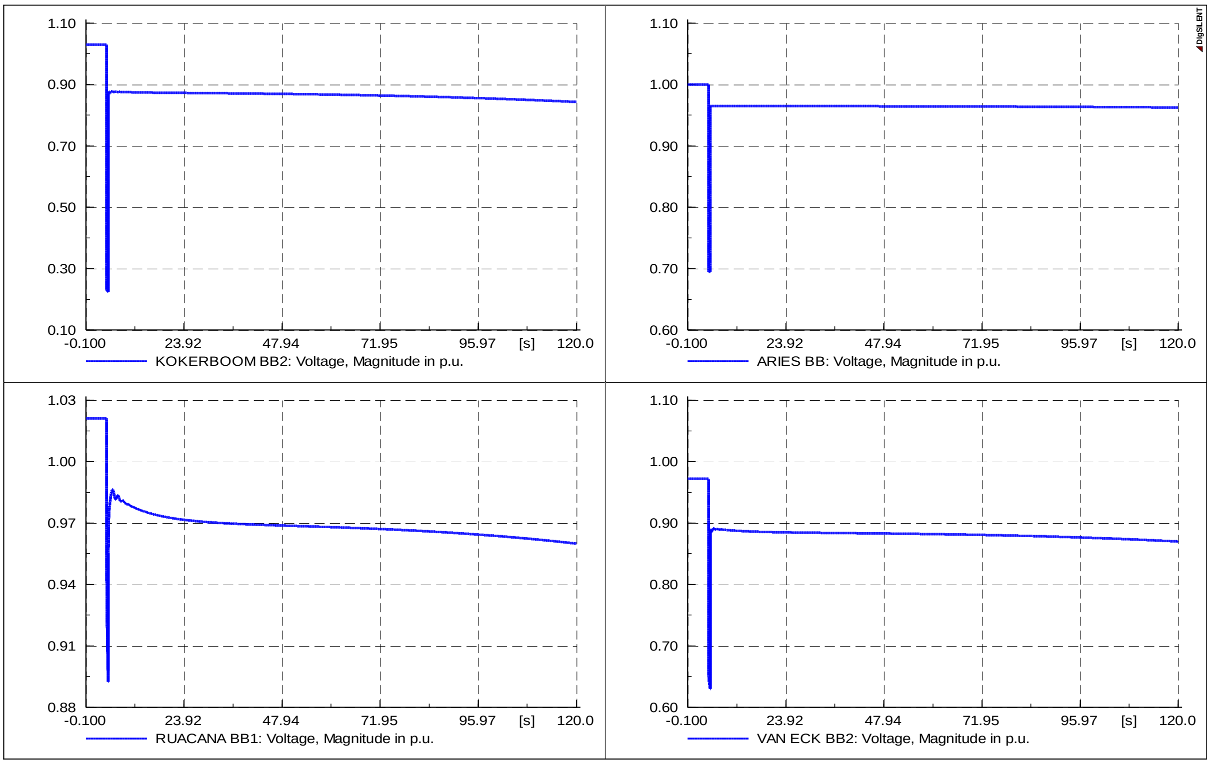

Figure B-0-1: Scenario 1 voltage at busbars

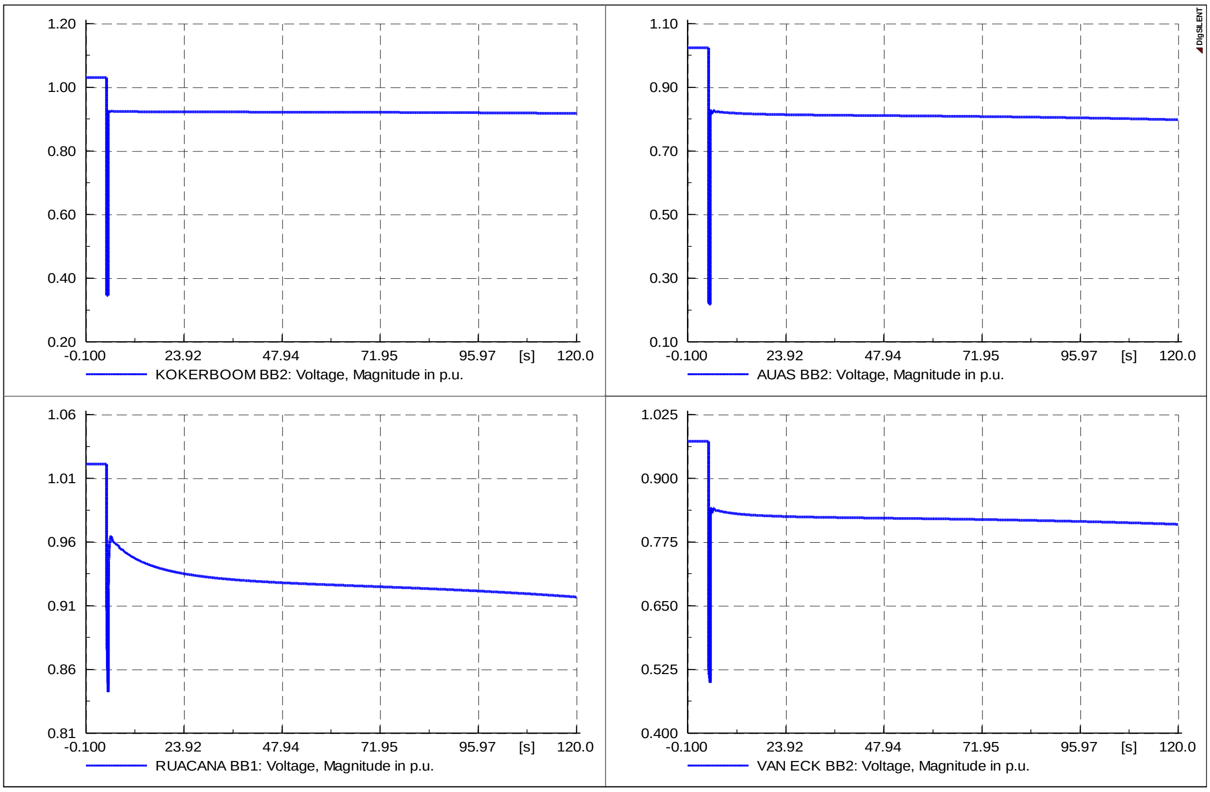

Figure B-0-2: Scenario 2 voltage at busbars

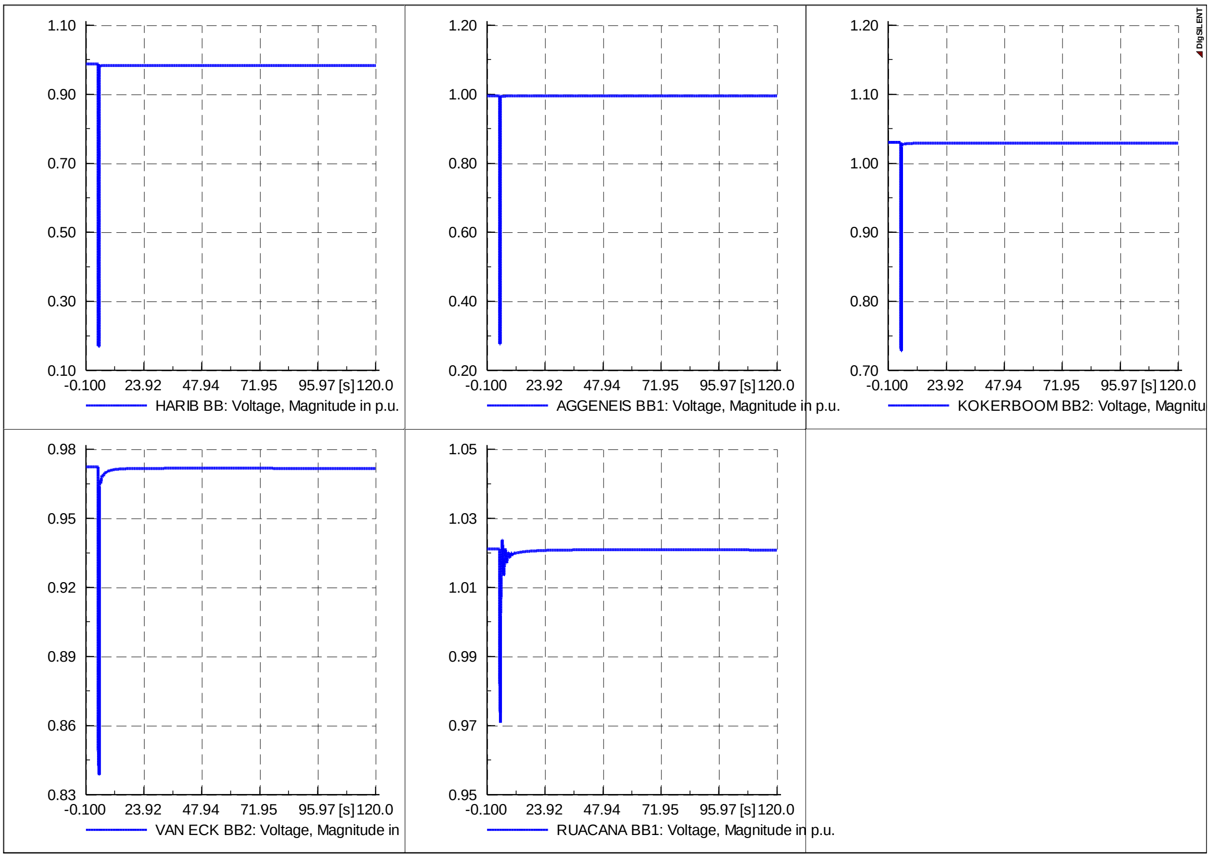

Figure B-0-3: Scenario 3 voltage at busbars

Appendix C: Integrated Network Voltage Results

Scenario 1:

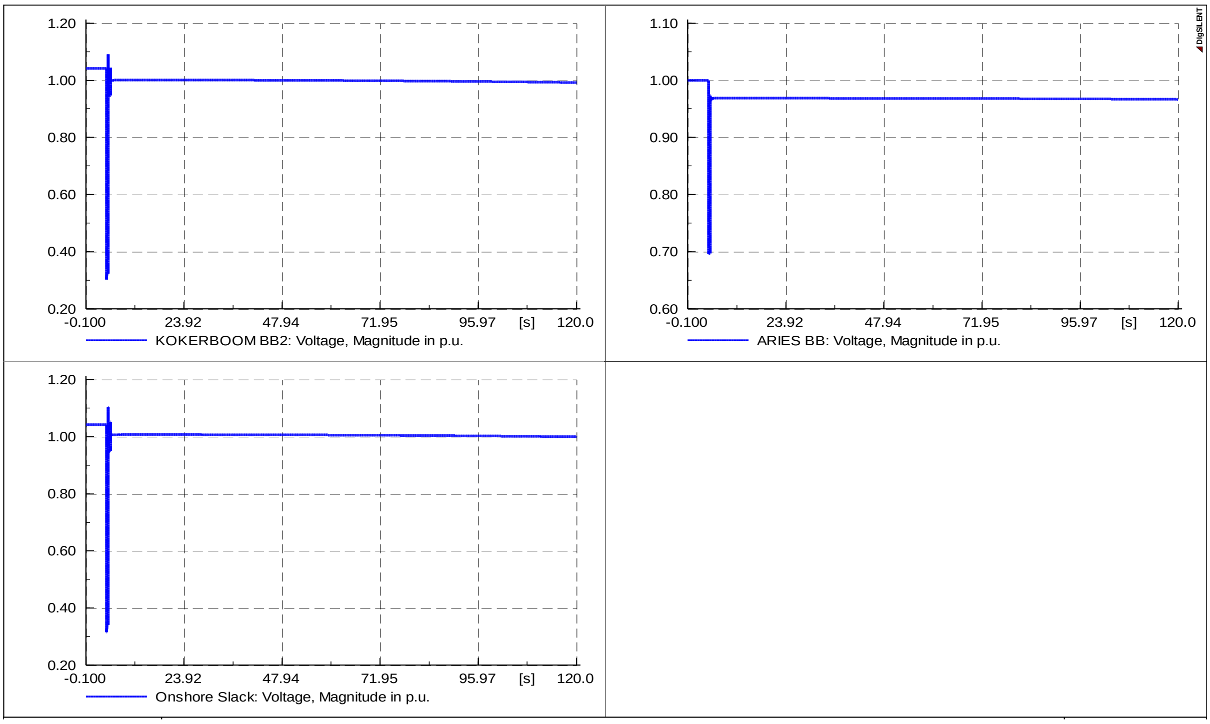

Figure C-0-1: 50MW wind farm integration

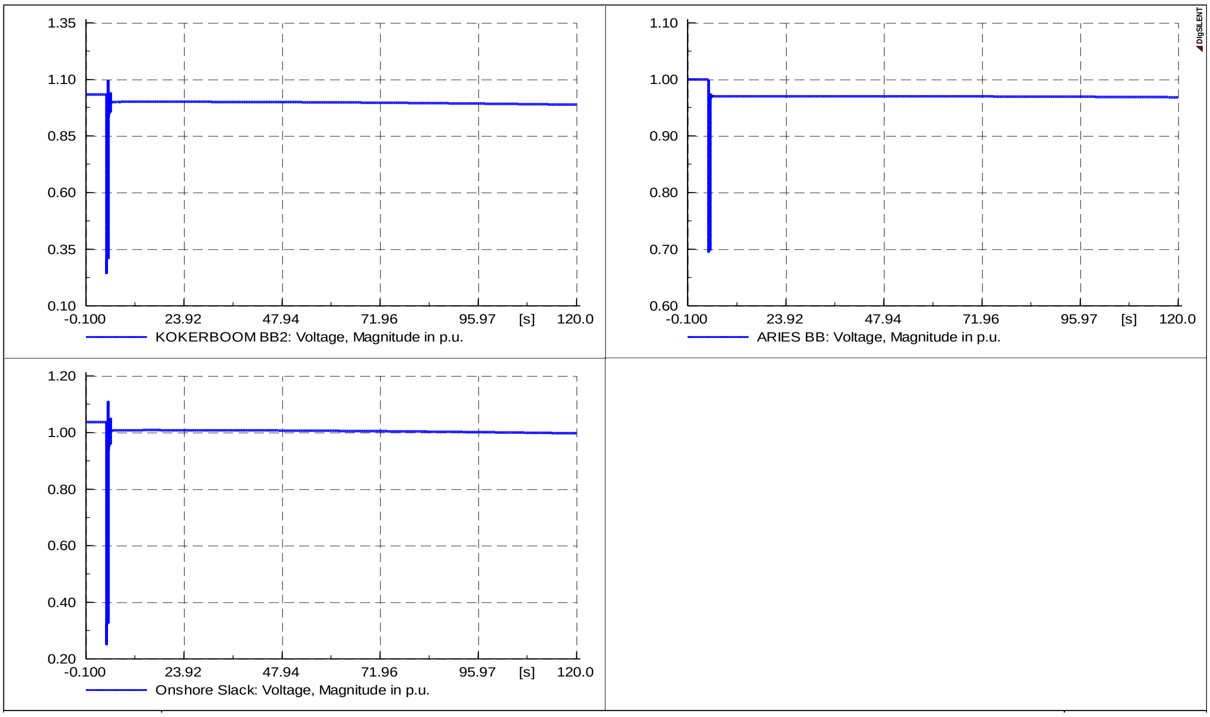

Figure C-0-2:300MW wind farm integration

Scenario 2:

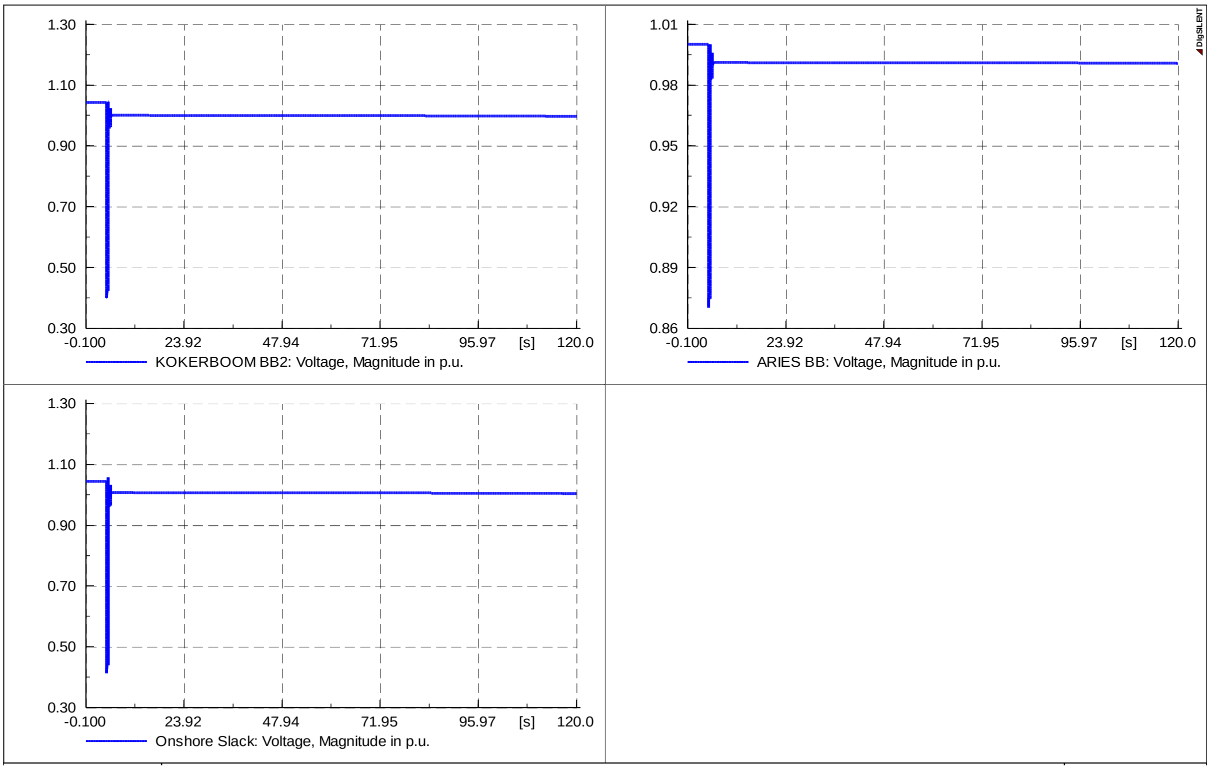

Figure C-0-3: 50MW wind farm integration

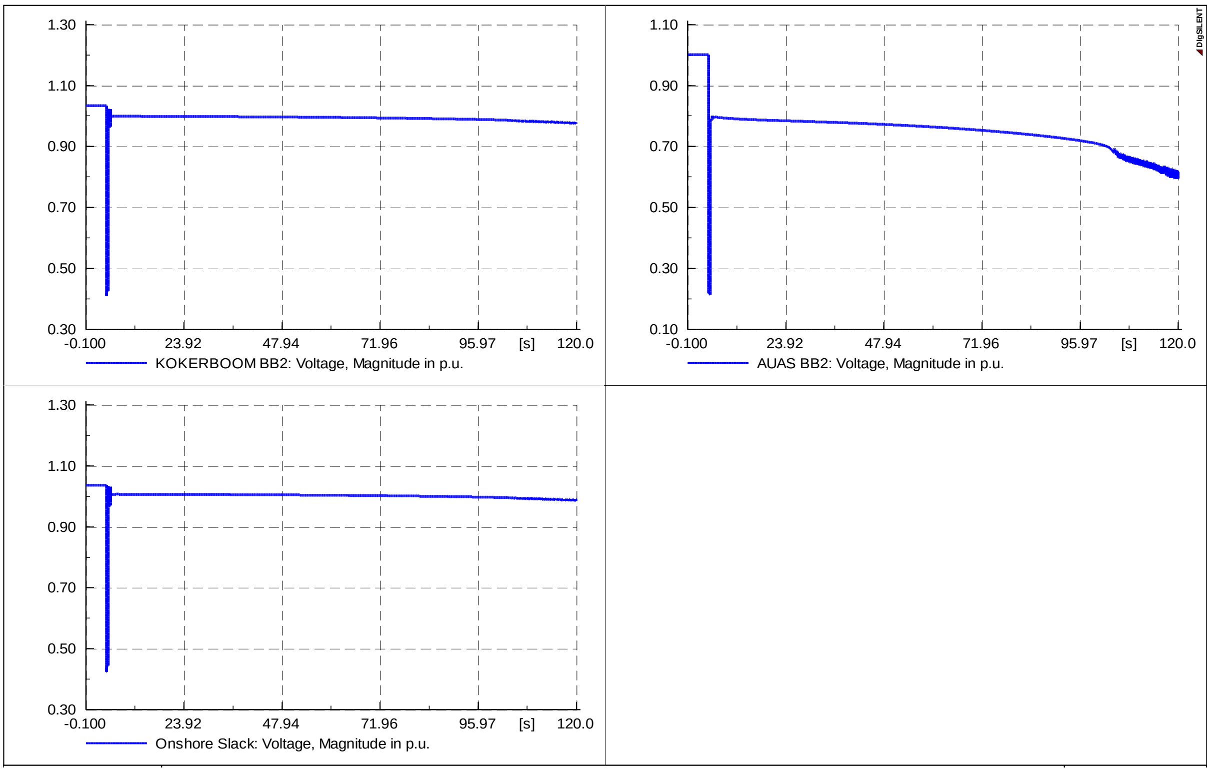

Figure C-0-4:300MW wind farm integration

Scenario 3:

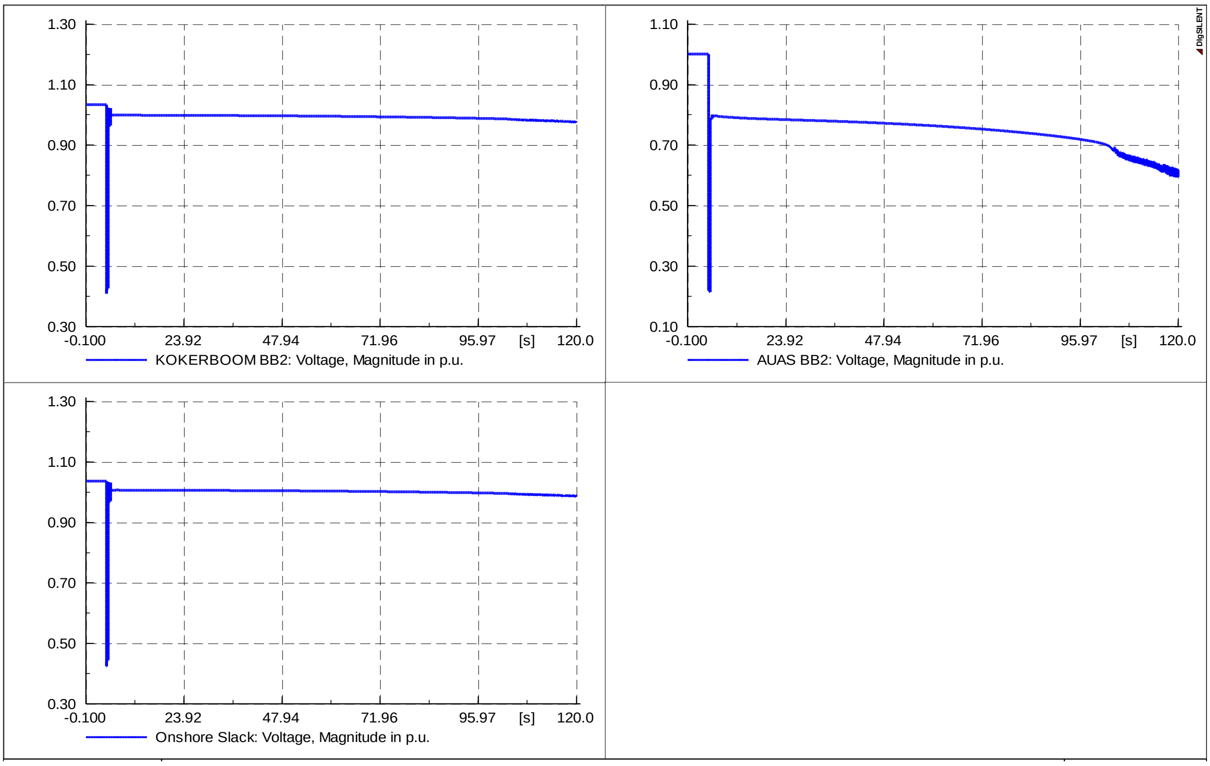

Figure C-0-5: 50MW wind farm integration

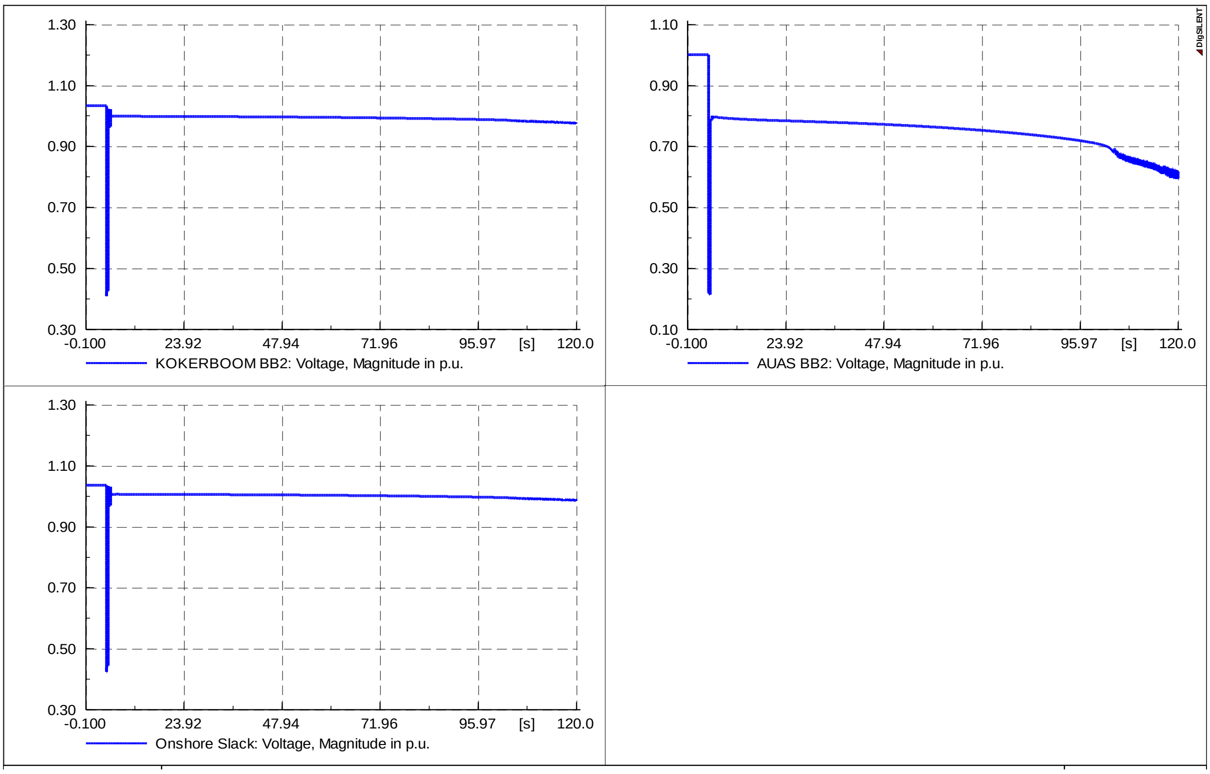

Figure C-0-6:300MW wind farm integration

Scenario 4:

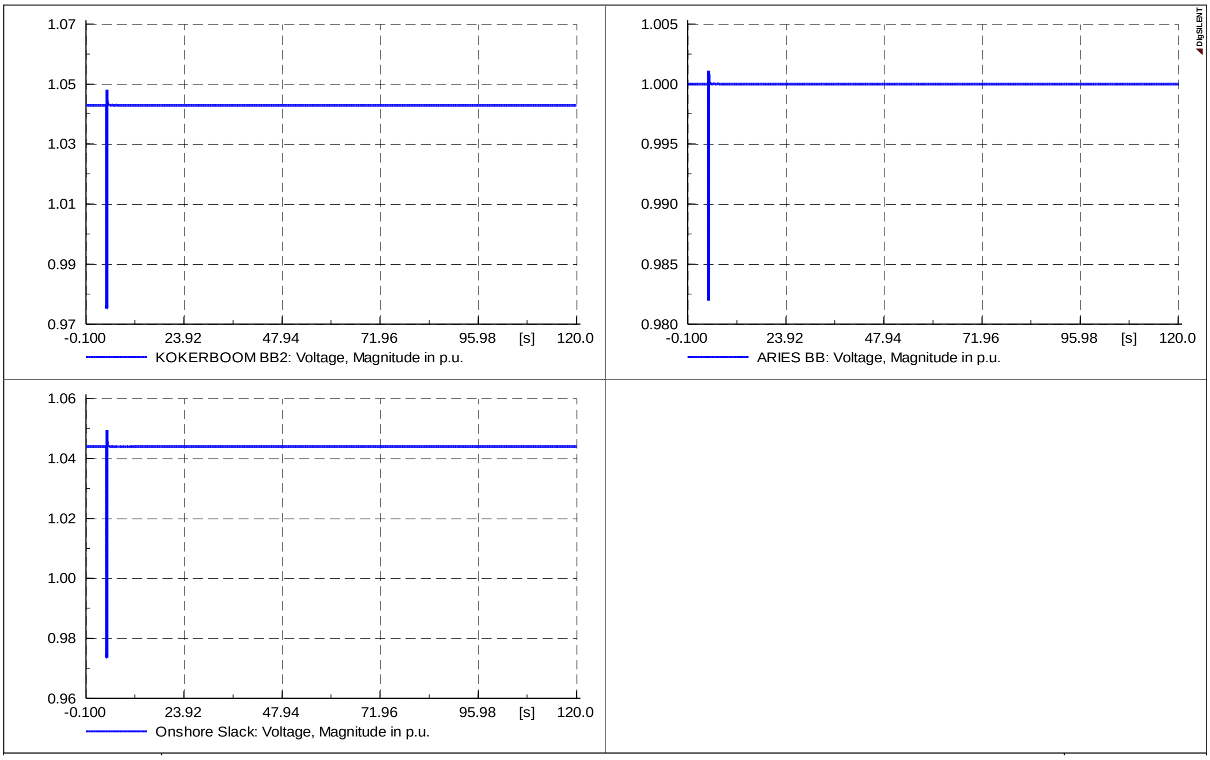

Figure C-0-7:50MW wind farm integration

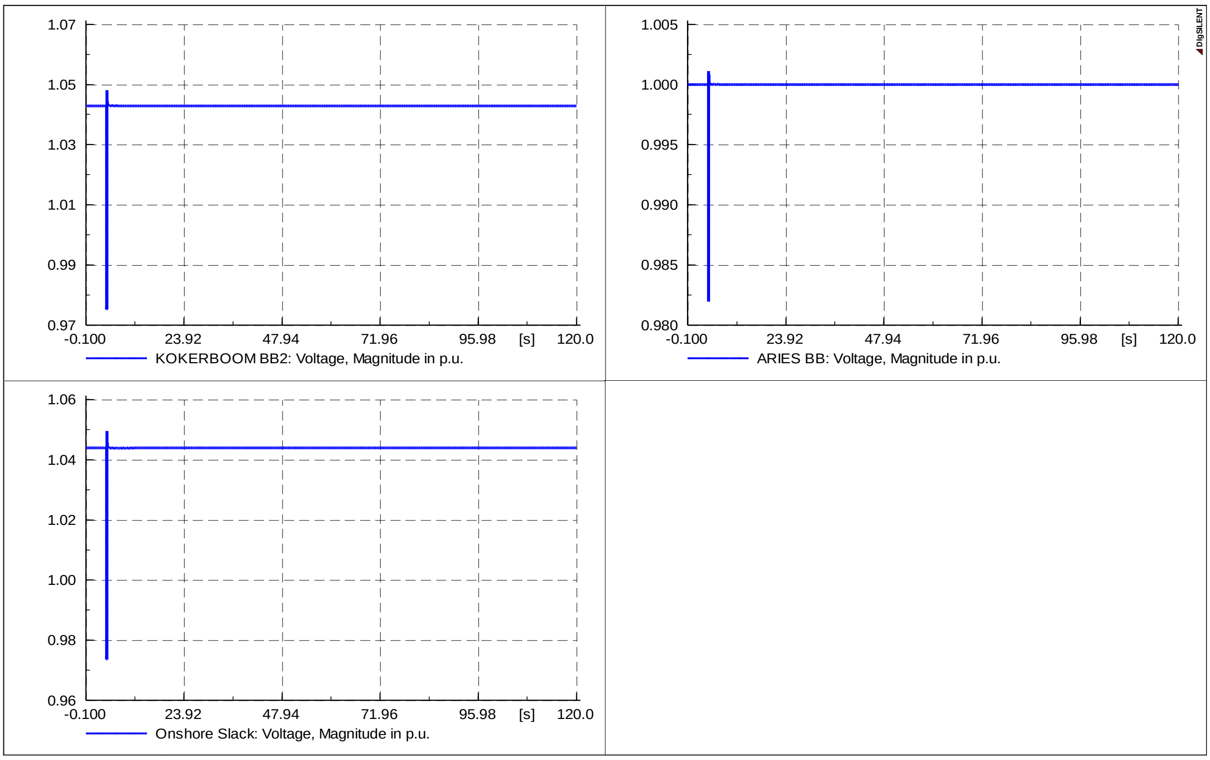

Figure C-0-8:300MW wind farm integration

Appendix D: NamPower Reduced Network Major Equipment Ratings

Table D-0-1: Generator ratings

Parameter	**RUACANA**	**VAN ECK**
Nominal Apparent Power	85 MVA	32.5 MVA
Nominal Voltage	11 kV	11 kV
Power Factor	1.0	0.9
Connection	YN	YN
Xd	2.0 p.u.	1.81
Xq	2.0 p.u.	1.76
Inertia Acceleration Time Constant	10.0	7.778
Stator Resistance (rstr)	0	0.003

Table D-0-2: Transformer ratings

Parameter	**RUACANA**	**VAN ECK**
Rated Power	90 MVA	100 MVA
Nominal Frequency	50 Hz	50 Hz
Rated Voltage (LV)	11 kV	11 kV
Rated Voltage (HV)	330 kV	220 kV
Vector Group and Phase Shift	YNyn0	YNyn0
Positive Sequence Impedance	12.5 %	13.1 %
Zero Sequence Impedance	12.5 %	13.1 %

Table D-0-3: HVAC transmission line parameters

Parameter			
Rated Voltage	400 kV	330 kV	220 kV
Rated Current	0.403 kA	0.187 kA	0.35 kA
Type	Overhead line	Overhead line	Overhead line
Positive and Negative Sequence Impedance	R=0.092 Ω/km X=0.420 Ω/km	R=0.587 Ω/km X=0.495 Ω/km	R=0.208 Ω/km X=0.401 Ω/km
Zero Sequence Impedance	R=0.366 Ω/km X=0.953 Ω/km	R=0.686 Ω/km X=0.514 Ω/km	R=0.308 Ω/km X=0.501 Ω/km